Advances in Materials Science and Engineering

Novel Synthesis and Applications of Metal, Metal Oxides (MOs), and Transition Metal Dichalcogenides (TMDs) for Energy, Sensing, and Memory Applications

Lead Guest Editor: Pradip Basnet
Guest Editors: Arslan Shehzad and Xi-Bo Li

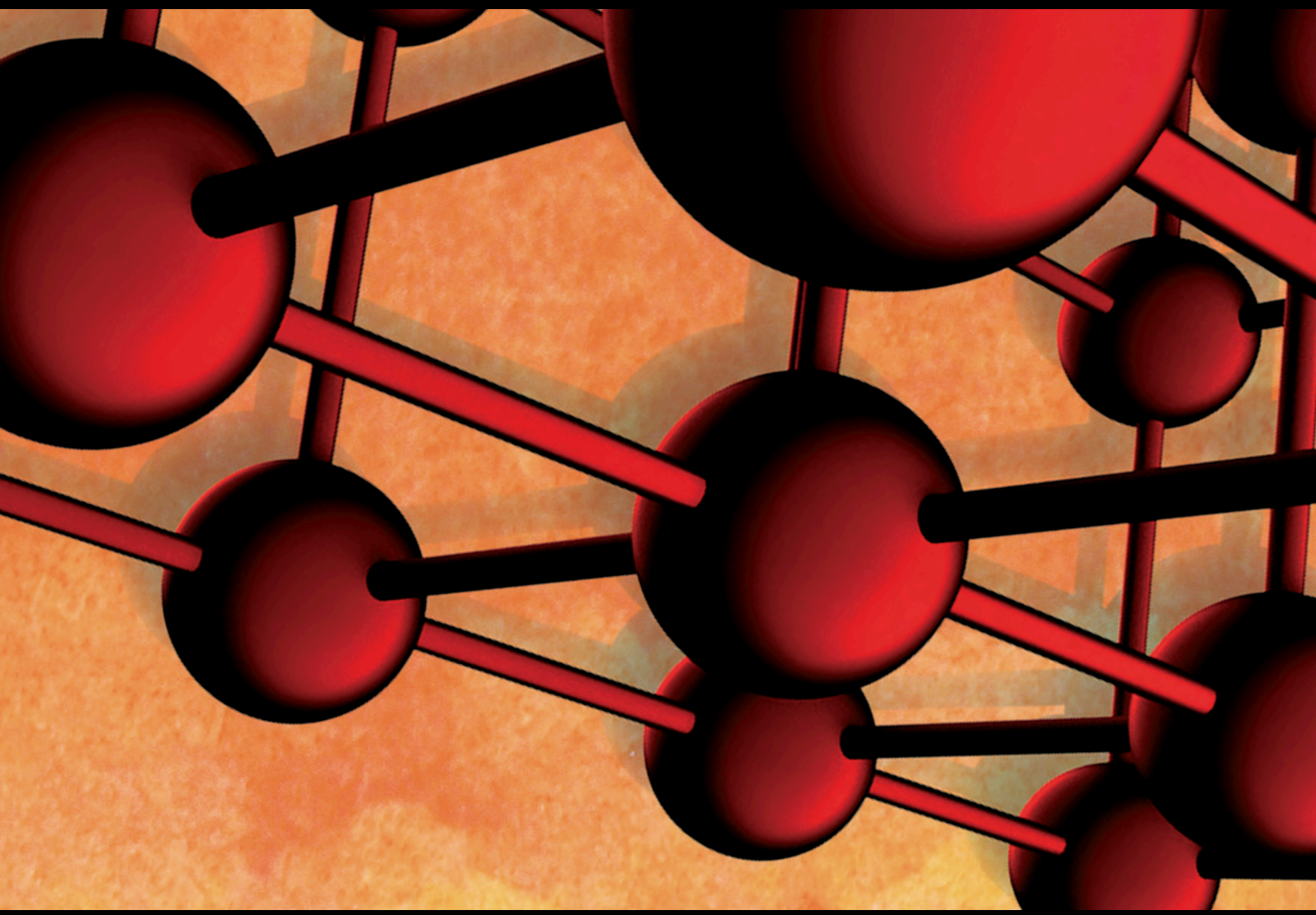

Novel Synthesis and Applications of Metal, Metal Oxides (MOs), and Transition Metal Dichalcogenides (TMDs) for Energy, Sensing, and Memory Applications

Advances in Materials Science and Engineering

Novel Synthesis and Applications of Metal, Metal Oxides (MOs), and Transition Metal Dichalcogenides (TMDs) for Energy, Sensing, and Memory Applications

Lead Guest Editor: Pradip Basnet
Guest Editors: Arslan Shehzad and Xi-Bo Li

Contents

Hindawi
Advances in Materials Science and Engineering
Volume 2019, Article ID 4163786, 2 pages
https://doi.org/10.1155/2019/4163786

Editorial

Novel Synthesis and Applications of Metal, Metal Oxides (MOs), and Transition Metal Dichalcogenides (TMDs) for Energy, Sensing, and Memory Applications

Pradip Basnet,[1] **M. Arslan Shehzad**,[2] **and Xi-Bo Li**[3]

[1]*School of Materials Science & Engineering, Georgia Institute of Technology, Atlanta, USA*
[2]*School of Chemical & Biomolecular Engineering, Georgia Institute of Technology, Atlanta, USA*
[3]*Research Center of Laser Fusion, China Academy of Engineering Physics, Mianyang, China*

Correspondence should be addressed to Pradip Basnet; pradip.basnet@mse.gatech.edu

Received 26 October 2019; Accepted 26 October 2019; Published 7 November 2019

Study of metal, metal oxides (MOs), and transition metal dichalcogenides (TMDs) micro-/nanostructures has been an area of interest for researchers recently. These materials exhibit interesting properties for a wide range of applications ranging from electronics to energy conversion. Nanostructures and composites of these metallic nanomaterials due to their high aspect ratio and quantum confinement have been studied for many applications including energy conversion, bio/chemical sensing, and memory applications. Among the different synthesis techniques that are reported for these nanomaterials, physical and chemical methods are the two well-known synthesis routes. In this special issue, we present a selection of invited and contributed articles, which focus on both synthesis and application of these nanomaterials. These accepted manuscripts span a wide range of materials for the applications highlighting novel fabrication techniques as well as suitable test protocols.

In an article entitled "Deposition of Gold Nanoparticles via Galvanic Replacement in DMSO and Their Influence on Formation of Silicon Nanostructures," M. Shepida et al. have reported a lithography-free gold nanoparticle (Au NP) deposition technique on Si substrates through galvanic replacement (GR) in dimethyl sulfoxide (DMSO) solution. The authors further analyzed the effect of $HAuCl_4$ solution concentration, reaction time, and temperature on the characteristics of the deposited Au NPs. By using the metal-assisted chemical etching method, they demonstrated one of the possible applications of synthesized Au NPs, e.g., the formation of nanorods. N. Odaira and Y. Arita in the article entitled "An Estimation of the Thermal Properties of Pu-Rich Metallic Fuel" have studied and reported the estimation of thermal properties of a Pu-rich metallic fuel which has potential to reduce minor actinides with small capacity of fast reactors. Their estimation, using both Nordheim's rule and Wiedemann–Franz law, indicated that this metallic fuel has much lower thermal conductivity and melting point. Furthermore, it was observed that the uranium addition causes increasing thermal conductivity and melting point. In the paper entitled "Synthesis of Mesoporous TiO_2 Spheres via the Solvothermal Process and Its Application in the Development of DSSC," S. Velázquez-Martínez et al. have described both the preparation and testing procedure of TiO_2 microstructures. They have discussed the usefulness of the solvothermal method for making TiO_2 nanoparticles that can be used for solar energy conversion efficiently. For example, the effects of changing solvent-system on the TiO_2 products have been studied and reported in detail.

G. Fedorenko et al. in the paper entitled "Oxide Nanomaterials Based on SnO_2 for Semiconductor Hydrogen Sensors" reported a synthesis of SnO_2 nanostructures which were then characterized for hydrogen sensor applications. Atomically thin SnO_2 (~5.3 nm) was synthesized using the sol-gel method. Additionally, palladium doping was done in order to improve response to hydrogen, and a comparison was made with undoped SnO_2. It was observed that doped nanostructures provide fast response and recovery time and a wide measuring range of hydrogen content in air ambient with good repeatability of the sensor signal. Such promising

properties could make useful sensors based on these nanomaterials for devices intended to determine hydrogen in air. In the paper entitled "Characterization of Layer Number of Two-Dimensional Transition Metal Diselenide Semiconducting Devices Using Si-Peak Analysis," X. Zhang has reported a nondestructive method of characterizing the layer number of "atomically thin" stacking 2D transition metal diselenide nanomaterials, namely, $MoSe_2$ and WSe_2, using Raman spectroscopy. The Raman approach for finding the layer number of $MoSe_2$ and WSe_2 were reported to be controlled by the change in their optical properties while testing up to four layers.

Concluding the guest editors highlights, we believe that the articles published in *Advances in Materials Science and Engineering,* special issue, provide useful information as a basis for a better understanding of the metal, MOs, and TMDs micro-/nanostructures and may further aid the scope fabrication and use of multifunctional nanomaterials.

Conflicts of Interest

The editors declare that they have no conflicts of interest regarding the publication of this Special Issue.

Acknowledgments

We, guest editors, thank all authors and contributors who submitted their high-quality work for consideration in this special issue. We also appreciate the time and consideration of the reviewers for their valuable feedback in the review process and hence improving the quality of the published articles. We thank one of the guest editors Dr. Sajjad Hussain for his contribution as an editor or deciding on the submitted manuscript. Lastly, we are thankful to Ms. Heba Hamdy for her help.

Pradip Basnet
M. Arslan Shehzad
Xi-Bo Li

Hindawi
Advances in Materials Science and Engineering
Volume 2019, Article ID 7865698, 7 pages
https://doi.org/10.1155/2019/7865698

Research Article

Characterization of Layer Number of Two-Dimensional Transition Metal Diselenide Semiconducting Devices Using Si-Peak Analysis

Xian Zhang

Department of Mechanical Engineering, Stevens Institute of Technology, 1 Castle Point Terrace, Hoboken, NJ 07030, USA

Correspondence should be addressed to Xian Zhang; xzhang4@stevens.edu

Received 20 April 2019; Revised 8 July 2019; Accepted 12 August 2019; Published 10 September 2019

Guest Editor: Xi-Bo Li

Atomically thin materials such as semiconducting transition metal diselenide materials, like molybdenum diselenide ($MoSe_2$) and tungsten diselenide (WSe_2), have received intensive interests in recent years due to their unique electronic structure, bandgap engineering, ambipolar behavior, and optical properties and have motivated investigations for the next-generation semiconducting electronic devices. In this work, we show a nondestructive method of characterizing the layer number of two-dimensional (2-D) $MoSe_2$ and WSe_2 including single- and few-layer materials by Raman spectroscopy. The related photoluminescence properties are also studied as a reference. Although Raman spectroscopy is a powerful tool for determining the layer number of 2-D materials such as graphene and molybdenum disulfide (MoS_2), there have been difficulties in precisely characterizing the layer number for $MoSe_2$ and WSe_2 by Raman spectroscopy due to the uncertain shifts during the Raman measurement process and the lack of multiple separated Raman peaks in $MoSe_2$ and WSe_2 for referencing. We then compared the normalized Si peak with $MoSe_2$ and WSe_2 and successfully identified the layer number of $MoSe_2$ and WSe_2. Similar to graphene and MoS_2, the sample layer number is found to modify their optical properties up to 4 layers.

1. Introduction

Because of their unique structure and exotic physical and mechanical properties, two-dimensional (2-D) materials have drawn tremendous interests since their discovery [1–5]. The introduction of mechanical exfoliation method has enabled us to tailor the thickness of bulk layered materials down to a single unit cell [1, 2, 6]. One particular group of 2-D materials, i.e., transition metal dichalcogenides (TMDCs) [7–12], has been extensively studied for their electrical and optical properties. This is because of the tunable electronic band structure with layer numbers [13] and temperature [14, 15] and more recently with heterostructure engineering leading to the discovery of superconductivity and exotic excitons [16–19]. As an example, molybdenum disulfide (MoS_2), one of the TMD materials, has been widely explored for its properties of Raman spectroscopy [20], photoluminescence (PL) [10–12, 14], and magnetic field influence [21] and with applications of field-effect transistors [7, 22] and chemical sensors [23].

Recently, transition metal diselenides $MoSe_2$ and WSe_2 have become the new 2-D stars owing to the creation of moiré excitons in their heterostructures [17, 18]. They are both at the transition of direct- and indirect-bandgap electronic structures around few layers, which provides new opportunities to engineer their electrical and optical properties [14, 24–27]. By sharing the same chalcogen atoms, their lattice constants also match well, which even allows for epitaxial growth of heterostructures [28, 29]. For these applications, a good understanding of their band structures and accurate thickness determination are in need. Despite the abundant explorations of their electrical conductance properties [30], optical properties [14], and even angle-resolved photoemission spectroscopy [24], a quantitative and nondestructive characterization method of characterizing the layer number of $MoSe_2$ and WSe_2 on silicon substrates is still lacking. Especially, due to the

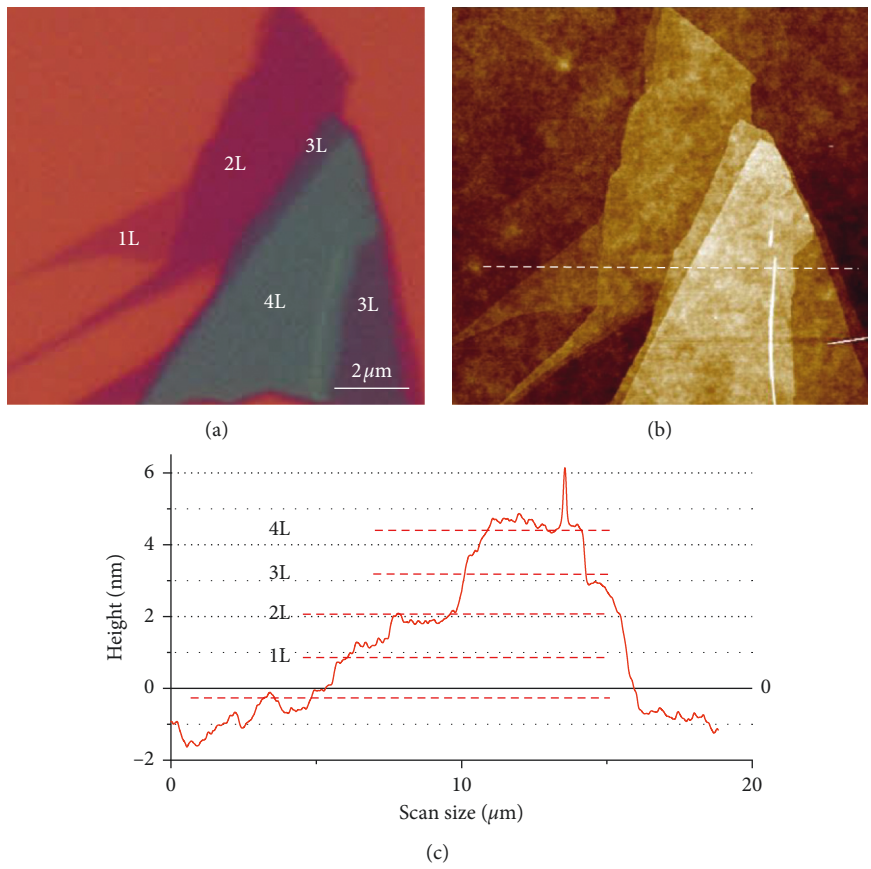

FIGURE 1: (a) Optical image and (b) atomic force microscope (AFM) image of 1–4L $MoSe_2$. The scale bar is 2 μm. (c) AFM profile of 1–4L $MoSe_2$.

infeasibility of extracting multiple Raman peaks of $MoSe_2$, which has only one Raman peak, and WSe_2, which has two Raman peaks that are not fully separated, the relative Raman peak position could not be characterized like what has been done with MoS_2 [15]. Recent studies have been using reflectance spectroscopy [31, 32] and absorbance spectroscopy [33] to characterize the layer number of 2-D transition metal dichalcogenides, but the limitation with some studies [31, 33] is that these 2-D materials are fabricated on the transparent substrate, and the additional fabrication step is needed to transfer 2-D materials to the target substrate for semiconducting applications. Moreover, a clear trend of reflectance spectroscopy and absorbance spectroscopy could be observed in 2-D materials with different layer numbers [31–33], but there lacks a quantitative value to identify each layer number alone. All of this makes it infeasible for the 2-D materials' semiconductor device applications. Our method of directly characterizing 2-D $MoSe_2$ and WSe_2 on the SiO_2/Si substrate confirms this previously reported method's [34] feasibility to a broader range of 2-D materials. It has the advantages of keeping the sample's physical properties closest to pristine, providing quantitative values for precise layer number characterization, and nondestruction, thus providing direct industrial applications.

In this paper, we characterized the layer number of $MoSe_2$ and WSe_2 by Raman spectroscopy with referencing to the substrate silicon's Raman peaks. Both materials possess increasing Raman peak intensity with increasing layer numbers until reaching 4 layers (L). We also found 1L $MoSe_2$ and WSe_2 flakes possess higher PL intensity than the few-layer flakes.

2. Materials and Methods

2.1. Materials and Procedures. $MoSe_2$ and WSe_2 bulk crystals (SPI Supplies) were used for mechanical exfoliation to obtain few-layer materials. The $MoSe_2$ or WSe_2 crystal was procured and exfoliated by using a scotch tape. The crystal of size 3 mm × 3 mm was used. After exfoliation on the scotch tape for ~8 times, the crystal with scotch tape was pressed onto a clean SiO_2 (285 nm)/Si substrate, and the end of a sharpie was used to abrade for 3 minutes. After removing the scotch tape, the flakes are left on the SiO_2 (285 nm)/Si substrate. 285 nm SiO_2 was used because it provides the best contrast for identifying the thin flakes under an optical microscope (Nikon Eclipse 150) (Figure 1(a)). The final $MoSe_2$ or WSe_2 flakes obtained in this way has a size from 2 μm to 15 μm. Each flake's thickness was determined by the tapping mode of atomic force microscopy (AFM) (Bruker AFM) (Figure 1(b)). Further confirmation of the layer number is by the optical method described in this article.

2.2. Raman Optical Measurement. A micro-Raman spectrometer (RENISHAW InVia Raman Microscope system) was used to measure the Raman spectra (Figures 2-3) for studying peak shifts and photoluminescence (PL)

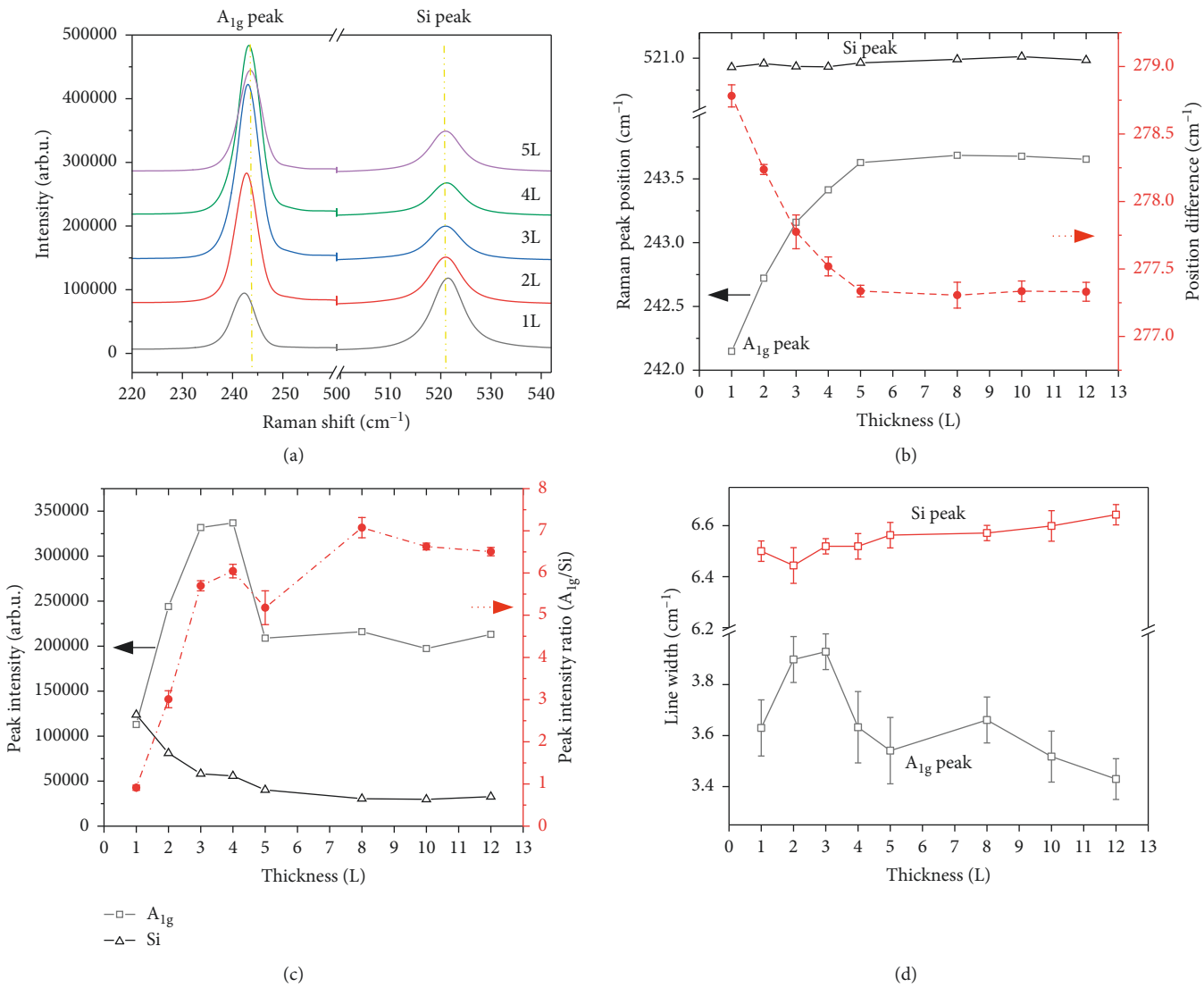

FIGURE 2: (a) Raman spectra of different layer numbers of $MoSe_2$ supported by SiO_2 (285 nm)/Si substrate by 633 nm laser. (b) Raman peak position of $MoSe_2$'s A_{1g} peak and Si peak for different layer numbers (left vertical axis) and their difference (right vertical axis). (c) Raman peak intensity of $MoSe_2$'s A_{1g} peak and Si peak for different layer numbers (left vertical axis) and their ratio (right vertical axis). (d) Raman peak line width of $MoSe_2$'s A_{1g} peak and Si peak.

(Figure 4(a)) of $MoSe_2$ and WSe_2. Laser with a wavelength of 633 nm was used. 1 mW laser power was used for Raman and PL measurement, to provide the best result without damaging the sample. Flakes from 1 layer to up to 15 layers were measured. The 100x objective with a numerical aperture of 0.90 of the Raman microscope system was used. For a more accurate characterization, we recharacterized the laser spot size by moving the laser across a sharp edge and fit Raman peak mapping's intensity curve. The laser spot size obtained in this way is 0.46 μm, which is the smallest in all the objectives and could provide the best resolution from the spot on the sample of measurement interest. All the measurements were performed in air at room temperature.

3. Results and Discussion

3.1. Optical Microscopy and Atomic Force Microscopy. Figure 1(a) shows an optical microscopy image of a mechanically exfoliated 1- to 4-layer (L) $MoSe_2$ flake. By choosing a Si substrate with a 285 nm thermal oxide SiO_2, we can obtain a good optical contrast for different thicknesses (Figure 1(a)). The same preparation method is used for WSe_2 flakes. Figure 1(b) shows an atomic force microscopy (AFM) landscape of this flake for confirming thickness, with the height profile along the dashed line shown in Figure 1(c). The tapping mode of AFM is used. A thickness of ~1 nm is found from the measurements, which is greater than the

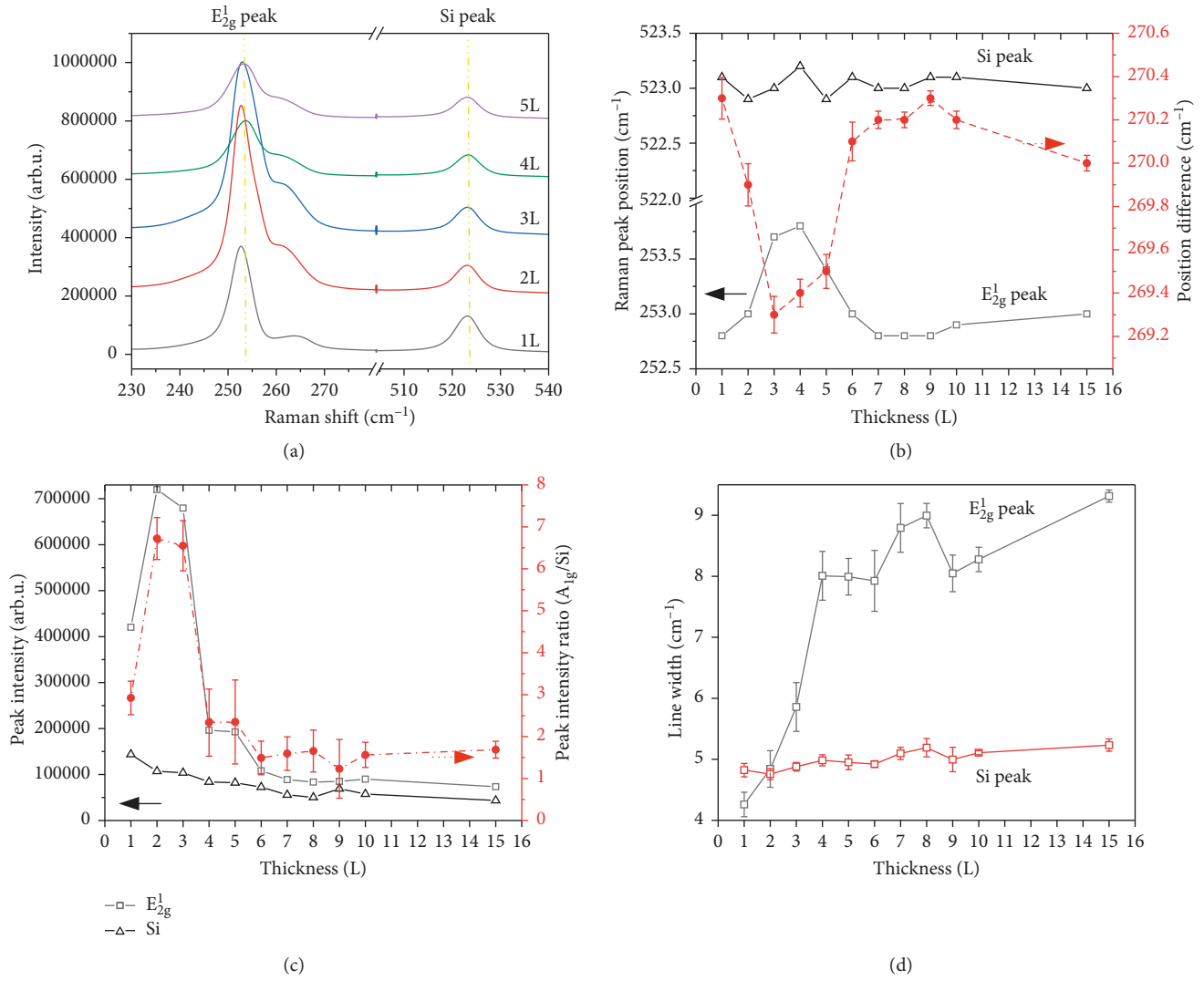

FIGURE 3: (a) Raman spectra of different layer numbers of WSe_2 supported by SiO_2 (285 nm)/Si substrate by 633 nm laser. (b) Raman peak position of WSe_2's E^1_{2g} peak and Si peak for different layer numbers (left vertical axis) and their difference (right vertical axis). (c) Raman peak intensity of WSe_2's E^1_{2g} peak and Si peak for different layer numbers (left vertical axis) and their ratio (right vertical axis). (d) Raman peak line width of WSe_2's E^1_{2g} peak and Si peak.

theoretical value of 0.65 nm but agrees with previous reports of AFM contact mode measurements [14, 27, 35]. For other layer numbers, flakes in other locations are used and confirmed by AFM using the same methodology. The AFM method is not practical for most applications due to the difficult and time-consuming device characterization process, which limits its applications in semiconducting industries, and the tip of AFM has a potential of damaging the sample. However, the nondestructive optical method is universal for semiconducting industrial applications, which is a more convenient, straightforward, safe, and accurate method.

3.2. Raman Spectroscopy. Laser used in the Raman measurement was focused on the $MoSe_2$ and WSe_2 flakes using the 100x objective lens with a numerical aperture of 0.90 and 1 mW laser power. Laser with a wavelength of 633 nm is used to provide a comprehensive characterization. For $MoSe_2$, A_{1g} Raman peak is the only observable peak and is the most visible and studied peak. Figure 2(a) shows the Raman spectra of $MoSe_2$ flakes measured by 633 nm laser from 1L to 5L. For each flake, two sharp peaks can be observed. The peak around 520 cm^{-1} (Figure 2(a)) comes from the Si substrate. Si-peak shift remains unchanged while the intensity changes due to the optical shielding from the different flakes that it is supporting. The peak around 243 cm^{-1} (Figure 2(a)) comes from the A_{1g} mode of $MoSe_2$, which is the most visible Raman mode for the study [35, 36]. The E_{2g} mode around 300 cm^{-1} is also weakly excited. However, because our goal is to find an easy way to distinguish the layer thickness, we choose to focus on the strongest A_{1g} Raman mode in this study. For both $MoSe_2$ and WSe_2, at least 3 samples for 1L–4L were measured. For each sample, we repeated the measurements 3 times. With this information, we calculated and obtained the error bars.

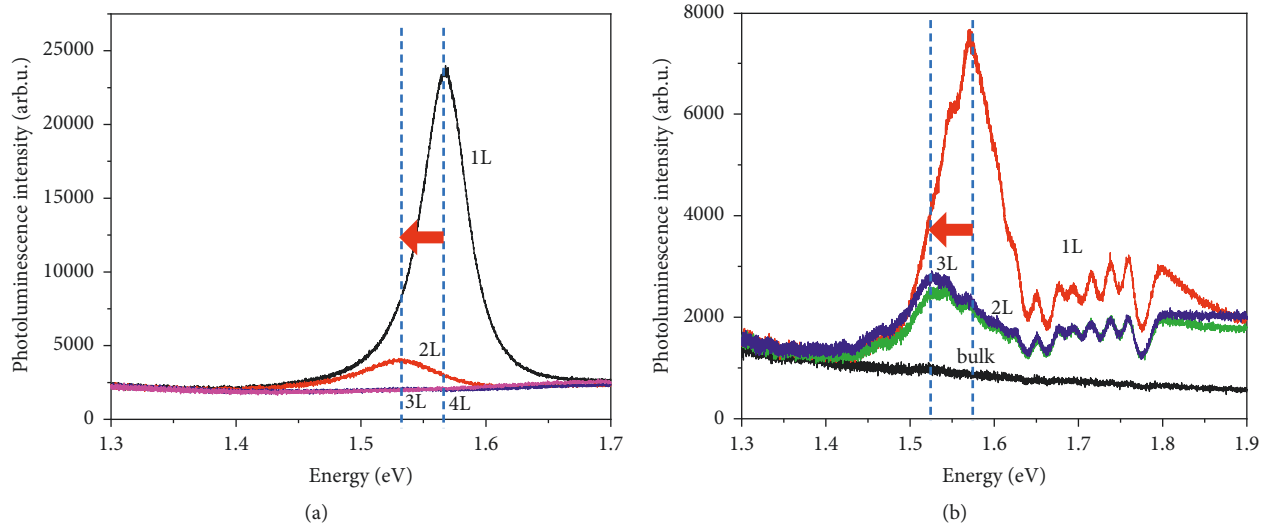

FIGURE 4: (a) Photoluminescence (PL) of 1L–4L $MoSe_2$. 1L $MoSe_2$ has highest PL intensity—stronger PL intensity indicates that bandgap transforms from indirect to direct. Bandgap increases with the decrease in thickness. (b) PL of 1L–3L and bulk WSe_2, with the same trend as $MoSe_2$.

Figures 2(b)–2(d) summarize the data for $MoSe_2$ from 1L to up to 12L. We find (Figures 2(a) and 2(b)) that the A_{1g} peak position shows a rapid increase as the layer number increases from 1L to 5L. This A_{1g} mode with a blue shift means the vibration stiffens with the increasing sample layer number. For films of 5L or more layers, the frequencies of A_{1g} mode converge to a constant value. In the meanwhile, the Si peak remains at the same position around 520.9 cm^{-1}. Due to Raman measurement's nature of drifting, usually another Raman peak is used and the difference between the two Raman peaks is used to characterize the layer number [13]. However, only one Raman peak is significant for $MoSe_2$; thus, the substrate Si's Raman peak which is measured simultaneously is used as reference to eliminate drifting during the measurements. The peak offsets are plotted in the main panel of Figure 2(b). When the layer number is up to 4, a monotonic decrease of the peak position difference is observed. Thus, our data show the capability of quantifying the layer number by the Raman peak offset between the A_{1g} peak and Si peak, which is facile and nondestructive and can avoid contact contamination and damage from AFM measurements. Also given that AFM sometimes yields different thicknesses for very thin layers (<4L) and is sensitive to sample-substrate impurities [14, 27, 35], Raman spectroscopy is used to characterize the collective dynamics of layered 2-D materials. Finally, when the layer number is greater than 4, the Raman peak shift remains unchanged, which serves as the limit of thickness characterization. As a result, for 1L $MoSe_2$, the Raman peak difference is larger than 278.5 cm^{-1}; for 2L $MoSe_2$ the Raman peak difference is larger than 278 cm^{-1}; and for 3L $MoSe_2$ the Raman peak difference is larger than 277.5 cm^{-1}.

Figure 2(c) shows the Raman peak intensity of $MoSe_2$'s A_{1g} peak and Si peak for different layer numbers and their ratio. Figure 2(d) shows the Raman peak line width of $MoSe_2$'s A_{1g} peak and Si peak. They both show distinctive variations as a function of film thickness and provide additional assistive information for layer thickness identification. The relative peak intensity between A_{1g} peak and Si peak has a monatomic increase with the layer number. Figure 2(d) presents the Raman peak line widths of both A_{1g} peak and Si peak. While peak position and intensity depend on the layer number, the peak line width is largely independent of layer number.

Figure 3(a) shows Raman spectra of WSe_2 using the same method by 633 nm laser. Figure 3(b) shows the Raman peak positions of WSe_2's E^1_{2g} peak and Si peak for different layer numbers and their difference. Figure 3(c) presents the Raman peak intensities of WSe_2's E^1_{2g} peak and Si peak for different layer numbers and their ratio. And Figure 3(d) shows the Raman peak line widths of WSe_2's E^1_{2g} peak and Si peak. In Figure 3(b), Si's Raman peak is also used as reference. For WSe_2, although there are two Raman peaks—E^1_{2g} and A_{1g}, they are not fully separated making peak position identification inaccurate; thus, the reference to the Si peak is needed. Here, the E^1_{2g} peak and Si peak's position difference are characterized on the WSe_2 samples of 1L–10L and 15L. It is clear that Raman spectroscopy could be used to characterize the layer number of WSe_2 when it is equal to or thinner than 3L based on their Raman peak shift, and by referencing peak intensity and line width, WSe_2 of 4L could be characterized. There is a limit of characterizing WSe_2 with layer number more than 4. As a result, for 1L WSe_2 the Raman peak difference is larger than 270 cm^{-1}, and for 2L WSe_2, the Raman peak difference is larger than 269.6 cm^{-1}. Again, the information of Raman peak intensities and line widths provides additional assistive information.

3.3. Photoluminescence and Electrical Characterization of the Sample. Figures 4(a) and 4(b) are the photoluminescence (PL) curves of 1L–4L $MoSe_2$ flakes and 1L–3L WSe_2 flakes with reference to the bulk sample. It provides more information for layer number and acts as an additional layer number identification engineering tool when there is a need. It has been found that bandgap increases with the decrease in

thickness, and the same trend has also been discovered for WSe_2, which conforms with the previous study [27]. The energy shift from 1L to 2L $MoSe_2$ is ~0.04 eV, and there is no PL peak observed for the sample with layer number larger than 3. The energy shift from 1L to 3L WSe_2 is ~0.05 eV. These two values provide information of characterizing layer numbers in addition to Raman spectroscopy using Si-peak analysis. It also conforms with the previous study [27] that 1L $MoSe_2$ has the strongest PL intensity, which indicates that bandgap transforms from indirect to direct. 1L $MoSe_2$'s PL result is in accordance with 1L MoS_2, which shows that it is a semiconducting material with direct bandgap and the bandgap decreases with the increase in layer number [11]. These physical properties provide an additional candidate to the semiconducting industry.

4. Conclusions

In this work, two atomically thin transition metal diselenide materials, $MoSe_2$ and WSe_2, with layer number from 1L to up to 15L have been studied by Raman spectroscopy, and the Si Raman peak from the substrate has been used as a reference for the precise characterization. By characterizing both the sample and substrate's Raman spectra, we are able to determine $MoSe_2$ and WSe_2's layer number for up to 4 layers. We believe that the Si-peak analysis remains the most powerful tool for determining the number of layers of $MoSe_2$ and WSe_2. Furthermore, this identification method can be exploited for van der Waals heterostructures made of various 2-D materials such as hBN and TMDCs, when substrate-related peaks are found and the relationship with the number of layers is verified. Their PL properties are also studied as additional information. It has been confirmed with the previous study that there is an enhanced PL in single-layer $MoSe_2$ and WSe_2 because of the transition from indirect to direct bandgap electronic structures, and the bandgap decreases with an increase in thickness. These results demonstrate more robust measurements of thickness of transition metal diselenide materials and provide potential of new optical and electrical applications of van der Waals semiconducting materials. In addition, the potential of combination of 2-D materials and other emerging materials such as organic materials will attract extensive attention from researchers in the organic, electronic, and nanotechnology communities.

Data Availability

The data used to support the findings of this study are available at https://www.dropbox.com/sh/3c1l292cqxcvz2l/AACuw8dw0_ClvYaTd0czZhdKa?dl=0.

Conflicts of Interest

The author declares no conflicts of interest.

Acknowledgments

This work is supported by the startup funding of the Stevens Institute of Technology.

References

[1] K. S. Novoselov, A. K. Geim, S. V. Morozov et al., "Electric field effect in atomically thin carbon films," *Science*, vol. 306, no. 5696, pp. 666–669, 2004.

[2] Y. Zhang, Y.-W. Tan, H. L. Stormer, and P. Kim, "Experimental observation of the quantum Hall effect and Berry's phase in graphene," *Nature*, vol. 438, no. 7065, pp. 201–204, 2005.

[3] Z. Yi, L. Liu, L. Wang et al., "Tunable dual-band perfect absorber consisting of periodic cross-cross monolayer graphene arrays," *Results in Physics*, vol. 13, article 102217, 2019.

[4] J. Huang, G. Niu, Z. Yi et al., "High sensitivity refractive index sensing with good angle and polarization tolerance using elliptical nanodisk graphene metamaterials," *Physica Scripta*, vol. 94, no. 8, article 085805, 2019.

[5] Z. Yi, J. Chen, C. Cen et al., "Tunable graphene-based plasmonic perfect metamaterial absorber in the THz region," *Micromachines*, vol. 10, no. 3, p. 194, 2019.

[6] K. S. Novoselov, D. Jiang, F. Schedin et al., "Two-dimensional atomic crystals," *Proceedings of the National Academy of Sciences*, vol. 102, no. 30, pp. 10451–10453, 2005.

[7] B. Radisavljevic, A. Radenovic, J. Brivio, V. Giacometti, and A. Kis, "Single-layer MoS_2 transistors," *Nature Nanotechnology*, vol. 6, no. 3, pp. 147–150, 2011.

[8] J. N. Coleman, M. Lotya, A. O'Neill et al., "Two-dimensional nanosheets produced by liquid exfoliation of layered materials," *Science*, vol. 331, no. 6017, pp. 568–571, 2011.

[9] Q. H. Wang, K. Kalantar-Zadeh, A. Kis, J. N. Coleman, and M. S. Strano, "Electronics and optoelectronics of two-dimensional transition metal dichalcogenides," *Nature Nanotechnology*, vol. 7, no. 11, pp. 699–712, 2012.

[10] G. Eda, H. Yamaguchi, D. Voiry, T. Fujita, M. Chen, and M. Chhowalla, "Photoluminescence from chemically exfoliated MoS_2," *Nano Letters*, vol. 11, no. 12, pp. 5111–5116, 2011.

[11] K. F. Mak, C. Lee, J. Hone, J. Shan, and T. F. Heinz, *Physical Review Letters*, vol. 105, no. 13, 2010.

[12] A. Splendiani, L. Sun, Y. Zhang et al., "Emerging photoluminescence in monolayer MoS_2," *Nano Letters*, vol. 10, no. 4, pp. 1271–1275, 2010.

[13] C. Lee, H. Yan, L. E. Brus, T. F. Heinz, J. Hone, and S. Ryu, "Anomalous lattice vibrations of single- and few-layer MoS_2," *ACS Nano*, vol. 4, no. 5, pp. 2695–2700, 2010.

[14] S. Tongay, J. Zhou, C. Ataca et al., "Thermally driven crossover from indirect toward direct bandgap in 2D semiconductors: $MoSe_2$ versus MoS_2," *Nano Letters*, vol. 12, no. 11, pp. 5576–5580, 2012.

[15] X. Zhang, D. Sun, Y. Li et al., "Measurement of lateral and interfacial thermal conductivity of single- and bilayer MoS_2 and $MoSe_2$ using refined optothermal Raman technique," *ACS Applied Materials & Interfaces*, vol. 7, no. 46, pp. 25923–25929, 2015.

[16] Y. Cao, V. Fatemi, S. Fang et al., "Unconventional superconductivity in magic-angle graphene superlattices," *Nature*, vol. 556, no. 7699, pp. 43–50, 2018.

[17] K. L. Seyler, P. Rivera, H. Yu et al., "Signatures of moiré-trapped valley excitons in $MoSe_2/WSe_2$ heterobilayers," *Nature*, vol. 567, no. 7746, pp. 66–70, 2019.

[18] K. Tran, G. Moody, F. Wu et al., "Evidence for moiré excitons in van der waals heterostructures," *Nature*, vol. 567, no. 7746, pp. 71–75, 2019.

[19] C. Jin, E. C. Regan, A. Yan et al., "Observation of moiré excitons in WSe_2/WS_2 heterostructure superlattices," *Nature*, vol. 567, no. 7746, pp. 76–80, 2019.

[20] S.-L. Li, H. Miyazaki, H. Song, H. Kuramochi, S. Nakaharai, and K. Tsukagoshi, "Quantitative Raman spectrum and reliable thickness identification for atomic layers on insulating substrates," *ACS Nano*, vol. 6, no. 8, pp. 7381–7388, 2012.

[21] S. Tongay, S. S. Varnoosfaderani, B. R. Appleton, J. Q. Wu, and A. F. Hebard, *Applied Physics Letters*, vol. 101, no. 12, article 123105, 2012.

[22] Y. Zhang, J. Ye, Y. Matsuhashi, and Y. Iwasa, "Ambipolar MoS_2 thin flake transistors," *Nano Letters*, vol. 12, no. 3, pp. 1136–1140, 2012.

[23] H. Li, Z. Yin, Q. He et al., "Fabrication of single- and multilayer MoS_2 film-based field-effect transistors for sensing NO at room temperature," *Small*, vol. 8, no. 1, pp. 63–67, 2012.

[24] Y. Zhang, T.-R. Chang, B. Zhou et al., "Direct observation of the transition from indirect to direct bandgap in atomically thin epitaxial $MoSe_2$," *Nature Nanotechnology*, vol. 9, no. 2, pp. 111–115, 2014.

[25] S. B. Desai, G. Seol, J. S. Kang et al., "Strain-induced indirect to direct bandgap transition in multilayer WSe_2," *Nano Letters*, vol. 14, no. 8, pp. 4592–4597, 2014.

[26] W. Zhao, R. M. Ribeiro, M. Toh et al., "Origin of indirect optical transitions in few-layer MoS_2, WS_2, and WSe_2," *Nano Letters*, vol. 13, no. 11, pp. 5627–5634, 2013.

[27] P. Tonndorf, R. Schmidt, P. Böttger et al., "Photoluminescence emission and Raman response of monolayer MoS_2, $MoSe_2$, and WSe_2," *Optics Express*, vol. 21, no. 4, p. 4908, 2013.

[28] C. Huang, S. Wu, A. M. Sanchez et al., "Lateral heterojunctions within monolayer $MoSe_2$-WSe_2 semiconductors," *Nature Materials*, vol. 13, no. 12, pp. 1096–1101, 2014.

[29] Y. Gong, S. Lei, G. Ye et al., "Two-step growth of two-dimensional WSe_2/$MoSe_2$ heterostructures," *Nano Letters*, vol. 15, no. 9, pp. 6135–6141, 2015.

[30] H. Fang, S. Chuang, T. C. Chang, K. Takei, T. Takahashi, and A. Javey, "High-performance single layered WSe_2 p-FETs with chemically doped contacts," *Nano Letters*, vol. 12, no. 7, pp. 3788–3792, 2012.

[31] Y. Niu, S. Gonzalez-Abad, R. Frisenda et al., "Thickness-dependent differential reflectance spectra of monolayer and few-layer MoS_2, $MoSe_2$, WS_2 and WSe_2," *Nanomaterials*, vol. 8, no. 9, p. 725, 2018.

[32] X. Li, Y. Shi, S. Li et al., "Layer-number dependent reflection spectra of MoS_2 flakes on SiO_2/Si substrate," *Optical Materials Express*, vol. 8, no. 10, pp. 3082–3091, 2018.

[33] N. S. Taghavi, P. Gant, P. Huang et al., "Thickness determination of MoS_2, $MoSe_2$, WS_2 and WSe_2 on transparent stamps used for deterministic transfer of 2D materials," *Nano Research*, vol. 12, no. 7, pp. 1691–1695, 2019.

[34] Y. No, H. Choi, J. Kim et al., "Layer number identification of CVD-grown multilayer graphene using Si peak analysis," *Scientific Reports*, vol. 8, no. 1, p. 571, 2018.

[35] X. Wang, Y. Gong, G. Shi et al., "Chemical vapor deposition growth of crystalline monolayer $MoSe_2$," *ACS Nano*, vol. 8, no. 5, pp. 5125–5131, 2014.

[36] X. Lu, M. I. B. Utama, J. Lin et al., "Large-area synthesis of monolayer and few-layer $MoSe_2$ films on SiO_2 substrates," *Nano Letters*, vol. 14, no. 5, pp. 2419–2425, 2014.

Hindawi
Advances in Materials Science and Engineering
Volume 2019, Article ID 7263721, 7 pages
https://doi.org/10.1155/2019/7263721

Research Article

An Estimation of the Thermal Properties of Pu-Rich Metallic Fuel

Naoya Odaira and Yuji Arita

University of Fukui, 1-3-33 Kanawa-cho, Tsuruga, Fukui 914-0055, Japan

Correspondence should be addressed to Yuji Arita; arita@u-fukui.ac.jp

Received 31 March 2019; Revised 25 July 2019; Accepted 2 August 2019; Published 4 September 2019

Guest Editor: Pradip Basnet

Pu-rich metallic fuel is promising for transuranic element burners. In this study, we calculated the thermal properties of Pu-rich metallic fuel. The thermal conductivity was calculated by using both Nordheim's rule and Wiedemann–Franz law. The thermal conductivity of Pu-40Zr (14.3 $Wm^{-1}{\cdot}K^{-1}$ at 600 K) was much lower than that of U-10Zr (23.5 $Wm^{-1}{\cdot}K^{-1}$ at 600 K), another candidate metallic fuel. This addresses the metallic fuel has much lower durability in accidental situations than U-Zr metallic fuel. Thus, we also calculated thermal conductivity of the Pu-20U-20Zr alloy. The result shows uranium addition to the Pu-Zr alloy increased the thermal conductivity. In addition, we calculated the melting point of the Pu-(0–80U)-20Zr alloy and the result shows uranium addition increased melting point. This result suggests the accident tolerance of the Pu-rich metallic fuel increases by adding uranium.

1. Introduction

Fast reactors can burn transuranic elements (TRUs; Pu, Np, Am, and Cm) effectively owing to their higher fission-to-neutron-capture ratio than light-water reactors (LWRs). LWRs will be the dominant nuclear power plants for at least the next few decades. To burn the TRUs produced from LWRs, it is necessary to improve the TRU burning capability of fast reactors. Because uranium TRU-fueled fast reactors also produce TRUs, the most effective approach is to use uranium-free TRU fuel because this does not produce additional TRUs. Such a system could reduce the capacity of the TRU burner units and the associated fuel cycle facilities to about 1/5 and 1/8, respectively. There have been many studies on uranium-free or fertile-free fuel systems [1–3]; however, difficulties remain, such as the requirement for new reprocessing technology. For example, reprocessing technology for producing TRU-burning oxide fuel is required to separate actinides and lanthanides, which have similar chemical behavior [4]. In addition, the remote control technology for reprocessing needs modifications because of high radioactivity of minor actinides. By contrast, uranium-free TRU metal could be reprocessed and fabricated based on pyroprocess and injection-casting technologies without substantial modification [5].

In the United States, many studies concerning uranium-free metal fuels have been carried out. Most notably, the US accelerator-driven transmutation of waste (ATW) program investigated an accelerator-driven transmutation system coupled with a subcritical fast reactor using uranium-free metal fuel [6–9]. In such systems, thermal properties, such as the heat capacity, thermal conductivity, and melting temperatures of the fuel, are important for the design of the core structure of the burning reactor.

In our previous study, we estimated the melting temperature of TRU-Zr alloys [10] and the thermal properties of Pu-rich alloys [11]. In the present study, we evaluate the thermal properties of Pu-40Zr (Pu-64at%Zr), a candidate material for TRU burners, and Pu-20U-20Zr (Pu-15at%U-40at%Zr) in a more relevant way.

2. Estimation of Thermal Properties

We calculated the heat capacity, thermal conductivity, and solidus and liquidus temperatures of the Pu-40Zr and the Pu-U-Zr alloys because experimental work with plutonium is difficult to obtain approval in Japan. The heat capacity of

alloys was estimated using the Neumann–Kopp law, which is equivalent to an additive law. Although the heat capacity varied considerably with phase changes, the estimated values for Pu-40Zr and Pu-20U-20Zr alloys were similar if their phases were the same.

Generally, the thermal conductivity at high temperatures is calculated from the heat capacity, thermal diffusivity, and density. The heat capacity and density are often estimated from the Neumann–Kopp law and Vegard's law. However, the thermal diffusivity is comparatively difficult to estimate because it varies significantly with composition, phase, and temperature. Another common way to estimate the thermal conductivity of metallic materials is to use the Wiedemann–Franz law, which multiplies the electrical conductivity, absolute temperature, and Lorentz number [12]. Unfortunately, however, the electrical conductivity of Pu-Zr alloys had not been reported. Nordheim's rule is a common way to estimate the electrical conductivity of element although its use is limited to alloys that form a solid solution. Fortunately, Pu-Zr and Pu-U-Zr alloys are considered to form a body-centered cubic (bcc) solid solution from related binary systems and the U-Pu-Zr ternary system [13, 14]. Therefore, the thermal conductivity of Pu-40Zr and Pu-20U-20Zr alloys was estimated using both the Wiedemann–Franz law and Nordheim's rule with the Nordheim coefficients.

Finally, we calculated the solidus and liquidus temperatures using Thermo-Calc, which is based on the CALPHAD method. The phase diagrams of the U-Zr, Pu-Zr, and U-Pu systems are available in the literature; thus, we calculated the liquidus and solidus temperatures by creating a pseudobinary system of the Pu-(0–80U)-20Zr alloy.

2.1. Heat Capacity. Figure 1 shows the data available in the literature for the U-Zr alloy [15] and the constituents: uranium, zirconium, and plutonium [16, 17]. There are anomalous peaks for the heat capacities of all three elements, which are caused by their phase transitions. The heat capacity of a compound can be estimated using the Neumann–Kopp (additive) law [18, 19]. Specifically, if a solid compound, M, is formed from elements A, B, and C by a chemical reaction:

$$aA + bB + cC \longrightarrow M, \tag{1}$$

then the heat capacity of the compound C_{PM} is expressed by the heat capacity of each element as follows:

$$C_{\mathrm{PM}} = aC_{\mathrm{PA}} + bC_{\mathrm{PB}} + cC_{\mathrm{PC}}. \tag{2}$$

The heat capacity of the U-Zr alloy measured by Matsui et al. [20] was similar to that calculated using the Neumann–Kopp law. Therefore, it may be possible to use it to determine the heat capacities of Pu-Zr and Pu-U-Zr alloys. Plutonium has many phase transitions, at which its heat capacity changes. For the Pu-Zr system created by Kurata [21], the Pu-40Zr alloy had two phases from room temperature to melting point, and the phase-transition temperature was approximately 902 K (Figure 2).

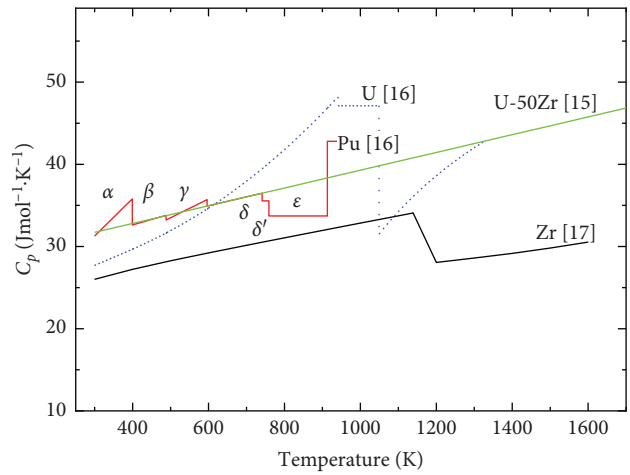

Figure 1: Literature data of the heat capacity of U-Zr and U, Zr, and Pu elements [15–17].

The low-temperature phase is a face-centered cubic (fcc) structure, and the high-temperature phase is a bcc structure. Below 902 K, the heat capacity of plutonium in our calculation was determined by interpolation and/or extrapolation of the value for the β and δ (fcc) phases. Above 902 K, the heat capacity was determined by extrapolation of the ε (bcc) phase. The heat capacity of zirconium was determined in a similar manner. Figure 3 shows the estimated heat capacity for Pu-40Zr and Pu-20U-20Zr alloys. For the Pu-20U-20Zr alloy, the phase-transition temperature was approximately 900 K, based on the available phase diagrams. The obtained fitting equations were as follows:

$$\begin{aligned}
{}_{\mathrm{Pu-Zr}}Cp\left(\mathrm{Jmol^{-1}\cdot K^{-1}}\right) &= 25.942 + 0.011614 \times T\,(\mathrm{K}) \\
&\quad - 1.5751 \times 10^{-6} \times T\,(\mathrm{K})^2 \\
&\quad : 298 < T < 902\,\mathrm{K} \\
&= 25.587 + 0.00246 \times T\ (K) \\
&\quad : 902 < T < 1330\,K, \\
{}_{\mathrm{Pu-U-Zr}}Cp\left(\mathrm{Jmol^{-1}\cdot K^{-1}}\right) &= 26.627 + 0.00995 \times T\,(\mathrm{K}) \\
&\quad + 2.92401 \times 10^{-6} \times T\,(\mathrm{K})^2 \\
&\quad : 298 < T < 900\,\mathrm{K} \\
&= 32.9715 - 0.00299 \times T\ (\mathrm{K}) \\
&\quad + 1.94196 \times 10^{-6}\,T\,(\mathrm{K})^2 \\
&\quad : 900 < T < 1330\ \mathrm{K}.
\end{aligned} \tag{3}$$

Although the phase transition temperature was different from the U-50Zr alloy, the value of Cp was not so different from it which has a similar ratio of zirconium with the Pu-40Zr alloy.

2.2. Thermal Conductivity. Wiedemann–Franz law is known as a specific rule in metallic elements, which connect thermal conductivity with electrical conductivity [12]:

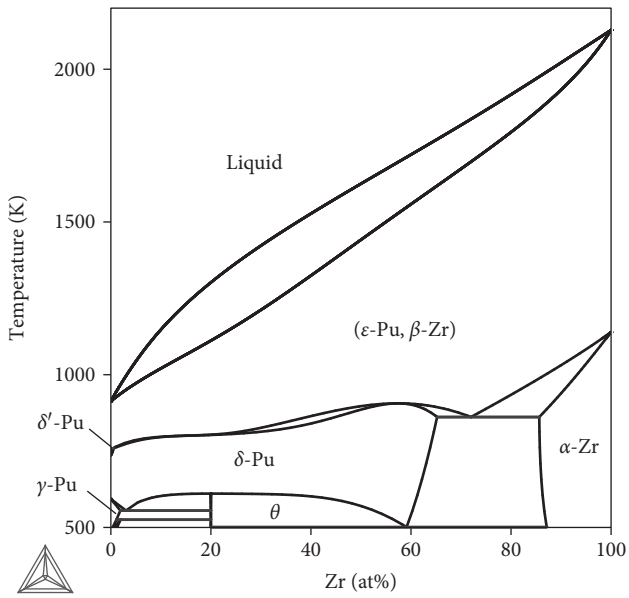

Figure 2: Phase diagram of the Pu-Zr system [21, 22].

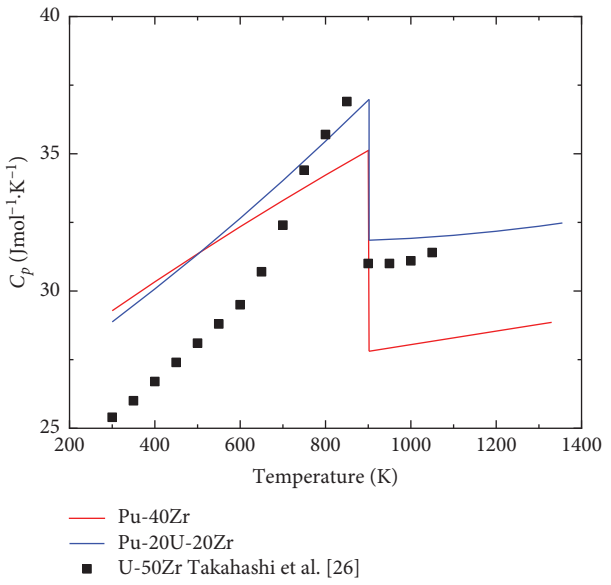

Figure 3: Estimated heat capacity of Pu-40Zr and Pu-20U-20Zr alloys.

$$\kappa = L\sigma T = \frac{\mathrm{LT}}{\rho}, \tag{4}$$

where κ is the thermal conductivity ($\mathrm{Wm^{-1}\cdot K^{-1}}$), σ is the electrical conductivity ($\Omega^{-1}\cdot\mathrm{m}^{-1}$), ρ is the electrical resistivity (Ωm), L is the Lorentz number, and T is the temperature (K). The Lorentz number is typically derived from the experimental measurement of thermal and electrical conductivity. However, it can also be derived from quantum mechanics, giving a value of $L = 2.44 \times 10^{-8}$ ($\mathrm{W\Omega K^{-2}}$), which is close to that of uranium, plutonium, and zirconium. Thus, we used this theoretical value of the Lorentz number in this study. For alloys form solid solution, Nordheim found that the electrical resistivity has a $x(1-x)$ dependence, as follows [23]:

$$\rho_m = \rho_A(1-x) + \rho_B x + cx(1-x), \tag{5}$$

where ρ_m, ρ_A, and ρ_B are the electrical resistivity of the mixture and elements A and B, x is the atomic fraction of element B, and c is the Nordheim coefficient, which is an element-dependent parameter. For example, for the Cu-Au alloy, the Nordheim coefficient of Cu-rich-Au alloys and Au-rich-Cu alloys are different [24]. Thus, we treated the Nordheim coefficients of the U-rich-Zr alloy and Zr-rich-U alloy separately in this paper.

From the Wiedemann–Franz law and Nordheim's rule, the thermal conductivity is considered to have the same dependence as the electrical conductivity [25]:

$$\kappa_1 = \frac{1}{(1-x)/\kappa_A + x/\kappa_B + c_1 x(1-x)/(\mathrm{LT})}, \tag{6}$$

where κ_1, κ_A, and κ_B are the thermal conductivity ($\mathrm{Wm^{-1}\cdot K^{-1}}$) of the mixture and elements A and B, respectively, x is the atomic fraction of element B, c_1 is the Nordheim coefficient, L is the Lorentz number, and T is the temperature. Because equation (5) only applies for binary alloys, we extended it to treat ternary alloys as a mixture of a binary alloy and third element as follows:

$$\kappa_2 = \frac{1}{(1-x)/\kappa_1 + x/\kappa_C + c_2 x(1-x)/(LT)}, \tag{7}$$

where κ_2, κ_1, and κ_C are the thermal conductivity ($\mathrm{Wm^{-1}\cdot K^{-1}}$) of the ternary alloy, binary alloy, and third element C, respectively, and x is the atomic fraction of element C. In our estimation, elements A, B, and C were U, Zr, and Pu, respectively, to obtain the Nordheim coefficients. To obtain the thermal conductivity of Pu-Zr and Pu-U-Zr, elements A, B, and C were Pu, Zr, and U, respectively.

The thermal conductivity of U-Zr and U-Pu-Zr alloys were taken from the work of Takahashi et al. [26] and reports from the Argonne National Laboratory (ANL) [27, 28]. These values were fitted into the above equations to obtain the Nordheim coefficients c_1 and c_2 for U-Zr and U-Pu-Zr alloys as temperature-dependent linear functions. To derive these functions, we fitted the temperature dependences of the thermal conductivity of uranium, zirconium, and plutonium using the following equation from available data [29, 30]:

$$\kappa = a + bT + cT^2 + dT^3. \tag{8}$$

Obtained fitting parameters are shown in Table 1. We obtained the thermal conductivity of Pu-Zr and Pu-U-Zr based on the assumption that their Nordheim coefficients were the same as those of U-Zr and U-Pu-Zr alloys. The Nordheim coefficients for U-Zr and U-Pu-Zr alloys are summarized in Table 2. In Figures 4 and 5, we compare the thermal conductivities obtained in the present study using the obtained Nordheim coefficients with those of the available data [26–28]. These show relatively close to measured thermal conductivity for both U-Zr and U-Pu-

Table 1: Fitted parameters for each element [29, 30].

	$\kappa = a + bT + cT^2 + dT^3$			
	a	b	c	d
U	3.739×10^{-6}	0.01837	−21.69	—
Zr	2.090×10^{-5}	−0.02515	27.48	—
Pu	-5.288×10^{-8}	6.439×10^{-5}	9.278×10^{-3}	−1.534

Table 2: Obtained Nordheim coefficients for U-Zr and U-Pu-Zr alloys.

		$c = a + bT$ (Nordheim coefficient)	
For published data	For estimation	a	b
Zr-rich (U-Zr alloy)	Pu-40Zr (Pu-64at%Zr)	7.985×10^{-6}	-7.436×10^{-9}
U-rich (U-Zr alloy)	—	1.581×10^{-6}	-1.619×10^{-9}
U-Zr-rich (U-Pu-Zr alloy)	Pu-20U-20Zr (Pu-15at%U-40at%Zr)	2.747×10^{-6}	-1.847×10^{-9}

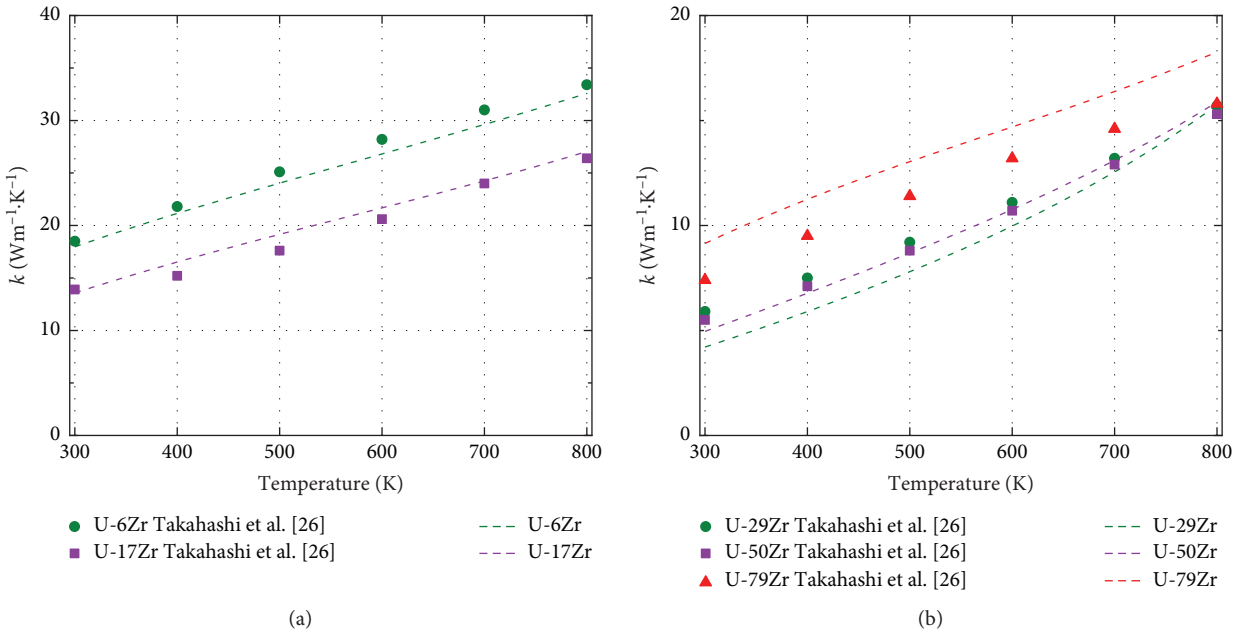

Figure 4: Comparison between the obtained thermal conductivity-temperature correlations (broken line) (present work) for (a) U-rich and (b) Zr-rich U-Zr alloys and the results of Takahashi et al. [26] (each point).

Zr alloys. For the U-79Zr alloy, our correlation showed higher thermal conductivity than experimental data. However, if zirconium content is below 50 wt%, our correlation showed sufficiently agreed well. Obtained Nordheim coefficients were based on these experimental data. These experimental data were only available below 1173 K, and this is the temperature limitation in the present experiment. The Pu-40Zr alloy had a significantly lower thermal conductivity than plutonium because of the effect of zirconium addition. However, the thermal conductivity of the Pu-20U-20Zr alloy was improved and it was close to that of plutonium because of the presence of uranium (Figure 6).

2.3. Solidus and Liquidus Temperatures. Solidus and liquidus temperatures of the Pu-U-Zr alloy (Pu-(0–80U)-20Zr) were calculated by Thermo-Calc [22] by creating a pseudo-binary phase diagram. Thermo-Calc is the calculation code based on the CALPHAD method, which creates phase diagrams and phase equilibria. A description of the CALPHAD method is provided elsewhere [31]. We used the database for the calculation to create U-Zr, Pu-Zr, U-Pu, and U-Pu-Zr systems based on the most recent data of the Gibbs free energy reported by Kurata [13, 14] although the Pu-rich region is not well understood in the U-Pu-Zr system. Verification of the database provided by Kurata is performed by D. E. Janney et al. [32]. There is no experimental data of the melting points for the Pu-U-Zr alloys, and thus, experimental measurement will be mandatory. To judge whether Pu-rich metallic fuel can be used in fast reactors, the system should be evaluated. Our results are shown in Figure 7, and fitting was performed with uranium content as follows:

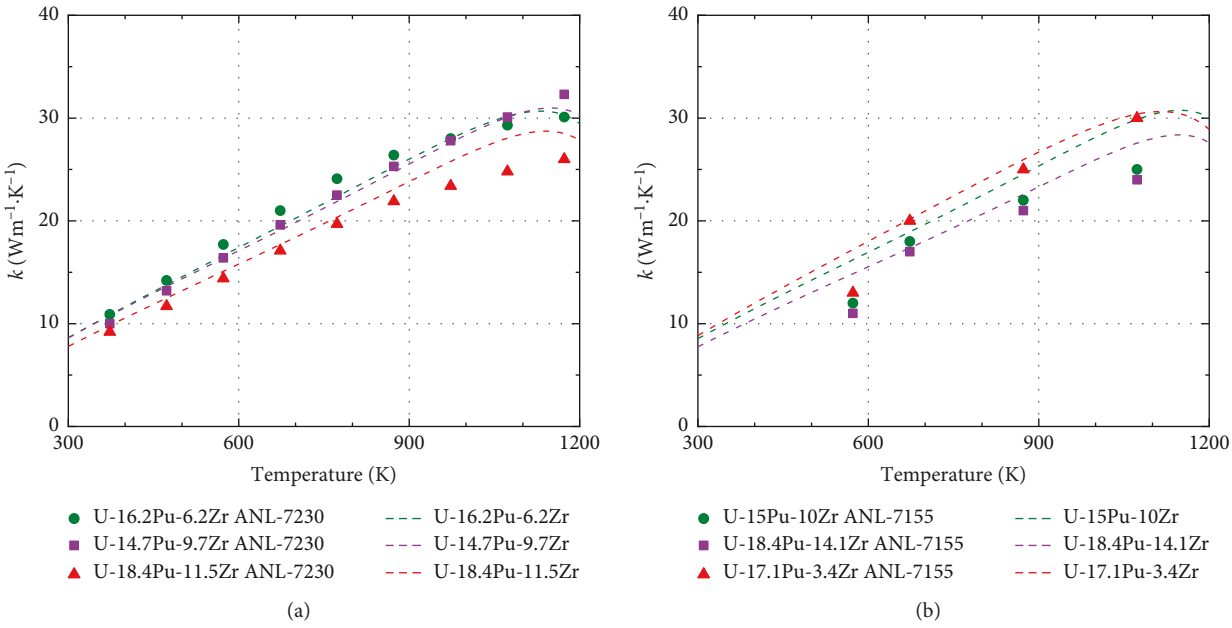

Figure 5: Comparison between the obtained thermal conductivity-temperature correlations (broken line) (present work) for the U-Pu-Zr alloy and data from (a) ANL-7230 (U-16.2Pu-6.2Zr, U-14.7Pu-9.7Zr, and U-18.4Pu-11.5Zr alloys (in wt%) and (b) ANL-7155 (U-15Pu-10Zr, U-18.4Pu-14.1Zr, and U-17.1Pu-3.4Zr [wt%] alloys (in wt%) [27, 28] (each point).

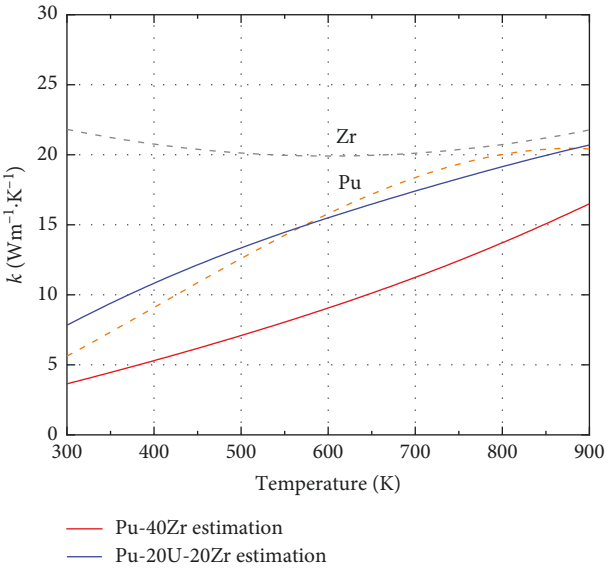

Figure 6: Estimated thermal conductivity of Pu-Zr and Pu-U-Zr alloys [29, 30].

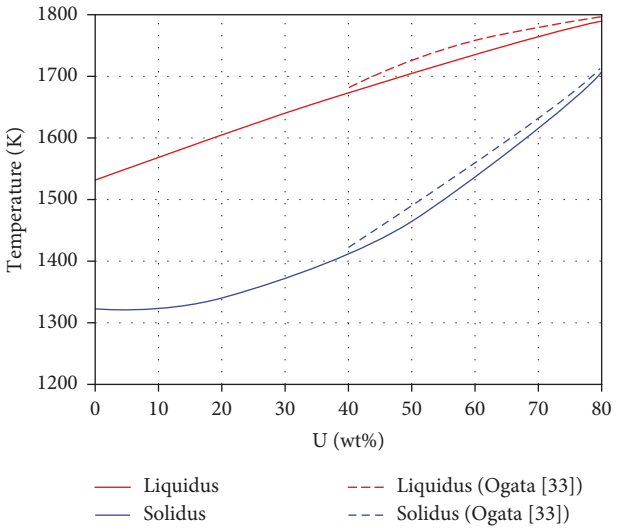

Figure 7: Estimated solidus and liquidus temperatures for the Pu-U-20Zr alloy [33, 34].

$$T_{\mathrm{liq}}(K) = 1530.5 + 385.07 \times W_{\mathrm{U}} - 77.635 \times W_{\mathrm{U}}^2,$$
$$T_{\mathrm{sol}}(K) = 1321.1 + 38.449 \times W_{\mathrm{U}} + 648.5 \times W_{\mathrm{U}}^2, \quad (9)$$

where T_{liq} and T_{sol} are the liquidus and solidus temperatures, respectively, and W_{U} is the weight fraction of uranium. Accordingly, both T_{liq} and T_{sol} increase with increasing uranium content. We calculated T_{liq} and T_{sol} values of 1321.1 and 1530.5 K for the Pu-20Zr alloy which were agreed well with the Pu-Zr system [13]. We also calculated them of 1705.4 and 1788.9 K for the U-20Zr alloy. These values were slightly lower than those for the U-20Zr alloy calculated by the correlation produced by Ogata, as shown in Figure 7 [33, 34].

3. Conclusion

U-free metallic alloy fuel has important advantages for use in TRU burners. Most importantly, we showed theoretically that the thermal conductivity of the Pu-40Zr alloy was lower than that of the U-Zr alloys, which limits the core power. This addresses the metallic fuel has much lower durability in

accidental situation than the U-Zr metallic fuel. To gain the safety margin, we also provided the estimation for the Pu-rich metallic fuel with small amount of uranium addition. However, the addition of uranium to the Pu-Zr alloy increased its thermal conductivity and solidus temperature. Despite these advantages, it should be noted that uranium addition could lead to lower efficiency in TRU burners.

Data Availability

No data were used to support this study.

Disclosure

Our previous work was presented in NuMat2018 at Seattle, entitled "An estimation of the thermal properties of Pu-rich metallic fuel," P1.008. This research was conducted as the Nuclear System Research and Development program under a contract with the Ministry of Education, Culture, Sports, Science and Technology (MEXT) in Japan during the fiscal year of 2014 to 2017. The title was "Innovative metallic fuel design and development of the production technology for TRU burning."

Conflicts of Interest

The authors declare that there are no conflicts of interest regarding the publication of this study.

Acknowledgments

We thank Adam Brotchie, PhD, from Edanz Group (http://www.edanzediting.com/ac)for editing a draft of this manuscript.

References

[1] T. Yamashita, H. Kuramoto, H. Akie et al., "Rock-like oxide fuels and their burning in LWRs," *Journal of Nuclear Science and Technology*, vol. 39, no. 8, pp. 865–871, 2002.

[2] M. Osaka, S. Hiroyuki, M. Kato et al., "Research and development of minor actinide-containing fuel and target in a future integrated closed cycle system," *Journal of Nuclear Science and Technology*, vol. 44, no. 3, pp. 309–316, 2007.

[3] N. Messaoudi and J. Tommasi, "Fast burner reactor devoted to minor actinide incineration," *Nuclear Technology*, vol. 137, no. 2, pp. 84–96, 2002.

[4] OECD/NEA, *State-of-the-Art Report on the Progress of Nuclear Fuel Cycle Chemistry*, NEA. No.7267, Paris, France, 2018.

[5] K. Arie, Y. Tsuboi, A. Hara, Y. Arita, and H. Ohta, "Fast reactors and related fuel cycles: next generation nuclear systems for systainable development FR17," in *Proceedings of the IAEA (International Atomic Energy Agency)*, Yekaterinburg, Russian Federation, June 2017.

[6] R. N. Hill and H. S. Khalil, *Emerging Nuclear Energy and Transmutation Systems: Core Physics and Engineering Aspects*, Argonne National Laboratory, Lemont, IL, USA, 2000.

[7] D. E. Beller, G. J. Van Tuyle, D. Bennett et al., "The U.S. accelerator transmutation of waste program," *Nuclear Instruments and Methods in Physics Research Section A: Accelerators, Spectrometers, Detectors and Associated Equipment*, vol. 463, no. 3, pp. 468–486, 2001.

[8] F. Heidet, T. K. kim, and T. A. Taiwo, "Thorium-fueled breed and burn core with low enriched uranium support," in *2013 ANS Winter Meeting*, Washington, DC, USA, November 2013.

[9] M. K. Meyer, "Fuel design for the U.S. accelerator driven transmutation system," in *Paper Presented at the Nuclear Application in the New Millennium*, Reno, NV, USA, November 2001.

[10] Y. Arita, Y. Tsuboi, and H. Ohta, *Innovative TRU Burning Fast Reactor Cycle Using Uranium-Free TRU Metal Fuel (2) Fundamental Properties of Uranium-free TRU-Zr Metal Fuel*, GLOBAL2015, Paris, France, 2015.

[11] N. Odaira and Y. Arita, "An estimation of the thermal properties of Pu-rich metallic fuel," in *Proceedings of NuMat2018*, Seattle, WA, USA, October 2018.

[12] R. Franz and G. Wiedemann, "Ueber die wärme-leitungsfähigkeit der metalle," *Annalen der Physik und Chemie*, vol. 165, no. 8, pp. 497–531, 1853.

[13] M. Kurata, "Phase Diagrams of Actinide Alloys, no. 2.05," in *Comprehensive Nuclear Materials*, Elsevier, Amsterdam, Netherlands, 2012.

[14] M. Kurata, "Thermodynamic assessment of the Pu-U, Pu-Zr, and Pu-U-Zr systems," *Calphad*, vol. 23, no. 3-4, pp. 305–337, 1999.

[15] Y. Takahashi, K. Yamamoto, T. Ohsato, H. Shimada, T. Terai, and M. Yamawaki, "Heat capacities of uranium-zirconium alloys from 300 to 1100 K," *Journal of Nuclear Materials*, vol. 167, pp. 147–151, 1989.

[16] R. J. M. Konings and O. Beneš, "The thermodynamic properties of the f-elements and their compounds. I. The lanthanide and actinide metals," *Journal of Physical and Chemical Reference Data*, vol. 39, no. 4, Article ID 043102, 2010.

[17] E. H. P. Cordfunke and R. J. M. Konings, *Themochemical Data for Reactor Materials and Fission Products*, North-Holland, Amsterdam, Netherlands, 1990.

[18] J. Leitner, P. Voňka, D. Sedmidubský, and P. Svoboda, "Application of Neumann-Kopp rule for the estimation of heat capacity of mixed oxides," *Thermochimica Acta*, vol. 497, no. 1-2, pp. 7–13, 2010.

[19] H. Kopp, "Investigations of the specific heat of solid bodies," *Philosophical Transactions of the Royal Society of London*, vol. 155, pp. 71–202, 1865.

[20] T. Matsui, T. Natsume, and K. Naito, "Heat capacity measurements of U0.80Zr0.20 and U0.80Mo0.20 alloys from room temperature to 1300 K," *Journal of Nuclear Materials*, vol. 167, pp. 152–159, 1989.

[21] M. Kurata, *Innovative nuclear research and development program*, Technical Report, Japan Science and Technology Agency (JST), Kawaguchi, Japan, 2007.

[22] https://www.thermocalc.com/.

[23] L. Nordheim, "Zur elektronentheorie der Metalle. II," *Annalen der Physik*, vol. 401, no. 6, pp. 641–678, 1931.

[24] S. Kasap and P. Capper, *Springer Handbook of Electronic and Photonic Materials*, Springer International Publiching, Basel, Switzerland, 2017.

[25] Y. Terada, K. Ohkubo, T. Mohri, and T. Suzuki, "Thermal conductivity in nickel solid solutions," *Journal of Applied Physics*, vol. 81, no. 5, pp. 2263–2268, 1997.

[26] Y. Takahashi, M. Yamawaki, and K. Yamamoto, "Thermophysical properties of uranium-zirconium alloys," *Journal of Nuclear Materials*, vol. 154, p. 4, 1988.

[27] A. V. Crewe and S. Lawroski, *Reactor Development Program Progress Report*, Argonne National Laboratory, ANL-7230, Lemont, IL, USA, 1966.

[28] Argonne National Laboratory, *Annual Progress Report for 1965*, Argonne National Laboratory, ANL-7155, Lemont, IL, USA, 1965.
[29] Y. S. Touloukian, *TPRC Data Series Vol. 1 Thermal Conductivity*, IFI/Plenum Press, New York, NY, USA, 1970.
[30] C. A. Alexander and V. E. Wood, "Thermal conductivity of plutonium above room temperature," *Journal of Applied Physics*, vol. 103, no. 6, 2008.
[31] K. Hack, *The SGTE Case Book-Thermodynamics at Work*-, ISBN 978-1-84569-215-5, CRC Press LLC, Boca Raton, FL, USA, 2008.
[32] D. E. Janney, C. A. Papesch, and S. C. Middlemas, *FCRD Advanced Reactor (Transmutation) Fuels Handbook, INL/EXT-15-36520*, Idaho National Laboratory, Idaho Falls, ID, USA, 2016.
[33] T. Ogata, "Irradiation behavior and thermodynamic properties of metallic fuel," *Journal of Nuclear Science and Technology*, vol. 39, no. 3, pp. 675–681, 2002.
[34] T. Ogata, "Metal Fuel, no. 3.01," in *Comprehensive Nuclear Materials*, Elsevier, Amsterdam, Netherlands, 2012.

Hindawi
Advances in Materials Science and Engineering
Volume 2019, Article ID 9504198, 15 pages
https://doi.org/10.1155/2019/9504198

Research Article

Synthesis of Mesoporous TiO_2 Spheres via the Solvothermal Process and Its Application in the Development of DSSC

S. Velázquez-Martínez,[1] **S. Silva-Martínez**,[2] **A. E. Jiménez-González**,[3] **and A. Maldonado Álvarez**[4]

[1]*Posgrado en Ingeniería y Ciencias Aplicadas, Universidad Autónoma del Estado de Morelos, Av. Universidad 1001, Col. Chamilpa, Cuernavaca, Morelos C.P. 62209, Mexico*
[2]*Centro de Investigación en Ingeniería y Ciencias Aplicadas, Universidad Autónoma del Estado de Morelos, Av. Universidad 1001, Col. Chamilpa, Cuernavaca, Morelos C.P. 62209, Mexico*
[3]*Instituto de Energías Renovables, IER-UNAM, Temixco, Morelos C.P. 62580, Mexico*
[4]*CINVESTAV–IPN, Departamento de Ingeniería Eléctrica-SEES, Av. Instituto Politécnico Nacional 2508, Ciudad de México C.P. 07360, Mexico*

Correspondence should be addressed to A. E. Jiménez-González; ajg@ier.unam.mx

Received 12 April 2019; Accepted 1 July 2019; Published 2 September 2019

Guest Editor: Pradip Basnet

This study examined the synthesis of the *n*-type nanostructured titanium dioxide semiconductor using a combined sol-gel/solvothermal method at 200°C, varying the concentrations of H_2O and HCl used as a catalyst for the hydrolysis of the titanium isopropoxide precursor. A white powder of TiO_2 nanoparticles was obtained via the solvothermal process. Scanning electron microscopy revealed a spherical morphology of the TiO_2 nanoparticles, with their diameter ranging from 2 to 7 microns as the HCl concentration increases. High-resolution electron microscopy and X-ray diffraction showed that the spheres are mesoporous titanium oxide ($TiO_2{}^m$) composed of nanocrystals with an anatase crystalline phase whose crystallite diameter grows from 8 to 13 nm as the HCl concentration increases. On the contrary, optimizing the H_2O concentration enabled a decrease in the crystallite size of $TiO_2{}^m$ and increases in the surface area and the energy band gap of $TiO_2{}^m$. The enlarged surface area enabled an increase in the number of contact points between $TiO_2{}^m$ and the dye of dye-sensitized solar cells (DSSCs), resulting in a better solar cell performance. The white powder was used to prepare a $TiO_2{}^m$ film via the screen-printing technique, which was used in the development of DSSC. The performance parameters of the DSSC (I_{SC}, V_{OC}, FF, and η%) were correlated with the synthesis parameters of $TiO_2{}^m$. This correlation showed that H_2O and HCl greatly influence the semiconductor properties of $TiO_2{}^m$, along with the short-circuit current J_{SC} and the conversion efficiency η% of the DSSC.

1. Introduction

Dye-sensitized solar cells (DSSCs) were developed at the beginning of the 90s [1], and today, they represent a mature technology with high marketing potential due to their acceptable stability, high performance under different lighting conditions, relatively low cost of production, and low toxicity [2–4]. The principle of operation of these cells is based on the separation of electrical charge by the junction between semiconductor materials with different electrical conductivities [5]. The active electrode of a DSSC uses an *n*-type mesoporous oxide semiconductor with a large surface area as its main component—in most cases, titanium oxide (TiO_2)—whose crystalline anatase phase is most often used [6–11].

A DSSC has a structure of the type SnO_2 : F/$TiO_2{}^c$/$TiO_2{}^m$/N719/$I^-/I_3{}^-$/Pt/SnO_2 : F, where SnO_2 : F represents a transparent conductor of high electrical conductivity and optical transmittance, $TiO_2{}^c$ is a thin layer of TiO_2 called the compact layer, $TiO_2{}^m$ is a mesoporous *n*-type semiconductor layer, N719 is a ruthenium dye, $I^-/I_3{}^-$ is the redox pair, and Pt/SnO_2 : F represents a platinum counter electrode deposited on the transparent conductor SnO_2 : F.

During the preparation of the DSSC, the TiO_2^m layer is sensitized with a dye (e.g., N719, N3, or organic dyes) to absorb electromagnetic radiation from the sun.

During the electromagnetic excitation from the HOMO (highest occupied molecular orbital) level to the LUMO (lowest unoccupied molecular orbital) level of the N719 dye, an electron is created at the LUMO level and a hole is formed at the HOMO level. From the LUMO level, the electron is rapidly injected into the conduction band of TiO_2^m and transferred to $SnO_2:F$ through TiO_2^c for subsequent extraction to an external circuit connected to the DSSC [3, 12–15]. To regenerate the ionized HOMO level, it is necessary to transfer an electron to that state from the redox pair (for example, I^-/I^{3-} or Co^{2+}/Co^{3+}), which donates electrons to restore the original state of the dye [3]. To regenerate the redox pair I^-/I^{3-}, the $Pt/SnO_2:F$ counter electrode consisting of a thin layer of platinum functioning as a catalyst is used to facilitate electron collection [16]. Once the photogenerated electrons are injected into the conduction band of TiO_2^m, they are quickly transported to the external circuit, producing an electric current based on a test charge and arriving at the $Pt/SnO_2:F$ counter electrode. Finally, to complete the cycle, the electrons collected in the counter electrode are ready to start a new regeneration cycle of the redox pair [3, 17].

The efficiency of a DSSC depends on the individual performance of each component layer [18, 19]. The semiconductor properties of TiO_2^m are essential in determining the performance of the DSSC. However, these properties depend to a large extent on solid state properties, such as the crystalline phase, crystallite size, porosity, surface area, surface morphology, and electrical conductivity, which depend on the chemical reaction occurring during TiO_2^m synthesis [20]. The crystalline anatase phase of TiO_2^m is one of the most often used phases in preparing DSSC because it allows relatively high conversion efficiencies to be obtained [21–23].

The solvothermal method has widely been used in the synthesis of the nanoparticles of semiconductor materials [24–28]. If water is used as a solvent, the method is known as "hydrothermal synthesis," whereas if some alcohol is used, the process is known as "solvothermal synthesis." Both processes are used to prepare various semiconductor materials of different geometries, such as micro- and nanostructured powders. In addition, it is possible to control the morphology (sphere (3D), rod (2D), or wire (1D)) of the crystals formed via solvent supersaturation, the chemical concentration of the reagents used, and kinetic control [29].

TiO_2^m has a relatively large surface area, allowing greater dye and photon adsorption. Among the different mesoporous nanostructured materials, the synthesis of TiO_2^m spheres—TiO_2^m nanocrystals brought together into spherical assemblies—having a larger surface area than some nanotube and nanowire systems has been demonstrated [30].

Several methods for preparing TiO_2^m spheres using different variations of the solvothermal method have been published in the literature. A characteristic of these synthesis methods is that mesoporous spheres are formed in two steps: (a) formation of TiO_2^m spheres during a sol-gel process and (b) subjection of these spheres to a solvothermal process in an autoclave at temperatures between 150 and 200°C [31–35]. For example, some authors synthesized TiO_2^m precursor spheres from a sol-gel solution in the presence of hexadecylamine, then dried them in the air, and finally subjected them to solvothermal treatment in a mixture of water and ethanol [31, 32]. Another method used to form titania (anatase-rutile) spheres is to add titanium tetraisopropoxide to ethylene glycol to form a white suspension, drying it at 80°C for 10 h. The spheres obtained using this method are dispersed in water and ethanol, placed in an autoclave, and thermally treated at 150°C for 12 h [33]. Another synthesis method of TiO_2^m microspheres is the thermal hydrolysis of titanium sulfate, dissolving it later in *n*-propanol and water, and then performing the solvothermal reaction [34]. The synthesis of TiO_2^m microspheres starting from titanium isopropoxide mixed with anhydrous acetone at ambient conditions is also possible by subjecting the mixture to a solvothermal process at 200°C for 12 h [35].

In the present study, the synthesis of TiO_2^m spheres is performed via a sol-gel/solvothermal process, in which the structural, morphological, optical, and electrical properties of the spheres are essentially studied according to the concentration of hydrochloric acid (as a catalyst for the hydrolysis of the titanium isopropoxide precursor), the H_2O content, and the temperature during the synthesis. Specifically, the surface area of TiO_2^m, pore size distribution, crystallite size, and forbidden energy band gap E_g are studied. This study also examines the application of TiO_2^m in the development of DSSC and the performance parameters (short-circuit current I_{SC}, open-circuit voltage V_{OC}, fill factor FF, and conversion efficiency η%) as a function of the synthesis parameters of the *n*-type TiO_2^m semiconductor.

2. Experimental Section

2.1. Chemical Reagents. To prepare the different component layers of the DSSC, the following reagents and materials were used.

Titanium isopropoxide (Sigma-Aldrich), ethyl alcohol absolute (Fermont), acetone absolute (Fermont), hydrochloric acid (J. T Baker 36.6–38%), and deionized water (Milli®85-Q/RIO) were used. $SnO_2:F$ (FTO) of 15 and 8 ohm per square (TEC15 Pilkington group), terpineol (mixture of isomers anhydrous, Sigma-Aldrich), ethyl cellulose (Sigma-Aldrich), ruthenium dye N719 (Ruthenizer 535-bis TBA Solaronix), polymer Surlyn® (Meltonix 1170-60 Solaronix), and Platinum Paste-PT-1 (Dyesol) electrolyte (Iodolyte HI-30) were also used.

2.2. Deposition of DSSC Films and Cell Assembly

2.2.1. TiO_2^c Layer. To prepare the thin film called the TiO_2^c blocking layer, a mixture of 2.0 mL of deionized water (H_2O) with 93.5 mL of ethanol was stirred in a two-neck flat-bottomed flask, adding 1.5 mL of hydrochloric acid (HCl) as a catalyst for the hydrolysis of the titanium isopropoxide precursor $Ti[OCH(CH_3)_2]_4$ ($Ti(OC_3H_7)_4$) [36–38]. After 20 minutes of stirring, 3 mL of titanium isopropoxide was

added dropwise to the above solution, which was then stirred for 24 h. During the said addition, the titanium precursor is hydrolyzed, forming a sol, to later form the polymer chains of the fully hydrolyzed $Ti(OH)_4$ monomer and thereby form the gel [39]. Using dip coating equipment, 3 depositions are performed on a transparent conductive glass substrate of SnO_2 : F (FTO) with resistivity 15 Ω/□. Subsequently, the substrate is calcined in air at 450°C, where the metal hydroxide is transformed into a titanium oxide film with a thickness of approximately 200 nm. In this way, a SnO_2 : $F/TiO_2{}^c$ junction is obtained.

2.2.2. Synthesis of $TiO_2{}^m$ Nanoparticles via a Sol-Gel/Solvothermal Method

(1) Sol-Gel Process. To prepare $TiO_2{}^m$ nanoparticles, a mixture of 1.9 mL of deionized water (H_2O) with 115.5 mL of ethanol was stirred in a two-neck flat-bottomed flask, adding hydrochloric acid (HCl) as a catalyst for the hydrolysis [36–38]. The volume of HCl was adjusted to obtain 0.5, 1, 1.5, 2, 2.5, and 3% (v/v) concentrations in relation to the total solution volume. After 20 minutes of stirring, 20.73 mL of titanium isopropoxide was added dropwise to the above solution, which was then stirred for 24 h.

(2) Solvothermal Process. After the sol-gel process, the solution was placed in an autoclave and thermally treated for 12 h at 200°C and a pressure of 54 atm. Then, the autoclave was allowed to cool to room temperature, and the solution resulting from the solvothermal process was centrifuged at 4000 rpm for 20 min. Subsequently, the obtained nanoparticles were washed in anhydrous ethanol and then centrifuged at 7000 rpm. This washing process was repeated twice more.

2.2.3. Preparation of the $TiO_2{}^m$ Layer. Using the $TiO_2{}^m$ nanoparticles obtained via the solvothermal method explained in the previous section, a paste was prepared with 0.5 g of $TiO_2{}^m$ mixed with 4.0 g of terpineol as a dispersing agent and 2 mL of acetone; this paste was placed in an ultrasound bath for 1 h to avoid nanoparticle agglomeration and lump formation. In another container, 0.15 grams of ethyl cellulose were weighed and mixed with 8 mL of ethanol, and the mixture was also placed in an ultrasound bath for 1 h. Subsequently, both solutions were mixed, and the ethanol was extracted using a rotary evaporator. The remaining paste was deposited using the screen-printing technique on the SnO_2 : $F/TiO_2{}^c$ junction to obtain a SnO_2 : $F/TiO_2{}^c/TiO_2{}^m$ heterojunction with an area of $0.5 \times 1.0\ cm^2$, which was thermally treated at 530°C for 1 h. Ethyl cellulose was added to create pores in the $TiO_2{}^m$ layer during the thermal treatment.

2.2.4. N-719 Dye. Sensitization of $TiO_2{}^m$ at the SnO_2 : $F/TiO_2{}^c/TiO_2{}^c/TiO_2{}^m$ heterojunction was performed by immersion for 24 h in a 0.5 mM solution of N-719 ruthenium dye in ethanol, which is based on ruthenium-bipyridyl complexes. The N-719 ruthenium dye from Solaronix has the following molecular structure: $C_{58}H_{86}O_8N_8S_2Ru$. To sensitize the *n*-type $TiO_2{}^m$ semiconductor, the dye needs to have the capacity to adhere strongly to the surface of $TiO_2{}^m$, which is achieved through the carboxylic groups of the N-719 dye. The sensitized SnO_2 : $F/TiO_2{}^c/TiO_2{}^m$/dye heterojunction is known as the working electrode because a DSSC constitutes a photoelectrochemical cell.

2.2.5. $I^-/I_3{}^-$ Redox Pair. An electrolyte in a liquid state is a fluid containing ions carrying electric charges. The I^-/I^{3-} redox pair was used in this project and is commonly used for these types of cells [40]. To prepare the electrolyte, solutions of lithium salts (lithium iodide), iodine, and 4-tert-butylpyridine dissolved in acetonitrile are usually mixed. The electrolytic solution (lodolyte HI-30 from Solaronix) is placed in the solar cell to regenerate the dye after it has provided an electron to the $TiO_2{}^m$ conduction band; thus, the electrolyte is the medium allowing the oxidized dye to regenerate and, under electromagnetic excitation, continue injecting electrons into the semiconductor.

2.2.6. Counter Electrode. A platinum film is deposited on SnO_2 : F to generate the Pt/SnO_2 : F counter electrode of the solar cell, considering that Pt is used to expedite electrolyte regeneration. Using the screen-printing technique, a platinum paste (Platinum Paste-PT-1 from Dyesol) was applied on SnO_2 : F, allowed to dry for 30 min at room temperature and then thermally treated at 450°C for 1 h.

2.2.7. DSSC Assembly. To assemble the solar cells studied here, the working electrode was placed with the dye facing up; a spacer (Surlyn® Polymer) was placed with a tweezer to avoid electrical contact between the $TiO_2{}^m$ layer and the counter electrode. Previously, Surlyn® was cut in the form of a frame to cover the area around the $TiO_2{}^m$ layer (1.2 cm × 0.7 cm). Then, the counter electrode was placed on the working electrode so that Surlyn was sandwiched between the glasses as shown in Figure 1.

This arrangement was introduced into a muffle furnace at 215°C for 90 s, then removed from the furnace, and allowed to cool at room temperature for 5 min. Subsequently, the electrolytic solution was injected into the cell through a pair of holes previously drilled in the counter electrode. Finally, silver paint was placed on the ends of the cell for better conductivity in measuring its parameters.

2.3. Experimental Equipment. To study the crystalline phase and crystallite size of the *n*-type $TiO_2{}^m$ semiconductor prepared in this study, we used a Rigaku X-ray diffractometer DMAX-2200, which uses the K_α line ($E = 1.5405$ Å) of a copper anode. The crystallite size of $TiO_2{}^m$ was determined using the Scherrer equation:

$$D = \frac{0.94\lambda}{B\cos\theta}, \quad (1)$$

where λ is the X-ray wavelength, B (2θ) is the full-width at half-maximum intensity (FWHM), and θ is the diffraction

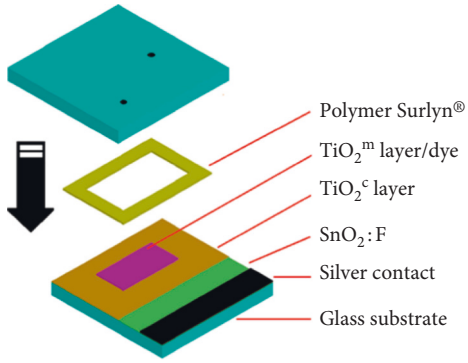

Figure 1: Cell assembly using a Surlyn polymer.

angle. To study the surface morphology of TiO_2^m, micrographs were obtained by field emission scanning electron microscopy (FE-SEM Hitachi S-5500). Reflectance and optical transmittance analyses were performed with a SHIMADZU UV-3101 spectrophotometer. These analyses were then used to calculate the size of the forbidden energy band gap E_g [41]. For the measurement of the I-V curves, a Keithley 236 Source-Measure Unit coupled with the SLB-150A Compact Solar Simulator Class AAA from SCIENCETECH and equipped with a UXL-150S0 Xenon short-arc lamp and an AM Air Mass Filter, was used. The specific surface area (SSA) was calculated using the BET method on a Quantachrome Autosorb 1. Before nitrogen adsorption, the oven-dried and dispersed sample was placed on a Quantachrome 9 mm cell and outgassed at 100°C for 24 h to remove any adsorbed water after storage and transport of the sample. Nitrogen adsorption isotherms were programmed with a 44 data point collection, of which the first 11 were used for SSA calculations.

3. Results and Discussion

3.1. Influence of HCl as a Catalyst for Hydrolysis on the Synthesis of TiO_2^m Nanoparticles. During the synthesis of TiO_2^m nanoparticles via the solvothermal method, the volume of HCl (experimental parameter) as a catalyst for hydrolysis was varied in relation to the total solution volume (% (v/v)) according to the following values: 0.5, 1.0, 1.5, 2.0, 2.5, and 3.0% (v/v). The H_2O concentration was fixed during this process at 1.9% (v/v). The TiO_2^m nanoparticles prepared using this method were characterized by X-ray diffraction and FE-SEM. This experiment showed that HCl, as a catalyst for the hydrolysis of titanium isopropoxide, plays a fundamental role in the properties of TiO_2^m nanoparticles synthesized during the sol-gel/solvothermal process as described below.

3.1.1. TiO_2^m Nanoparticles Prepared via the Solvothermal Process at 200°C. Figure 2 shows the X-ray diffraction patterns of TiO_2^m for each HCl concentration used (0.5 to 3.0% (v/v)) during the solvothermal processes at 200°C. A dominant peak at an angle of $2\theta = 26.1°$ corresponding to the (101) plane of the pure anatase crystalline phase—according to the *Powder Diffraction File* database card # 21-1272—and

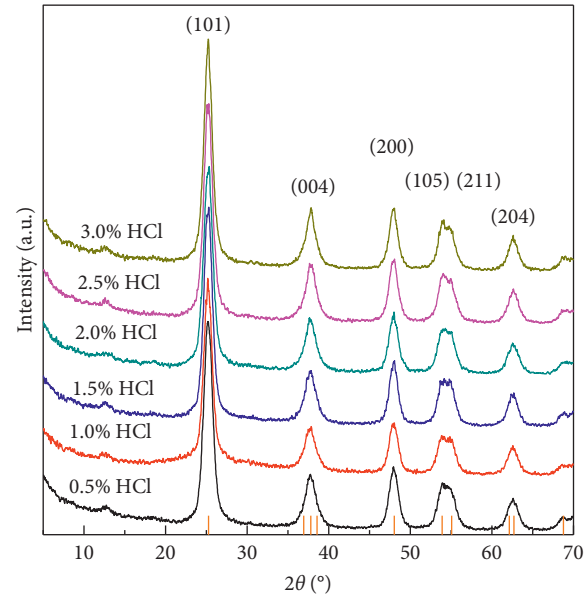

Figure 2: X-ray diffraction patterns of TiO_2^m nanoparticles prepared at 200°C in an autoclave as a function of HCl concentration.

other reflections corresponding to its other crystalline planes are observed. Relatively wide peaks corresponding to relatively small crystallite sizes (8–12 nm), as discussed below, are observed.

3.1.2. Thermal Treatment of TiO_2^m Nanoparticles in Air at 530°C. As explained in Section 2.2.3, a paste was made with TiO_2^m nanoparticles prepared using the solvothermal process for the deposition of the mesoporous layer via the screen-printing technique on the SnO_2 : F/TiO_2^c junction to obtain the SnO_2 : F/TiO_2^c/TiO_2^m heterojunction, which was thermally treated in air at 530°C for 3 h. After thermal treatment, an X-ray diffraction study was performed on each sample listed in Figure 2, with the results shown in the graph of Figure 3. This graph shows that the anatase crystalline phase is conserved for all HCl concentrations, except for 2.5 and 3.0% (v/v) HCl concentrations, where a small peak can be perceived (R) at an angle of $2\theta = 27.2°$, corresponding to the rutile crystalline phase. With thermal treatment, diffraction peaks are sharper, so the crystallite size has increased (17 to 22 nm), as reported in Table 1.

3.1.3. FE-SEM of TiO_2^m Prepared at Different HCl Concentrations. Figure 4 shows micrographs of the surface morphology of TiO_2^m taken with the FE-SEM S-5500 microscope (10,000X) for each HCl concentration used during the sol-gel/solvothermal process at 200°C. These micrographs show how the HCl concentration significantly influences the morphology of TiO_2^m particles, which changes from a relatively smooth surface, as observed in Figures 4(a) and 4(b), corresponding to the synthesis of TiO_2^m at 0.5 and 1.0% (v/v) HCl concentrations, respectively, to one in which agglomeration of TiO_2^m particles begins, as shown in Figure 4(c), corresponding to a 1.5% (v/v) HCl concentration. Figure 4(d)

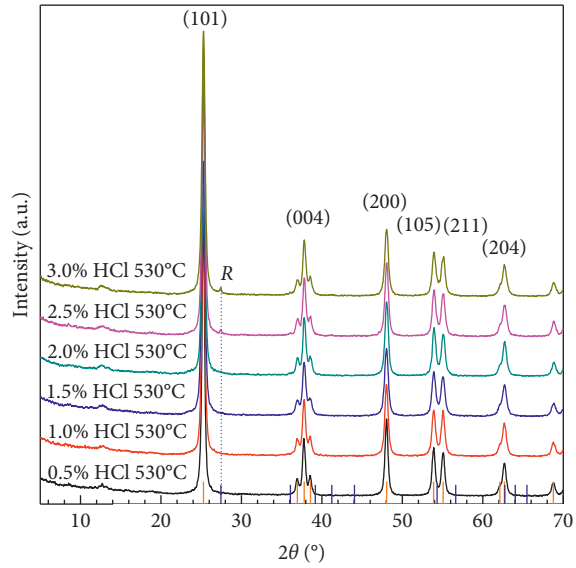

Figure 3: X-ray diffraction patterns of $TiO_2{}^m$ nanoparticles prepared at 530°C as a function of HCl concentration.

Table 1: Crystallite diameter, pore size, surface area, and band gap E_g of $TiO_2{}^m$ samples prepared in an autoclave at 200°C and at 530°C.

HCl% (v/v)	Crystallite size (nm)	Pore size (nm)	Surface area (m^2/g)	Crystallite size (nm)	Pore size (nm)	Surface area (m^2/g)	E_g (eV)
	200°C			530°C			
0.5	8.45	2.96	161.10	22.20	10.72	31.75	3.18
1.0	9.93	4.21	196.00	19.90	12.35	47.30	3.23
1.5	11.54	15.12	183.90	17.60	41.11	65.56	3.27
2.0	11.50	6.57	208.70	20.00	23.56	55.46	3.31
2.5	11.75	5.96	208.10	19.30	19.75	56.83	3.25
3.0	12.05	6.43	198.50	18.40	16.83	60.12	3.32

shows a semispherical morphology corresponding to the 2.0% (v/v) HCl concentration, where a clear coalescence is observed as larger spheres grow from the fusion with smaller spheres of $TiO_2{}^m$. As the HCl concentration increases to 2.5 and 3.0% (v/v), more perfect and larger $TiO_2{}^m$ spheres with diameters above 6 microns are obtained (Figure 4(e)), and Figure 4(f) shows even larger $TiO_2{}^m$ spheres with irregular agglomerates beginning to grow on their surfaces. Notably, Kim et al. [42] also reported the synthesis of $TiO_2{}^m$ spheres in acid media (a mixture of H_2SO_4 and HNO_3) using surfactants as nucleation precursors during the sol-gel process and a subsequent hydrothermal treatment to obtain highly spherical morphologies such as those shown in this study.

Figures 5 and 6 show images of the $TiO_2{}^m$ samples included in Figure 4 at a 300,000X and 500,000X magnification, respectively, where each sample, including the spheres, are made of $TiO_2{}^m$ nanocrystals. Figures 5 and 6 show that all samples have pores and that the pore diameter grows from 10 to 23 nm when the HCl concentration increases from 0.5 to 3.0% (v/v).

The magnification increase from 300,000X to 500,000X allowed us to observe in a much better form the surface morphology as well as the pore size distribution of $TiO_2{}^m$ synthesized at different HCl concentrations. For example, from Figures 4(a)–4(d), it is easy to see a pore size increase as the HCl concentration varies from 0.5 to 2.0% (v/v), and after that, the pore size remains almost constant. Also, the crystal size can be much better estimated, as shown in Figure 6, and its value coincides with the determined by X-ray diffraction (8–12 nm), as explained in Section 3.1.1.

3.1.4. Surface Area, Crystallite Size, Pore Size, and E_g of $TiO_2{}^m$ as a Function of HCl Concentration. The crystallite size, surface area, and pore size play a fundamental role in the performance of DSSC. For example, the smaller the crystallite size is, the larger the surface area will be, which allows us to have many *p-n* junctions between the dye and $TiO_2{}^m$. Table 1 shows the average crystallite diameter, pore size, and surface area of $TiO_2{}^m$ samples in powder form after their synthesis in the autoclave at 200°C for each HCl concentration used. To use it in the development of DSSC, $TiO_2{}^m$ must be subjected to thermal treatment in air at 530°C. Table 1 also shows the values of the average crystallite diameter, pore size, surface area, and band gap of $TiO_2{}^m$ powders treated at 530°C for 3 h.

Considering only the pore size obtained for the titanium dioxide samples treated at 200 and 530°C, it is possible to conclude from Table 1 that the material is mesoporous, according to the IUPAC definition [43] because, for all cases, the pore size of $TiO_2{}^m$ remains below 50 nm.

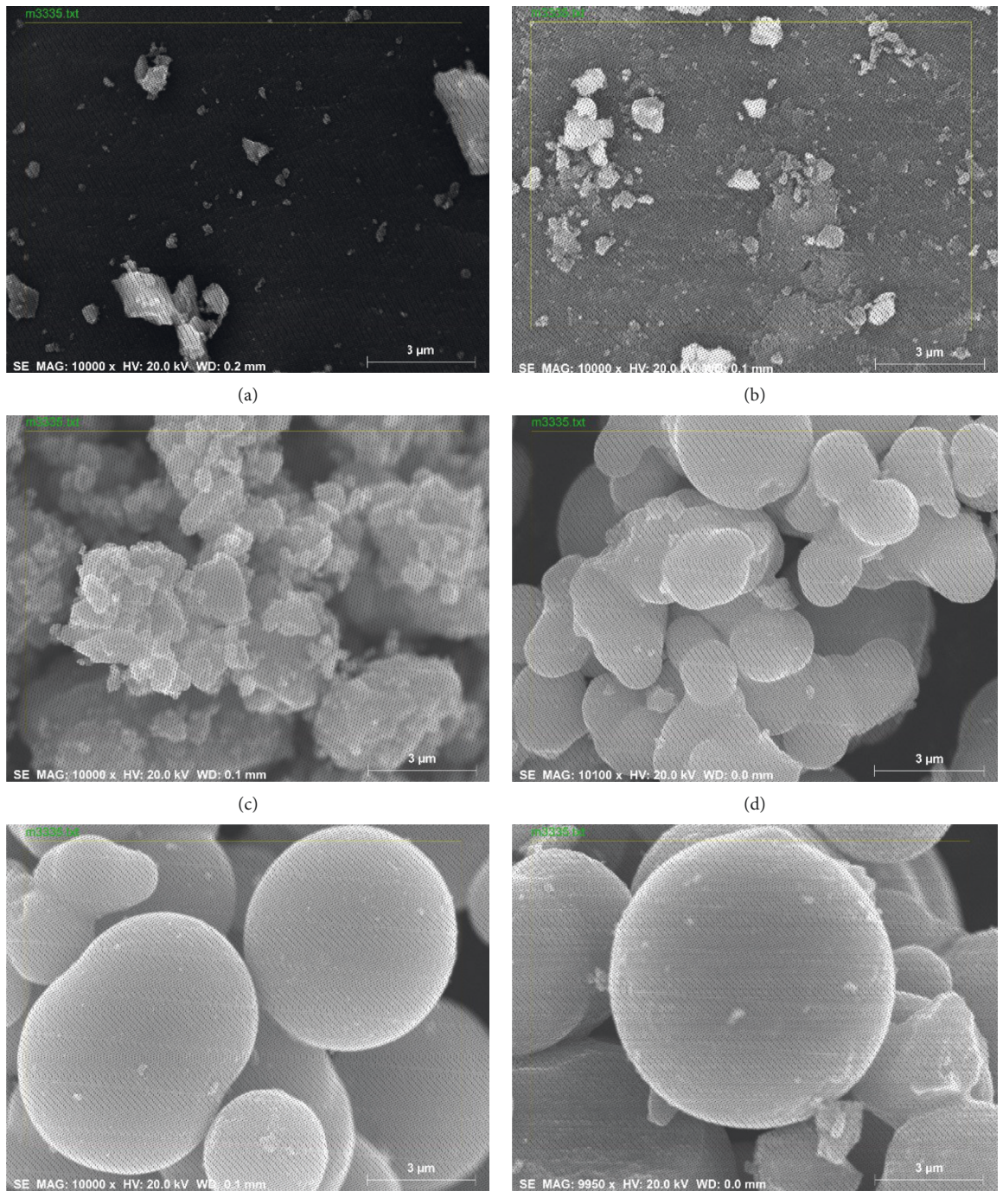

Figure 4: Micrographs of $TiO_2{}^m$ (10,000X magnification) synthesized at different HCl concentrations: (a) 0.5, (b) 1.0, (c) 1.5, (d) 2.0, (e) 2.5%, and (f) 3.0% (v/v).

Considering the results of Table 1, columns 4 and 7 show the surface area of $TiO_2{}^m$ as a function of HCl concentration for samples treated at 200°C (solvothermal process) and at 530°C, respectively. The surface area decreases drastically from an average of 198 to 52 m^2/g as the temperature changes from 200 to 500°C. This decrease in surface area is due to crystallite size growth (diameter), as observed from columns 2 and 5, and to particle coalescence into spherical configurations to form larger $TiO_2{}^m$ spheres, favoring the increase in pore size observed in columns 2 and 6 of Table 2.

Columns 3 and 6 show a maximum pore size of 15.12 nm at 200°C and 41.11 nm at 530°C, both at 1.5% (v/v) HCl concentration. The pore size decreases above the 1.5% (v/v) HCl concentration. This decrease can be attributed to a competition between the decrease in crystallite size from 20.0 to 18.4 nm shown in Table 1 and the formation of larger $TiO_2{}^m$ spheres as the HCl concentration increases above 1.5% (v/v).

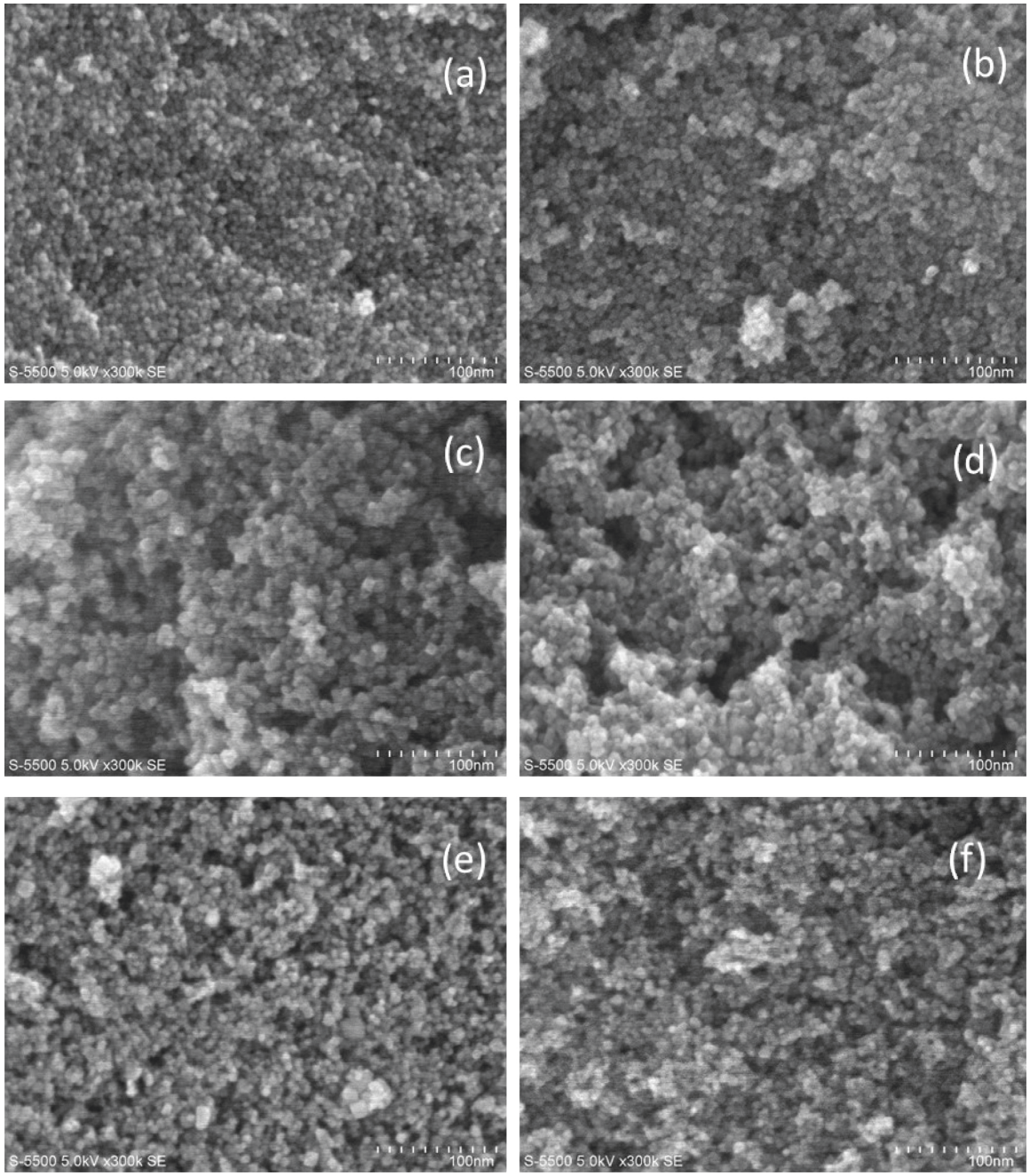

Figure 5: Micrographs (300,000X magnification) of $TiO_2{}^m$ synthesized at different HCl concentrations: (a) 0.5, (b) 1.0, (c) 1.5, (d) 2.0, (e) 2.5, and (f) 3.0% v/v.

3.2. Influence of H_2O during Hydrolysis on the Synthesis of $TiO_2{}^m$ Nanoparticles

3.2.1. $TiO_2{}^m$ Samples Obtained at Different H_2O Concentrations. Once the effect of HCl concentration on preparing $TiO_2{}^m$ via the solvothermal process was studied, the role of the H_2O content during the synthesis of $TiO_2{}^m$ was analyzed. To this end, X-ray diffraction studies were performed on the $TiO_2{}^m$ films prepared via the solvothermal process at 200°C, taking the 2.5% (v/v) HCl concentration as a fixed experimental parameter and varying the H_2O concentration from 1.9 to 4.9% (v/v). All cases show an X-ray diffraction pattern of the $TiO_2{}^m$ anatase crystalline phase very similar to that in Figure 2. It was also observed that for the 3.9% (v/v) H_2O concentration, there are small indications of the growth of a brookite phase at an angle of $2\theta = 30.8^\circ$ corresponding to the (121) plane.

3.2.2. $TiO_2{}^m$ Samples Treated at 530°C. Because the $TiO_2{}^m$ layer in the development of DSSC was thermally treated in air at 530°C for 3 h, after calcining at that temperature, these samples were subjected to an X-ray diffraction study.

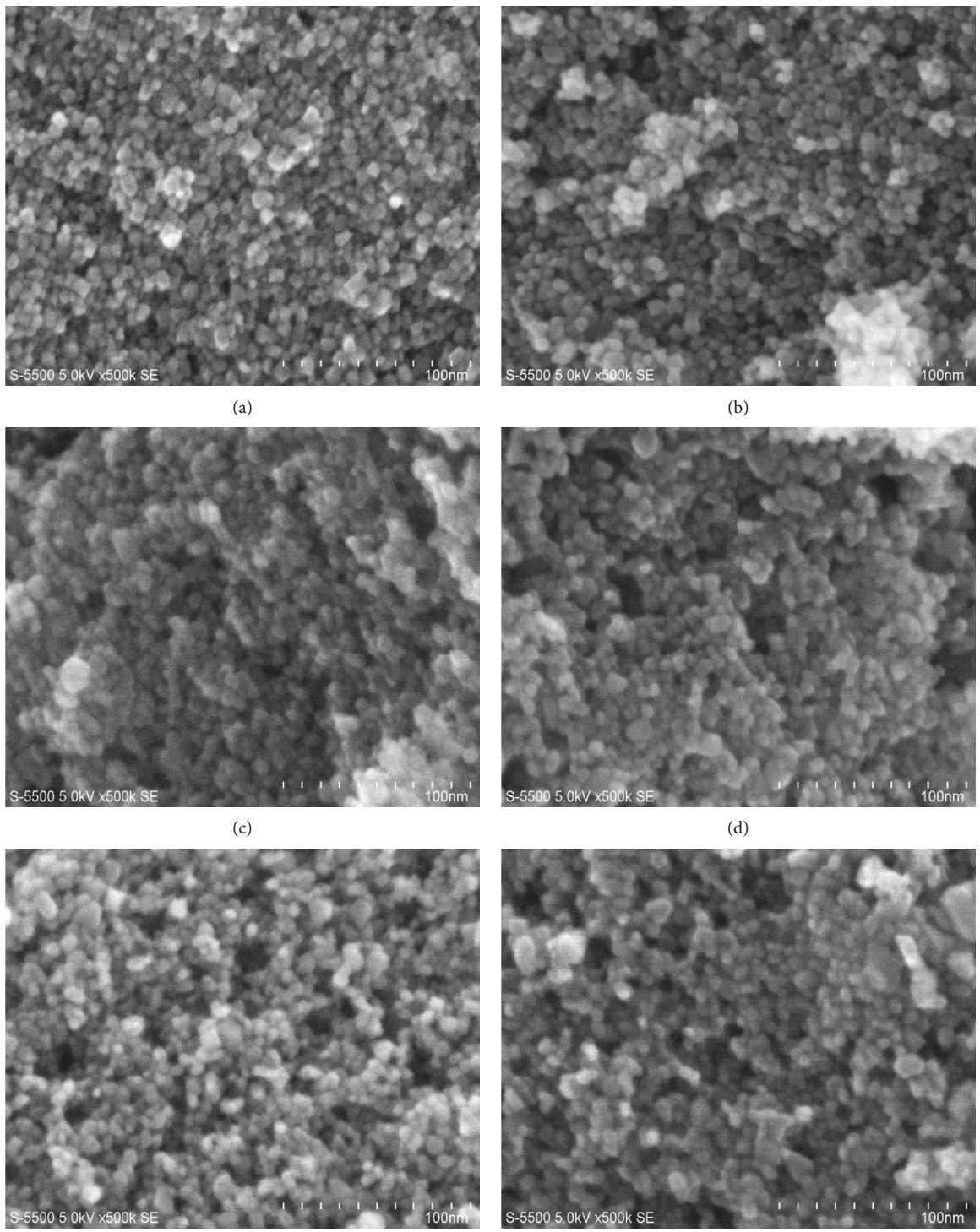

Figure 6: Micrographs (500,000X magnification) of $TiO_2{}^m$ synthesized at different HCl concentrations: (a) 0.5, (b) 1.0, (c) 1.5, (d) 2.0, (e) 2.5, and (f) 3.0% v/v.

The diffraction pattern found in these samples is very similar to that shown in Figure 3 for samples prepared at different HCl concentrations. Here, the anatase crystalline phase is conserved for all H_2O concentrations except for 2.5 and 3.0% (v/v), where a small peak can be perceived at $2\theta = 27.5^{\circ}$C, corresponding to the rutile crystalline phase (R). On the contrary, it is also possible to observe that after said thermal treatment at 530°C, the brookite phase disappears for all H_2O concentrations at which it could be observed.

Table 2: Crystallite diameter, surface area, pore size, and forbidden energy band gap E_g of $TiO_2{}^m$ samples thermally treated in air at 530°C as a function of the H_2O concentration.

H_2O% (v/v) (530°C)	Crystallite size (nm)	Surface area (m^2/g)	Pore size (nm)	E_g (eV)
1.9	19.30	56.83	19.75	3.18
2.4	18.40	56.29	17.19	3.23
2.9	18.10	62.52	33.14	3.27
3.4	16.60	68.15	30.89	3.31
3.9	16.90	71.40	22.93	3.25
4.9	17.10	66.84	22.17	3.32

3.2.3. Analysis of the $TiO_2{}^m$ Surface Area and Pore Size as a Function of H_2O Concentration. For use in the development of DSSC, $TiO_2{}^m$ powders should be thermally treated at 530°C in air for 3 h. Table 2 shows the average crystallite diameter, surface area, and pore size of $TiO_2{}^m$ samples prepared at different H_2O concentrations, maintaining the HCl concentration at 2.6% (v/v) and thermally treated in air at 530°C.

Comparing the columns pertaining to crystallite size in Tables 1 and 2, one finds that for treatment at 530°C, on average (not shown in tables), the $TiO_2{}^m$ crystallite size decreases more with increasing H_2O concentration (17.3 nm) than with increasing HCl concentration (19.56 nm), and consequently, the surface area and forbidden band of $TiO_2{}^m$ should grow slightly with increasing H_2O concentration. Similarly, by comparing the corresponding columns for the pore size shown in Tables 1 and 2, one finds that for treatment at 530°C, on average, a larger $TiO_2{}^m$ pore size is more favored by increasing the concentration of H_2O (24.34 nm) than by increasing that of HCl (20.72 nm).

The findings described in the previous paragraph should be revealed by an increase in the surface area upon optimizing the H_2O concentration. Indeed, by comparing the columns pertaining to the surface area in Tables 1 and 2, one finds that for treatment at 530°C, on average, a larger $TiO_2{}^m$ surface area is more favored by an increase in H_2O concentration (63.97 m^2/g) than by an increase in HCl concentration (52.83 m^2/g). An increasing surface area increases the number of contact points between $TiO_2{}^m$ and the dye, and this is reflected in the solar cell performance as seen later.

3.3. $TiO_2{}^m$ Crystallite Size as a Function of HCl and H_2O Concentrations. Curve (a) in Figure 7 shows the crystallite size of $TiO_2{}^m$ in samples prepared in the autoclave at a temperature of 200°C as a function of HCl concentration, maintaining a fixed 1.9% (v/v) H_2O concentration. As shown in Table 1, the crystallite size increases from 8.45 to 11.04 nm as the HCl concentration increases from 0.5 to 1.5% (v/v); above this last value, the crystallite grows more slowly and reaches a constant value close to 12 nm. This behavior could be due to the hydrolysis of titanium isopropoxide, in which the substitution of the isopropoxy groups $O(C_3H_7)^-$ of titanium isopropoxide by OH^- groups is relatively slow, and as HCl is added, hydrolysis speeds up, causing an increase in crystallite size up to a concentration of 1.5% (v/v), at which the chemical bonds between Ti^{4+} and OH^- hydroxyl radicals reach saturation. Above the 1.5% (v/v) HCl concentration, the crystallite growth is very slow and almost constant. Curve (b) in Figure 7 shows the crystallite sizes of $TiO_2{}^m$ prepared in the autoclave at 200°C by varying the H_2O concentration and taking as a fixed parameter a 2.5% (v/v) HCl concentration. From that curve, it is possible to observe that the crystallite size of the TiO_{2m} semiconductor undergoes a slight decay from 11.8 to 10.6 nm as the H_2O concentration increases from 1.9 to 4.9% (v/v).

3.4. Forbidden Energy Band Gap of $TiO_2{}^m$ as a Function of HCl and H_2O Concentrations. According to the theory of quantum confinement, when the size (diameter) of a crystallite in a crystalline solid decreases to a few nanometers (2–20 nm), the magnitude of the forbidden energy band gap varies. To calculate the forbidden energy band gap E_g, $TiO_2{}^m$ nanoparticles were synthesized at different HCl and H_2O concentrations and thermally treated in air at 530°C. Because $TiO_2{}^m$ has an indirect energy band, a graph of $(\alpha \cdot h\nu)^{1/2}$ vs. $h\nu$ was drawn. In this mathematical expression, α is the absorption coefficient of $TiO_2{}^m$ and is calculated using equation (2), where d is the film thickness, T is the transmittance, and R is the optical reflectance of the material [44]. The tangent line to the curve intersecting the $h\nu$ axis indicates a very approximate value of the forbidden energy band gap:

$$\alpha = \frac{1}{d} * \ln\left(\frac{100 - R}{T}\right). \quad (2)$$

Following the procedure described above, the value of the indirect energy band gap E_g was determined for each HCl concentration used during the synthesis of $TiO_2{}^m$, maintaining a 1.9% (v/v) H_2O concentration as a fixed parameter.

Curve (a) in Figure 8 shows the values of the indirect energy band gap E_g determined for each HCl concentration used for the synthesis of $TiO_2{}^m$. As the HCl concentration increases from 0.5 to 2% (v/v) in the synthesis of the particles, E_g decreases from 3.375 to 3.18 eV; above this concentration, E_g increases slightly until reaching 3.26 eV. These results suggest that optical properties, particularly the absorption coefficient of $TiO_2{}^m$, depend on the synthesis of the material [45].

Curve (b) in Figure 8 shows the magnitude of the indirect forbidden energy band gap E_g of $TiO_2{}^m$ treated at 530°C (HCl concentration = 2.5% (v/v)). This figure shows that the forbidden energy band gap increases from 3.18 to 3.32 eV when the H_2O content varies from 1.9 to 4.9% (v/v). The growth in the magnitude of the forbidden energy band gap is consistent with the decrease in crystallite size from 19.3 to 17.1 nm shown in Table 2, which can be attributed to a quantum confinement effect, as explained by Sánchez et al. [46].

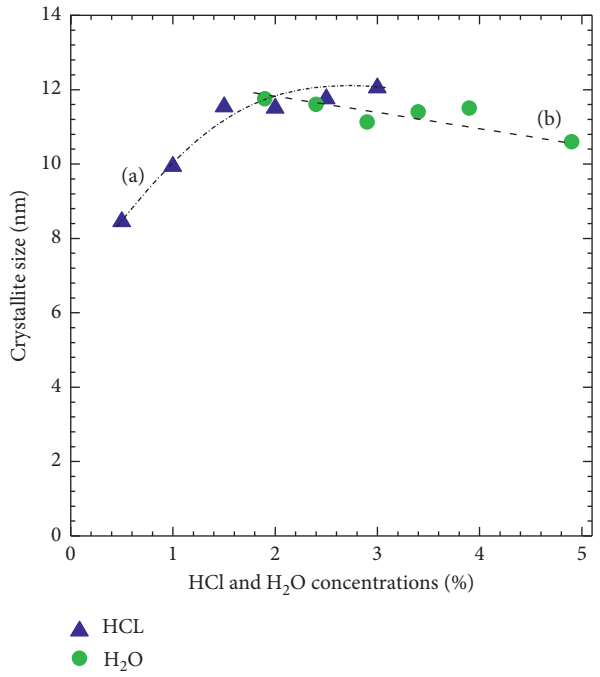

Figure 7: Crystallite size as a function of (a) HCl and (b) H_2O concentrations.

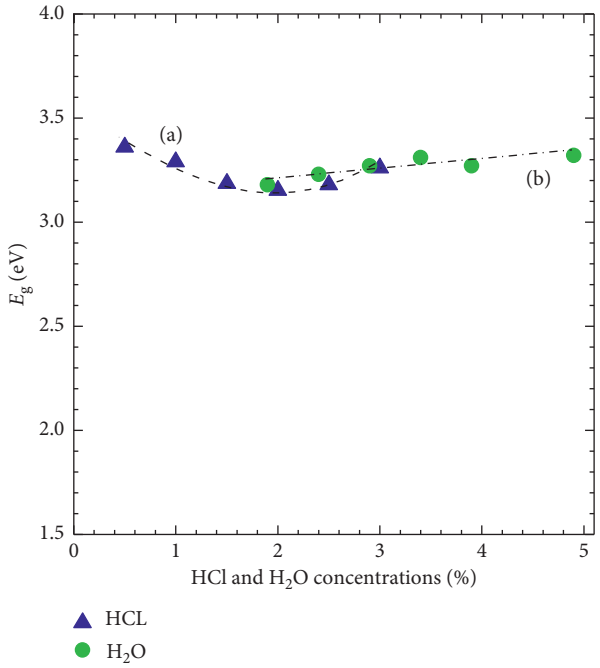

Figure 8: Band gap behavior of TiO_2^m as a function of the (a) HCl and (b) H_2O concentrations after thermal treatment in air at 530°C.

3.5. Photovoltaic Performance Analysis of DSSC

3.5.1. Effect of HCl on the Photovoltaic Performance of DSSC. Once the TiO_2^m semiconductor was prepared, the DSSC was assembled with a structure of the type SnO_2: $F/TiO_2^c/TiO_2^m/N719/I^-/I_3^-/Pt/SnO_2$: F. Here, the TiO_2^m layers were thermally treated in air at 530°C, having a thickness close to 12 microns.

Figure 9 shows the current-voltage curves (I-V) for the different HCl concentrations used in the synthesis of the *n*-type TiO_2^m semiconductor via the solvothermal process. As shown, the HCl concentration drastically influences the performance of the DSSC, where the parameter most influenced is the short-circuit current density J_{SC} and thus the conversion efficiency η% of the solar cell.

The short-circuit current density J_{SC} starts at 4.2 mA/cm^2 for the 0.5% (v/v) HCl concentration and reaches a value of 10.14 mA/cm^2 for the 2.0% (v/v) HCl concentration; above this concentration, J_{SC} decreases to 8.83 mA/cm^2 for the 3.0% (v/v) HCl concentration.

Table 3 summarizes the performance parameters of the DSSC shown in Figures 9 and 10, that is, the open-circuit voltage (V_{OC}), the short-circuit current density (J_{SC}), the fill factor (FF), and the energy conversion efficiency (η%) of the DSSC obtained by varying the concentration of HCl as a catalyst for the hydrolysis of titanium isopropoxide as well as the H_2O content during the sol-gel/solvothermal process.

With the data presented at the left side of Table 3, Figure 10(a) shows a graph of the short-circuit current J_{SC} as a function of the concentration of HCl for the hydrolysis, showing a maximum at J_{SC} = 10.14 mA/cm^2 and 2.0% (v/v) HCl.

The conversion efficiency η% shows a behavior analogous to that of J_{SC}. As shown in Figure 10(b), as the concentration of the HCl hydrolysis catalyst is increased from 0.5 to 2.5% (v/v), η% increases from 2.06% to 3.91%. Above this HCl concentration (2.5% (v/v)), η% decreases to 3.69%.

Table 3 (left side) shows a small variation in the open-circuit voltage V_{OC} upon increasing the concentration of HCl for the hydrolysis from 0.5 to 2.5% (v/v). In this case, the open-circuit voltage V_{OC} decreases slightly from 0.73 to 0.68 V and then increases again to 0.7 V at the 3.0% (v/v) HCl concentration, yielding an average value of V_{OC} = 0.695. Likewise, the fill factor (FF) decreases from 0.68 to 0.52 as the HCl concentration increases from 0.5 to 2.0% (v/v) and then increases again slightly to 0.59 at the 3.0% (v/v) HCl concentration, for an average value of FF = 0.616.

3.5.2. Effect of the H_2O Content on the Photovoltaic Performance of DSSC. Figure 11 shows the I-V curves of DSSC utilizing the TiO_2^m semiconductor prepared with a 2.5% (v/v) HCl concentration for the hydrolysis of titanium isopropoxide and varying H_2O content during the sol-gel/solvothermal process. According to Figure 10(b), 2.5% (v/v) HCl concentration optimizes the efficiency of the DSSCs prepared using the TiO_2^m semiconductor. Table 3 (right side) shows the performance parameters of the DSSC shown in Figure 11: V_{OC}, J_{SC}, FF, and η% of the DSSC obtained by varying the H_2O content.

The right side of Table 3 shows that DSSC prepared from TiO_2^m synthesized at different H_2O contents have more uniform and less disperse values of the open-circuit voltage V_{OC} and fill factor (FF) than the corresponding values found at the left side of Table 3 for TiO_2^m synthesized at different

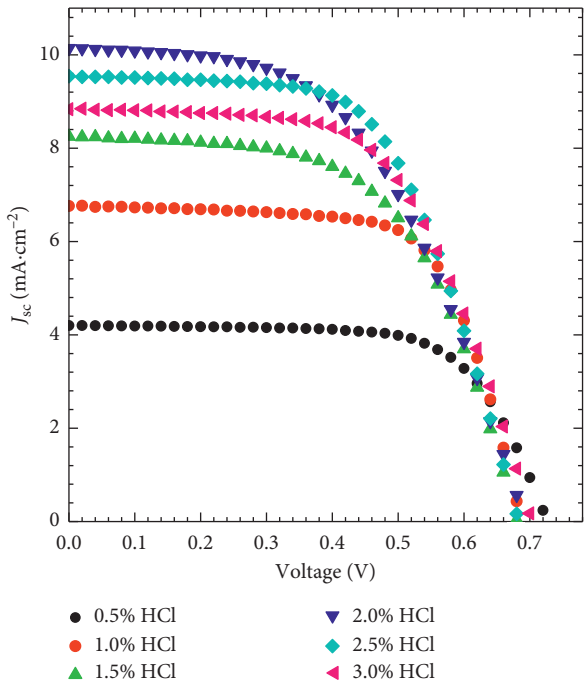

Figure 9: I-V curves of DSSC with *n*-type semiconductors prepared at different concentrations of HCl as a catalyst for the hydrolysis.

Table 3: Performance parameters of solar cells. Left side: DSSCs utilizing TiO_2^m synthesized via a sol-gel/solvothermal process at different HCl concentrations and at a 1.9% (v/v) H_2O concentration and thermally treated in air at 530°C. Right side: DSSCs prepared from TiO_2^m synthesized at different H_2O contents and at a 2.5% (v/v) HCl concentration for the hydrolysis and thermally treated in air at 530°C.

HCl% (v/v)	V_{OC} (V)	J_{SC} (mA·cm^{-2})	FF	η (%)	H_2O% (v/v)	V_{OC} (V)	J_{SC} (mA·cm^{-2})	FF	η (%)
0.5	0.73	4.20	0.68	2.06	1.9	0.68	9.54	0.60	3.91
1.0	0.69	6.76	0.68	3.15	2.4	0.69	9.38	0.63	4.07
1.5	0.68	8.61	0.63	3.65	2.9	0.70	7.27	0.64	3.26
2.0	0.69	10.14	0.52	3.66	3.4	0.69	8.44	0.64	3.69
2.5	0.68	9.54	0.60	3.91	3.9	0.68	9.45	0.63	4.08
3.0	0.70	8.83	0.59	3.69	4.9	0.67	9.16	0.65	3.99

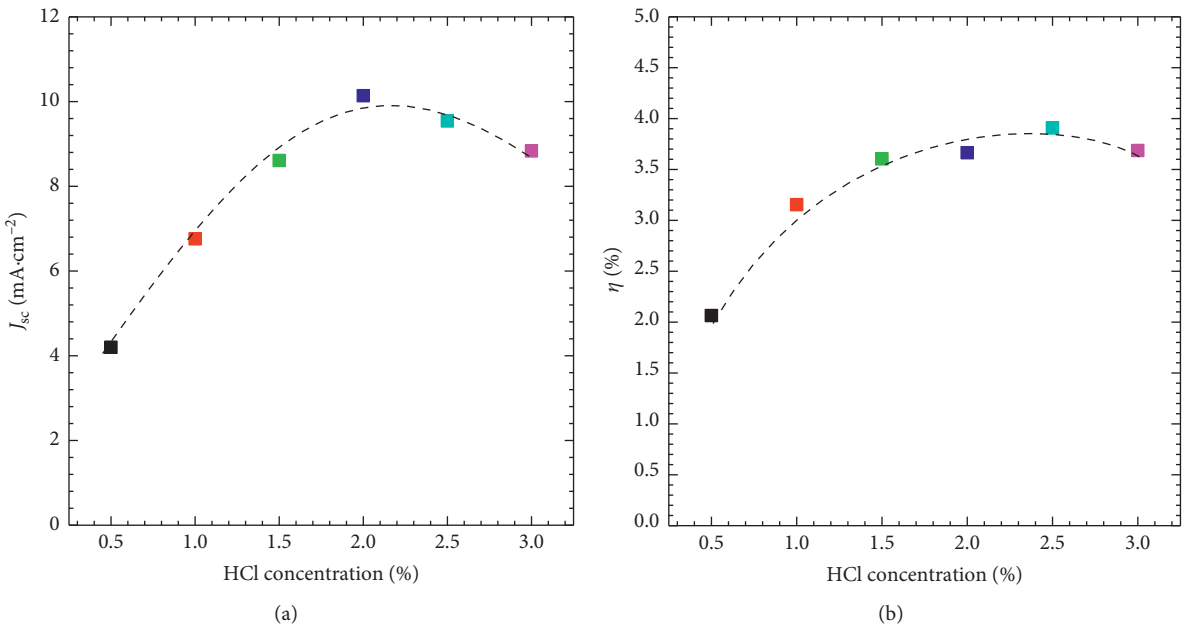

Figure 10: (a) Behavior of the short-circuit current J_{SC} and (b) conversion efficiency as a function of the concentration of HCl for the hydrolysis.

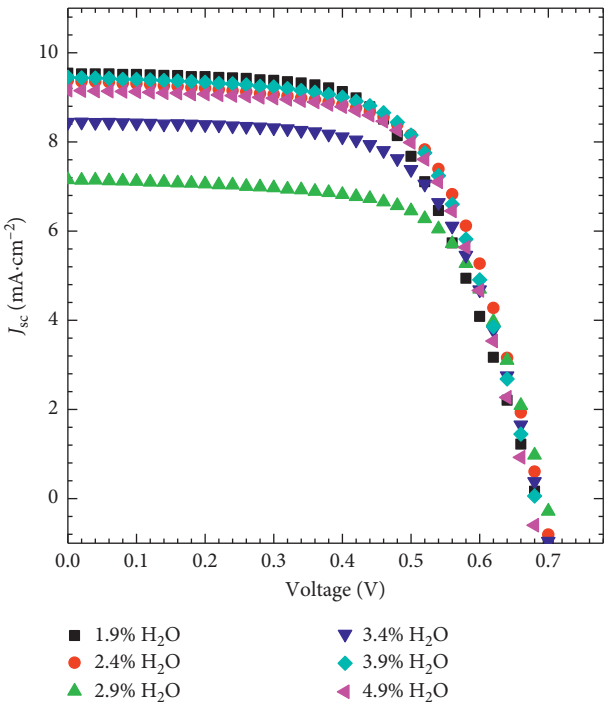

Figure 11: I-V curve of DSSC with *n*-type semiconductors prepared at different H_2O concentrations and at a 2.5% HCl concentration for the hydrolysis.

HCl concentrations. The open-circuit voltage V_{OC} remains almost constant around its average value of 0.685 V when there is a variation in H_2O content, in contrast to an average value of $V_{OC} = 0.695$ V when there is a variation in HCl concentration. Likewise, the fill factor (FF) remains almost constant around its average value of 0.631 when there is a variation in H_2O content, in contrast to an average value of FF = 0.616 when there is a variation in HCl concentration.

By comparing the average values of the short-circuit currents J_{SC} of the DSSCs in Figures 9 and 11, one finds that the average J_{SC} (H_2O; $J_{SC} = 8.873$ mA/cm^2) of the DSSC in Figure 11 surpasses that in Figure 9 (HCl; $J_{SC} = 8.13$ mA/cm^2), so the average conversion efficiency of the solar cells in Figure 11 ($\eta\% = 3.83\%$) exceeds the average conversion efficiency of the corresponding ones in Figure 9 ($\eta\% = 3.35\%$).

3.6. On the Method of Preparing Mesoporous Spheres and the Conversion Efficiency Achieved. There is a substantial difference between the preparation methods for mesoporous spheres described in the introduction and the one developed in this study. In the previous methods [31–35], the mesoporous spheres are formed in the first step of the sol-gel solution, then extracted, dried, and passed to the solvothermal process in an autoclave. In the present method, $TiO_2{}^m$ microspheres are formed within the autoclave under the influence of a coalescence process at 200°C and HCl, which, with increasing concentration, produces larger mesoporous spheres, as observed in the FE-SEM studies shown in Figure 4.

For comparison purposes of the results obtained in this work, in the literature, it is possible to find other research works related to the synthesis of TiO_2 microspheres with an anatase crystalline phase and its application in dye-sensitized solar cells.

Zhao-Qian and coworkers developed a modified solvothermal process to carry out the synthesis of TiO_2 microspheres using acetone as solvent [35]. As-prepared TiO_2 spheres with diameters from 550 to 1010 nm are composed of densely interconnected nanocrystals with each other and possess a high specific surface area up to 138.47 m$^2\cdot$g^{-1}. As *n*-type semiconductor integrated in DSSC, Zhao-Qian and coworkers prepared TiO_2 microsphere films via screen printing. With the work electrode (dye-sensitized TiO_2 microspheres), DSSC provided a power conversion efficiency of 7.80%. Finally, TiO_2 microsphere-based DSSCs were optimized by adding a TiO_2 nanocrystal underlayer and $TiCl_4$ post-treatment providing a better performance.

In addition, Swathy et al. prepared anatase titania microspheres by a modified sol-gel method [47]. At first, they took a defined amount of titanium (IV) butoxide (TB) and ethylene glycol, which were mixed and stirred constantly for 24 hours. Subsequently, to the previous solution, they added a water-acetone mixture. The final precipitate was washed, filtered, and dried. The powder obtained, which was further heat treated at 500°C, contained spherical titania particles with a diameter of ~400 nm. The titania microspheres were then used as the scattering layer in DSSC. To assemble DSSCs, Swathy et al. deposited the scattering layer by screen printing on a nanocrystalline titania coating. DSSC with scattering layer achieved photovoltaic parameters, such as V_{oc} of 0.690 V, J_{sc} of 10.44 mA/cm^2, fill factor of 0.68, and a conversion efficiency of 4.92%.

Another work on the preparation of anatase TiO_2 spheres is that reported by Ch. Dwivedia at al. where TiO_2 hollow spheres were synthetized in a continuous spray pyrolysis reactor, using titanium isopropoxide as organic precursor and ethanol as solvent [48]. TiO_2 powder was collected from the outlet of the furnace. This powder was then utilized to make TiO_2 paste using ethanol as solvent. The size of TiO_2 hollow spheres was about 170–300 nm, and the thickness of the shell was about 55–60 nm. TiO_2 hollow spheres were utilized as a scattering layer in dye-sensitized solar cells (DSSCs). Commercial nanocrystalline TiO_2 paste (20 nm) forming the transparent layer was from Dyesol. DSSC containing TiO_2 hollow spheres layer showed a power conversion efficiency of 7.46% which is better than that containing single layer TiO_2 transparent film (7.1%).

Finally, Miao et al. also prepared mesoporous anatase TiO_2 microspheres with different surface areas obtained by a solvothermal process [49]. To do so, tetrabutyl titanate (TBT) was slowly added to an acetone-phenol mixed solvent under vigorous stirring at room temperature. The resulting solution was transferred into a 40 mL Teflon-lined stainless steel autoclave, and then heated at 150°C for 24 h. The samples were then sintered at 500°C. By tuning the ratio of the mixed solvent, the authors obtained high-quality TiO_2 microspheres with controllable surface areas of 122–168 m$^2\cdot$g^{-1}. Then, the mesoporous anatase TiO_2 microspheres were used as the

scattering layer of the photoelectrode. DSSC based on a photoelectrode with a TiO_2 nanoparticle underlayer and a microsphere scattering layer yield the highest photoelectrical conversion efficiency of 7.94%.

In summary, we have seen that TiO_2 microspheres can be synthetized by several preparation methods utilizing different titanium precursors and solvents. TiO_2 microspheres synthetized here (Table 1) or reported in the literature have a large surface area, are mesoporous, and can be used for light scattering in DSSC, allowing for a good charge collection efficiency.

On the contrary, to explain the reason for the relatively low conversion efficiency (4.07%) obtained in the DSSC prepared here, it should be understood that the use of mesoporous spheres in the $TiO_2{}^m$ semiconductor layer has certain disadvantages compared to a compact and homogeneous mesoporous layer (nanoparticle underlayer or nanocrystalline titania coating) of $TiO_2{}^m$: (a) There are gaps between spheres that do not contribute to the formation of the $TiO_2{}^m$/dye junctions. (b) The spherical morphology reduces the surface area, lessening contact between $TiO_2{}^m$ and the dye. (c) The spherical morphology reduces the number of electronic paths for electric current transport after dye excitation. All these facts are detrimental to the conversion efficiency of the DSSC developed here.

To increase the conversion efficiency of the DSSC developed in this study, it would be very convenient to work with the following alternatives in the near future:

(a) Mix $TiO_2{}^m$ spheres with $TiO_2{}^p$ in powder form (called nanoparticle underlayer or nanocrystalline titania coating) without a spherical morphology to fill the gaps between $TiO_2{}^m$ spheres and thus build DSSC.

(b) Use a mesoporous $TiO_2{}^p$ layer in powder form (without a spherical morphology), depositing the mesoporous spheres on that layer, that is, build the solar cell heterostructure with the configuration $SnO_2:F/TiO_2{}^c/TiO_2{}^p/TiO_2{}^m/N719/I^-/I_3{}^-/Pt/SnO_2:F$. In the said heterostructure, the $TiO_2{}^m$ layer would function as a scattering layer, as already reported in the literature, which would result in a structure with greater conversion efficiency [50].

4. Conclusions

The structure and morphology of the $TiO_2{}^m$ nanoparticles prepared via a sol-gel/solvothermal method are greatly influenced by the HCl and H_2O concentrations used during hydrolysis of the titanium isopropoxide precursor. HCl greatly changes the morphology of $TiO_2{}^m$ and, as a function of concentration, contributes to obtaining either a planar configuration or a spherical morphology, that is, mesoporous microspheres. On the contrary, optimizing the H_2O concentration enabled a decrease in the crystallite size of $TiO_2{}^m$ and consequently increases in the surface area, pore size, and energy band gap of $TiO_2{}^m$. The increase in surface area allowed the number of contact points between $TiO_2{}^m$ and the dye to increase, which was positively reflected in the solar cell performance. However, in all the synthesis processes performed in this study, it was possible to obtain $TiO_2{}^m$ in a predominantly anatase crystalline phase.

The HCl and H_2O concentrations during the synthesis of the n-type $TiO_2{}^m$ semiconductor also have an important influence on the behavior of the performance parameters of the DSSC (I_{SC}, V_{OC}, FF, and η%). By varying the concentration of the catalyst (HCl) during hydrolysis of the precursor, a greater variation in the short-circuit current J_{SC} is observed in the *I-V* curve of the DSSC, with a greater dispersion of the values of the performance parameters of the solar cells (I_{SC}, V_{OC}, FF, and η%).

On the contrary, by optimizing the H_2O concentration during the synthesis of the *n*-type $TiO_2{}^m$ semiconductor, in the analyzed DSSC, the values of the open-circuit voltage V_{OC} and fill factor (FF) are more uniform and less disperse than those for $TiO_2{}^m$ synthesized at different HCl concentrations. On average, the short-circuit currents J_{SC} and conversion efficiency η% of the cells whose synthesis of $TiO_2{}^m$ was optimized by adjusting the H_2O content surpass those optimized by adjusting only the HCl concentration. The highest conversion efficiency (η%) found in the DSSC reported in this study was 4.08%.

In summary, the performance parameters (I_{SC}, V_{OC}, FF, and η%) of DSSC were greatly influenced by the HCl and H_2O concentrations used during hydrolysis of the titanium isopropoxide precursor in the synthesis of the *n*-type $TiO_2{}^m$ semiconductor.

Data Availability

This research article is the result of the Ph.D. dissertation in Engineering and Applied Sciences of the student Sergio Velazquez Martínez carried out in the Research Institute of Basic and Applied Sciences of the Autonomous University of the State of Morelos, Mexico. The data of said results are available in the student's work log which is available in the aforementioned institute.

Conflicts of Interest

The authors declare that they have no conflicts of interest.

Acknowledgments

This study was performed with financial support from the Energy Sustainability Fund SENER-CONACYT-Mexico through project B-S-69369 (Bilateral project Mexico-England) and from DGAPA-PAPIIT through project IT101118. The authors thank M. Sc. Ma. Luisa Ramón García for her support in measuring and analyzing the X-ray diffraction patterns of the TiO_2 blocking and mesoporous films, Eng. Rogelio Moran Elvira for his support in the scanning electron microscopy measurements and Engs. A. Palafox and E. Luna for their technical assistance in the development of the transparent conductor of SnO_2: F.

References

[1] B. O'Regan and M. Grätzel, "A low-cost, high-efficiency solar cell based on dye-sensitized colloidal TiO_2 films," *Nature*, vol. 353, pp. 737–740, 1991.

[2] M. Pazoki, U. B. Cappel, E. M. J. Johansson, A. Hagfeldt, and G. Boschloo, "Characterization techniques for dye-sensitized solar cells," *Energy & Environmental Science*, vol. 10, no. 3, pp. 672–709, 2017.

[3] M. Ye, X. Wen, M. Wang et al., "Recent advances in dye-sensitized solar cells: from photoanodes, sensitizers and electrolytes to counter electrodes," *Materials Today*, vol. 18, no. 3, pp. 155–162, 2015.

[4] M. Grätzel, "The advent of mesoscopic injection solar cells," *Progress in Photovoltaics: Research and Applications*, vol. 14, no. 5, pp. 429–442, 2006.

[5] M. Grätzel, "Dye-sensitized solar cells," *Journal of Photochemistry and Photobiology C: Photochemistry Reviews*, vol. 4, no. 2, pp. 145–153, 2003.

[6] R. Govindaraj, N. Santhosh, M. Senthil Pandian, and P. Ramasamy, "Preparation of titanium dioxide nanorods/nanoparticles via one-step hydrothermal method and their influence as a photoanode material in nanocrystalline dye-sensitized solar cell," *Applied Surface Science*, vol. 449, pp. 166–173, 2018.

[7] M. Jalali, R. Siavash Moakhar, A. Kushwaha, G. K. L. Goh, N. Riahi-Noori, and S. K. Sadrnezhaad, "Enhanced dye loading-light harvesting TiO_2 photoanode with screen printed nanorod-nanoparticles assembly for highly efficient solar cell," *Electrochimica Acta*, vol. 169, pp. 395–401, 2015.

[8] V. Karthikeyan, S. Maniarasu, V. Manjunath, E. Ramasamy, and G. Veerappan, "Hydrothermally tailored anatase TiO_2 nanoplates with exposed {1 1 1} facets for highly efficient dye-sensitized solar cells," *Solar Energy*, vol. 147, pp. 202–208, 2017.

[9] Y. Cui, X. He, M. Zhu, and X. Li, "Preparation of anatase TiO_2 microspheres with high exposure (001) facets as the light-scattering layer for improving performance of dye-sensitized solar cells," *Journal of Alloys and Compounds*, vol. 694, pp. 568–573, 2017.

[10] S. Kathirvel, C. Su, Y.-J. Shiao, Y.-F. Lin, B.-R. Chen, and W.-R. Li, "Solvothermal synthesis of TiO_2 nanorods to enhance photovoltaic performance of dye-sensitized solar cells," *Solar Energy*, vol. 132, pp. 310–320, 2016.

[11] M. Gao, Y. Ma, L. Qi, J. Liang, Y. Si, and Q. Zhang, "Anatase TiO_2 nanocrystals via dihydroxy bis (ammonium lactato) titanium (IV) acidic hydrolysis and its performance in dye-sensitized solar cells," *Journal of Porous Materials*, vol. 25, no. 5, pp. 1499–1504, 2018.

[12] A. Hagfeldt, G. Boschloo, L. Sun, L. Kloo, and H. Pettersson, "Dye-sensitized solar cells," *Chemical Reviews*, vol. 110, no. 11, pp. 6595–6663, 2010.

[13] M. K. Nazeeruddin, E. Baranoff, and M. Grätzel, "Dye-sensitized solar cells: a brief overview," *Solar Energy*, vol. 85, no. 6, pp. 1172–1178, 2011.

[14] S. Sharma, B. Bulkesh Siwach, S. K. Ghoshal, and D. Mohan, "Dye sensitized solar cells: from genesis to recent drifts," *Renewable and Sustainable Energy Reviews*, vol. 70, pp. 529–537, 2017.

[15] M. Shakeel Ahmad, A. K. Pandey, and N. Abd Rahim, "Advancements in the development of TiO_2 photoanodes and its fabrication methods for dye sensitized solar cell (DSSC) applications. a review," *Renewable and Sustainable Energy Reviews*, vol. 77, pp. 89–108, 2017.

[16] J. Gong, J. Liang, and K. Sumathy, "Review on dye-sensitized solar cells (DSSCs): fundamental concepts and novel materials," *Renewable and Sustainable Energy Reviews*, vol. 16, no. 8, pp. 5848–5860, 2012.

[17] J. Gong, K. Sumathy, Q. Qiao, and Z. Zhou, "Review on dye-sensitized solar cells (DSSCs): advanced techniques and research trends," *Renewable and Sustainable Energy Reviews*, vol. 68, pp. 234–246, 2017.

[18] S. Mozaffari, M. R. Nateghi, and M. B. Zarandi, "An overview of the challenges in the commercialization of dye sensitized solar cells," *Renewable and Sustainable Energy Reviews*, vol. 71, pp. 675–686, 2017.

[19] P. P. Kumavat, P. Sonar, and D. S. Dalal, "An overview on basics of organic and dye sensitized solar cells, their mechanism and recent improvements," *Renewable and Sustainable Energy Reviews*, vol. 78, pp. 1262–1287, 2017.

[20] S. V. Umale, S. N. Tambat, V. Sudhakar, S. M. Sontakke, and K. Krishnamoorthy, "Fabrication, characterization and comparison of DSSC using anatase TiO_2 synthesized by various methods," *Advanced Powder Technology*, vol. 28, no. 11, pp. 2859–2864, 2017.

[21] G. Li, C. P. Richter, R. L. Milot et al., "Synergistic effect between anatase and rutile TiO_2 nanoparticles in dye-sensitized solar cells," *Dalton Transactions*, vol. 45, pp. 10078–10085, 2009.

[22] M. Grätzel, "Solar energy conversion by dye-sensitized photovoltaic cells," *Inorganic Chemistry*, vol. 44, no. 20, pp. 6841–6851, 2005.

[23] K. D. Benkstein, N. Kopidakis, J. van de Lagemaat, and A. J. Frank, "Influence of the percolation network geometry on electron transport in dye-sensitized titanium dioxide solar cells," *Journal of Physical Chemistry B*, vol. 107, no. 31, pp. 7759–7767, 2003.

[24] Y. T. Chung, M. M. Ba-Abbad, A. W. Mohammad, N. H. H. Hairom, and A. Benamor, "Synthesis of minimal-size ZnO nanoparticles through sol-gel method: taguchi design optimisation," *Materials and Design*, vol. 87, pp. 780–787, 2015.

[25] H. Tong, N. Enomoto, M. Inada, Y. Tanaka, and J. Hojo, "Synthesis of mesoporous TiO_2 spheres and aggregates by sol-gel method for dye-sensitized solar cells," *Materials Letters*, vol. 141, pp. 259–262, 2015.

[26] T. Sugimoto, X. Zhou, and A. Muramatsu, "Synthesis of uniform anatase TiO_2 nanoparticles by gel-sol method," *Journal of Colloid and Interface Science*, vol. 259, no. 1, pp. 43–52, 2003.

[27] F. Gu, S. F. Wang, M. K. Lü, G. J. Zhou, D. Xu, and D. R. Yuan, "Photoluminescence properties of SnO_2Nanoparticles synthesized by sol–gel method," *Journal of Physical Chemistry B*, vol. 108, no. 24, pp. 8119–8123, 2004.

[28] E. Lifshitz, I. Dag, I. Litvin et al., "Optical properties of CdSe nanoparticle films prepared by chemical deposition and sol-gel methods," *Chemical Physics Letters*, vol. 288, no. 2–4, pp. 188–196, 1998.

[29] B. Gersten, "Solvothermal synthesis of nanoparticles," *Chemfiles*, vol. 5, pp. 11-12, 2005.

[30] J. Archana, M. Navaneethan, and Y. Hayakawa, "Solvothermal growth of high surface area mesoporous anatase TiO_2 nanospheres and investigation of dye-sensitized solar cell properties," *Journal of Power Sources*, vol. 242, pp. 803–810, 2013.

[31] F. Sauvage, D. Chen, P Comte et al., "Dye-sensitized solar cells employing a single film of mesoporous TiO_2 beads achieve

power conversion efficiencies over 10%," *ACS Nano*, vol. 4, no. 8, pp. 4420–4425, 2010.

[32] D. Chen, F. Huang, Y.-B. Cheng, and R. A. Caruso, "Mesoporous anatase TiO_2beads with high surface areas and controllable pore sizes: a superior candidate for high-performance dye-sensitized solar cells," *Advanced Materials*, vol. 21, no. 21, pp. 2206–2210, 2009.

[33] J. Archana, S. Harish, M. Sabarinathan et al., "Highly efficient dye-sensitized solar cell performance from template derived high surface area mesoporous TiO_2 nanospheres," *RSC Advances*, vol. 6, no. 72, pp. 68092–68099, 2016.

[34] Y. Rui, L. Wang, J. Zhao et al., "Template-free synthesis of hierarchical TiO_2 hollow microspheres as scattering layer for dye-sensitized solar cells," *Applied Surface Science*, vol. 369, pp. 170–177, 2016.

[35] Z.-Q. Li, Y.-P. Que, L.-E. Mo et al., "One-pot synthesis of mesoporous TiO_2 micropheres and its application for high-efficiency dye-sensitized solar cells," *ACS Applied Materials & Interfaces*, vol. 7, no. 20, pp. 10928–10934, 2015.

[36] A. E. J. González and S. G. Santiago, "Structural and opto-electronic characterization of TiO_2 films prepared using the sol-gel technique," *Semiconductor Science and Technology*, vol. 22, no. 7, pp. 709–716, 2007.

[37] C.-C. Wang and J. Y. Ying, "Sol-gel synthesis and hydrothermal processing of anatase and rutile titania nanocrystals," *Chemistry of Materials*, vol. 11, no. 11, pp. 3113–3120, 1999.

[38] B. A. Morales, O. Novaro, T. López, E. Sánchez, and R. Gómez, "Effect of hydrolysis catalyst on the Ti deficiency and crystallite size of sol-gel-TiO_2 crystalline phases," *Journal of Materials Research*, vol. 10, no. 11, pp. 2788–2796, 1995.

[39] C. J. Brinker and G. W. Scherer, *Sol-Gel Science: The Physics and Chemistry of Sol-Gel Processing*, Academic Press INC, Cambridge, MA, USA, 1990.

[40] T. Tesfamichael, G. Will, J. Bell, K. Prince, and N. Dytlewski, "Characterization of a commercial dye-sensitised titania solar cell electrode," *Solar Energy Materials and Solar Cells*, vol. 76, no. 1, pp. 25–35, 2003.

[41] J. Tauc, "Absorption edge and internal electric fields in amorphous semiconductors," *Materials Research Bulletin*, vol. 5, no. 8, pp. 721–729, 1970.

[42] H.-J. Kim, J.-D. Jeon, and S.-Y. Kwak, "Highly dispersed mesoporous TiO_2 spheres via acid treatment and its application for dye-sensitized solar cells," *Powder Technology*, vol. 243, pp. 130–138, 2013.

[43] L. B. McCusker, F. Liebau, and G. Engelhardt, "Nomenclature of structural and compositional characteristics of ordered microporous and mesoporous materials with inorganic hosts," *Microporous and Mesoporous Materials*, vol. 58, no. 1, pp. 3–13, 2003.

[44] N. Laidani, R. Bartali, G. Gottardi, M. Anderle, and P. Cheyssac, "Optical absorption parameters of amorphous carbon films from Forouhi–Bloomer and Tauc–Lorentz models: a comparative study," *Journal of Physics: Condensed Matter*, vol. 20, no. 1, article 015216, 2008.

[45] J. Du, J. Zhang, and D. J. Kang, "Controlled synthesis of anatase TiO_2 nano-octahedra and nanospheres: shape-dependent effects on the optical and electrochemical properties," *CrystEngComm*, vol. 13, no. 12, p. 4270, 2011.

[46] M. A. Sánchez-García, X. Bokhimi, A. Maldonado-Álvarez, and A. E. Jiménez-González, "Effect of anatase synthesis on the performance of dye-sensitized solar cells," *Nanoscale Research Letters*, vol. 10, no. 1, p. 306, 2015.

[47] K. S. Swathy, P. A. Abraham, N. R. Panicker, N. C. Pramanik, and K. S. Jacob, "Nanostructured anatase titania spheres as light scattering layer in dye-sensitized solar cells," *Procedia Technology*, vol. 24, pp. 767–773, 2016.

[48] C. Dwivedi, V. Duttaa, A. K. Chandiranb, V. Chandiran, M. K. Nazeeruddin, and M. Grätzel, "Anatase TiO_2 hollow microspheres fabricated by continuous spray pyrolysis as a scattering layer in dye-sensitised solar cells," *Energy Procedia*, vol. 33, pp. 223–227, 2013.

[49] X. Miao, K. Pan, Y. Liao et al., "Controlled synthesis of mesoporous anatase TiO_2 microspheres as a scattering layer to enhance the photoelectrical conversion efficiency," *Journal of Materials Chemistry A*, vol. 1, no. 34, p. 9853, 2013.

[50] M.-J. Jeng, Y.-L. Wung, L.-B. Chang, and L. Chow, "Dye-sensitized solar cells with anatase TiO_2 nanorods prepared by hydrothermal method," *International Journal of Photoenergy*, vol. 2013, Article ID 563897, 9 pages, 2013.

Hindawi
Advances in Materials Science and Engineering
Volume 2019, Article ID 5190235, 7 pages
https://doi.org/10.1155/2019/5190235

Research Article

Oxide Nanomaterials Based on SnO_2 for Semiconductor Hydrogen Sensors

George Fedorenko, Ludmila Oleksenko, and Nelly Maksymovych

Taras Shevchenko National University of Kyiv, 62a Volodymyrska Str., Kyiv 01601, Ukraine

Correspondence should be addressed to George Fedorenko; georgf@ukr.net

Received 11 April 2019; Accepted 18 July 2019; Published 5 August 2019

Guest Editor: Arslan Shehzad

Nanosized tin dioxide with an average particle size of 5.3 nm was synthesized by a sol-gel method and characterized by IR spectroscopy, TEM, X-ray, and electron diffraction. The obtained SnO_2 can be used as initial material for creation of gas-sensitive layers of adsorption semiconductor sensors. Addition of palladium into the initial nanomaterial allows to improve response to hydrogen of such sensors in comparison with sensors based on undoped SnO_2 and provides fast response and recovery time, a wide measuring range of hydrogen content in air ambient, and good repeatability of the sensor signal. Such promising properties could make useful the sensors based on these nanomaterials for devices intended to determine hydrogen in air.

1. Introduction

Nowadays, development of nanosized oxides is actual for obtaining functional materials with required properties. In particular, such nanomaterials can be useful for creating adsorption semiconductor gas sensors intended to determine the presence of combustible gases, e.g., hydrogen, in air. Different semiconductor oxides, such as SnO_2, TiO_2, ZnO, ZrO_2, and WO_3 [1–5], can be used as initial materials for gas-sensitive layers of the sensors. Tin dioxide among them is the most popular due to its chemical stability, band structure, and extreme sensitivity of its conductivity to the surface state where the molecules adsorbed on the SnO_2 surface are actively engaged in chemical reactions occurred in the temperature range 20–500°C [6–11]. It is known that a decrease in the particle size of semiconductor material can lead to increase in the ratio of the atoms fraction on the surface of particles to the atoms fraction in their volume that makes impact of the surface processes into the material properties significant [12]. Thus, the sensitivity of the adsorption semiconductor sensors should depend greatly on the morphology of the materials of the gas-sensitive layers: a decrease in the semiconductor particle size of the gas-sensitive material could cause an increase in the sensor response as it was experimentally observed by other authors [13–16].

Increase in the sensor response can also be achieved by introducing catalytically active additives into the semiconductor materials of the gas-sensitive layers [13]. It leads to an increase in the rate of the catalytic reaction of the analyzed gas with oxygen chemisorbed on the sensor surface that in turn increases the sensor response [13]. Palladium can be such an additive for hydrogen sensors due to its high catalytic activity in the hydrogen oxidation reaction [17].

Thus, usage of tin dioxide nanomaterial doped with the palladium additive is promising to provide high sensitivities of the semiconductor sensors to hydrogen.

The aim of this work is to synthesize oxide nanomaterials based on tin dioxide with the addition of palladium for creation of highly sensitive adsorption semiconductor sensors to hydrogen.

2. Experimental

Initial nanosized tin dioxide was synthesized by a sol-gel process through chemical oxidation of tin (II) oxalate by 35% solution of H_2O_2 [18]. Tin (II) oxalate (3 g) was gradually added under stirring to 10 ml of 35% solution of hydrogen peroxide in water. After two hours, a resulting sol was quickly heated to decompose the excess of the hydrogen peroxide and evaporate the water. As a result, a transparent

water-based gel was obtained, and then it was dried at 90°C for 24 hours until the gel turned into a yellowish translucent xerogel [19]. The xerogel was calcinated at different temperatures and temperature holding times for obtaining crystalline nanoscale SnO_2 particles with minimal sizes.

In order to optimize the temperature treatment conditions of the obtained xerogel, its thermal decomposition was studied in air with a heating rate of 10°C/min on a DTG-60H derivatograph (Shimadzu, Japan).

Gas-sensitive nanomaterials based on unmodified SnO_2 and tin dioxide doped with 0.24 wt.% palladium were obtained through applying a paste formed by mixing the initial nanosized SnO_2 with aqueous solution of carboxymethylcellulose (CMC) onto ceramic plates with subsequent drying at 90°C. Impregnation of the dried paste with a solution of palladium (II) chloride in dilute hydrochloric acid was performed with subsequent drying at 90°C in order to obtain palladium-doped gas-sensitive material. The coated ceramic plates were then heated at temperatures up to 620°C in order to provide decomposition of $PdCl_2$ and CMC.

The amount of palladium introduced into the gas-sensitive material was determined by X-ray fluorescence analysis (ElvaX EXS–01, Elvatech, Ukraine).

The morphology of the synthesized nanomaterial was studied by transmission electron microscopy on a SELMI PEM-125K device (Ukraine) with an accelerating voltage of 100 kV.

The phase composition of the materials was studied using a LabX XRD-6000 diffractometer, Shimadzu (Japan) (CuKα radiation). Particle sizes of the nanomaterials were estimated using the Scherrer equation [20]:

$$D = \frac{k\lambda}{\beta \cdot \cos\theta}, \quad (1)$$

where D is XRD particle size; k is a constant that depends on crystallite shape and is close to unity (for our calculation k was equal to 0.9); λ is the wavelength of CuKα radiation ($\lambda = 1{,}5418$ Å); β is a true broadening of diffraction peak ($\beta = \Delta - b$, where Δ is an experimental broadening of the diffraction peak; b is an instrumental broadening); and θ is a Bragg angle. The lattice parameters of the materials were calculated using a program UnitCell.

The specific surface areas of the xerogel temperature treatment products were determined by the argon thermal desorption method using Al_2O_3 as a standard sample ($S_{sp} = 22\ m^2/g$). Before measurements, the investigated samples were degassed in a helium stream at 300–350°C for two hours.

The infrared spectra of the samples were recorded on a PerkinElmer BX spectrophotometer (USA).

The sensors were made on the basis of planar ceramic plates by the same preparation method as the gas-sensitive nanomaterials. The paste (mixture of the initial nanosized SnO_2 with the 3% solution of CMC in water) was deposited between measuring electrodes on the one side of the ceramic sensor plate. The other side of the plate contained a platinum heater for controlling the operational temperature of the sensor. Dimensions of the sensors plates were $1.8 \times 1.8 \times 0.3$ mm. Design of the sensor in more detail is presented in [21].

The sensor parameters were determined in a special electric stand. The electrical circuit of the stand was presented in [22]. A hydrogen-air mixture with 44 ppm H_2 was used to measure the sensor responses at different operational temperatures in order to find optimal hydrogen sensing conditions.

Stabilization of the sensor electrical conductivities was achieved by pretreatment of the sensors for three days at the operational temperature of 405°C with a periodic supply of the hydrogen-air mixture (935 ppm H_2) to the measuring chambers where the sensors were placed.

The ratio of the sensor electrical conductivity in hydrogen-air mixture (σ_g) to the electrical conductivity in clean air (σ_0) was taken as a measure of the sensor response to this hydrogen content in air ambient (γ): $\gamma = \sigma_g/\sigma_0$.

Two parameters (response time ($\tau_{0.9}$) and recovery time (τ_{relax})) were used to estimate the dynamic properties of the sensors. A value $\tau_{0.9}$ was estimated as the time required for conductivity signal of the sensor to attain 90% of its equilibrium value after an injection of the hydrogen-air mixture to the measuring chamber of the sensor. The recovery time (τ_{relax}) was estimated as the time required for the conductivity signal of the sensor to attain 10% of its equilibrium value in the hydrogen-air mixture after applying clean air to the measuring chamber.

3. Results and Discussion

Study by the DTA-DTG method of the thermal decomposition process of the obtained xerogel (Figure 1) showed that a weight loss occurs in several steps. The first step (up to 100°C) corresponds to loss of physically sorbed water (~10 wt.%) with endoeffect at 43°C on the DTA curve. Further increase in the temperature up to 600°C leads to a weight loss (~8 wt.%) corresponding to the removal of the strongly bounded water. It should be noted that in this temperature range, partial crystallization of the tin dioxide can also occur and a presence of a broadened peak of exoeffect on the DTA curve (Figure 1) could indicate this process.

Several absorption bands can be observed in the IR spectra of the xerogel and the materials obtained by its temperature treatment up to 400°C with isothermal exposure at this temperature during 1 hour 20 minutes and 2 hours 20 minutes: the absorption band at 1632 cm^{-1} that refers to deformation vibrations of the adsorbed water, a wide absorption band in the region at 3000–3600 cm^{-1} corresponding to the total contribution of stretching vibrations of surface hydroxyl groups and the water adsorbed on the surface, and two intense absorption bands in the region at 550–600 cm^{-1} and 650–680 cm^{-1} corresponding to vibrations of the bond between tin atoms and oxygen for the terminal and bridge fragments, respectively [23, 24]. In the last case, the absorption band at 660 cm^{-1} is the characteristic for the O-Sn-O fragment [24]. It should be noted that an increase in the duration of the temperature treatment of the xerogel from 1 hour 20 minutes to 2 hours 20 minutes

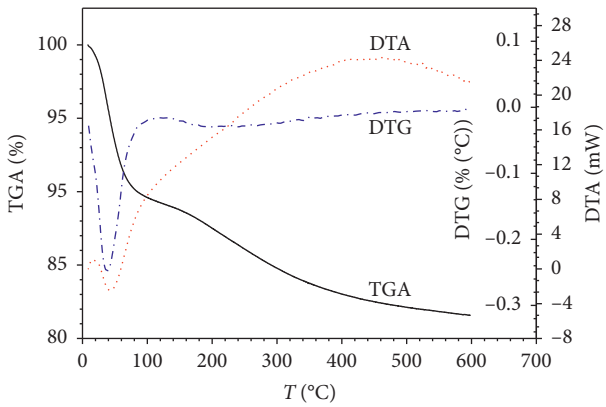

Figure 1: Thermal analysis data for xerogel.

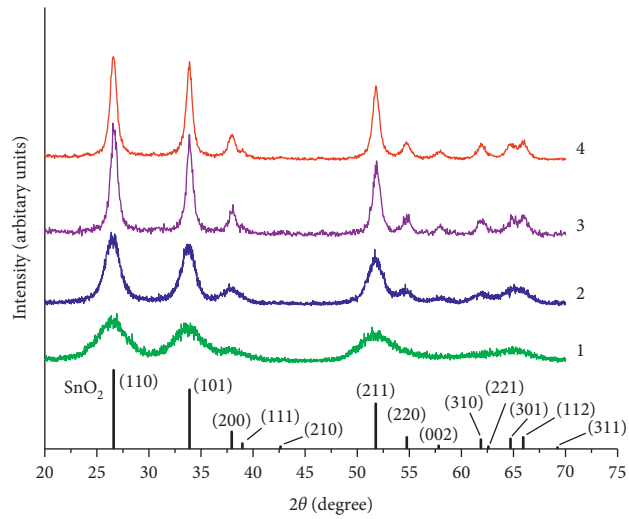

Figure 2: XRD data for xerogel (1); material obtained through temperature treatment of xerogel at 400°C during 2 hours 20 minutes (2); undoped sensor material (3); sensor material doped with 0.24 wt.% Pd (4).

leads to a slight shift (5 cm^{-1}) of the absorption band at 650–680 cm^{-1} to the larger wave numbers region. In these conditions, the absorption band at 590 cm^{-1} for the xerogel shifts to 616 cm^{-1} and to 631 cm^{-1} after 1 hour 20 minutes and 2 hour 20 minutes at 400°C, respectively, due to the formation of the crystalline structure of the nanomaterial [24, 25].

Additional formation of the SnO_2 structure accompanied with rearrangement of tin and oxygen atoms after the temperature treatment of the xerogel is also evidenced by a change in the ratio between the intensity of the absorption bands corresponded to the terminal Sn-O groups and to the bridge fragments. Higher band intensity of the terminal fragments in comparison with the bridge ones in the material heated at 400°C for 2 hours 20 minutes may be attributed to the formation of the SnO_2 crystal structure as it was observed for the materials obtained in [25].

According to the XRD analysis (Figure 2), the diffraction patterns of the xerogel and the materials obtained after xerogel thermal treatment at the temperature range of 400–600°C are broadened that indicates the nanoscale nature of the samples regardless of their isothermal processing time (1 hour 20 min and 2 hours 20 min) at different temperatures (Table 1). It was established that all obtained materials have the cassiterite structure (ICDD PDF-2 Version 2.0602 (2006), card no. 00-041-1445). Calculated lattice parameters are listed in Table 1. Estimation of the materials XRD particle sizes using the Scherrer equation has shown that the SnO_2 particle sizes increase from 4.8 to 12.1 nm (Table 1) with an increase in the isothermal processing temperature of the xerogel. Such increase should lead to a decrease in the specific surface area (S_{sp}) of the material that was experimentally observed: the value of S_{sp} decreased from 110 to 37 m^2/g when isothermal processing temperature increased from 400 to 600°C (Table 1).

It should be noted that changes in isothermal processing time do not make any significant influence on the specific surface area: the value of S_{sp} decreases from 85 to 81 m^2/g at 450°C and from 60 to 58 m^2/g at 500°C when the processing time increases from 1 hour 20 minutes to 2 hour 20 minutes, respectively. Thus, it can be assumed that exposure temperature makes a greater impact on the particles sizes than the processing time. For the samples obtained through the temperature treatment of the xerogel at 400°C during 1 hour 20 minutes, the specific surface area was not measured because the preparation of the sample required high-temperature degasation in the argon flow (the temperature range 300–350°C) that can make changes in the incompletely formed crystal structure of this material. Thus, the obtained value of the specific surface area will not be objective and representative.

The TEM study of the material obtained by the xerogel thermal treatment at 400°C for 2 hours 20 minutes showed that it consisted of individual nanoparticles with sizes from 3 to 9 nm (average size of the nanoparticles is 5–6 nm) (Figure 3(a)). The presence of the nanosized crystalline particles for this material is confirmed by the ring-shaped electron diffraction pattern presented in the inset of Figure 3(a). The specific surface area of the synthesized nanosized tin dioxide is 110 m^2/g (Table 1).

Thus, the thermal treatment of the xerogel up to 400°C during 2 hours 20 minutes is sufficient to provide formation of the nanoscale crystalline SnO_2 with an average particle size 5–6 nm. This material was chosen as the initial for creating the adsorption semiconductor sensors. To increase their sensitivity to hydrogen, a small amount of palladium (0.24 wt.%) was added into the gas-sensitive layer. Both types of the obtained gas-sensitive materials (undoped and doped with 0.24 wt.% Pd) consist of the nanosized particles observed by TEM (Figures 3(b) and 3(c)). According to the XRD study, only cassiterite phase was present in the gas-sensitive material (Figure 2). The XRD sizes of SnO_2 particles are 13.9 and 12.6 nm for the undoped and doped with 0.24 wt.% Pd materials, respectively, that could be explained by a stabilization role of the palladium additives [26].

As can be seen in Figure 4, the palladium additive increases the conductivities of the sensors that can be attributed to the increase in the number of defects in the tin dioxide crystal structure that were formed during the

Table 1: Particle sizes of SnO_2 calculated by using the Scherrer equation, lattice parameters, and specific surface areas of the nanomaterials obtained through thermal treatment of the xerogel.

Sample	Nanomaterial formation conditions		XRD size (nm)	S_{sp} (m^2/g)	Lattice parameters	
	T (°C)	Isothermal processing time			a (Å)	c (Å)
Xerogel	90	24 h	~3		4.77 ± 0.03	3.171 ± 0.06
SnO_2	400	1 h 20 min	4.8		4.732 ± 0.005	3.190 ± 0.005
SnO_2	400	2 h 20 min	5.3	110	4.739 ± 0.005	3.180 ± 0.005
SnO_2	450	1 h 20 min	6.5	85	4.749 ± 0.005	3.191 ± 0.005
SnO_2	500	1 h 20 min	8.3	60	4.745 ± 0.005	3.189 ± 0.005
SnO_2	550	1 h 20 min	9.9	48	4.743 ± 0.005	3.185 ± 0.005
SnO_2	600	1 h 20 min	12.1	37	4.72 ± 0.005	3.190 ± 0.005

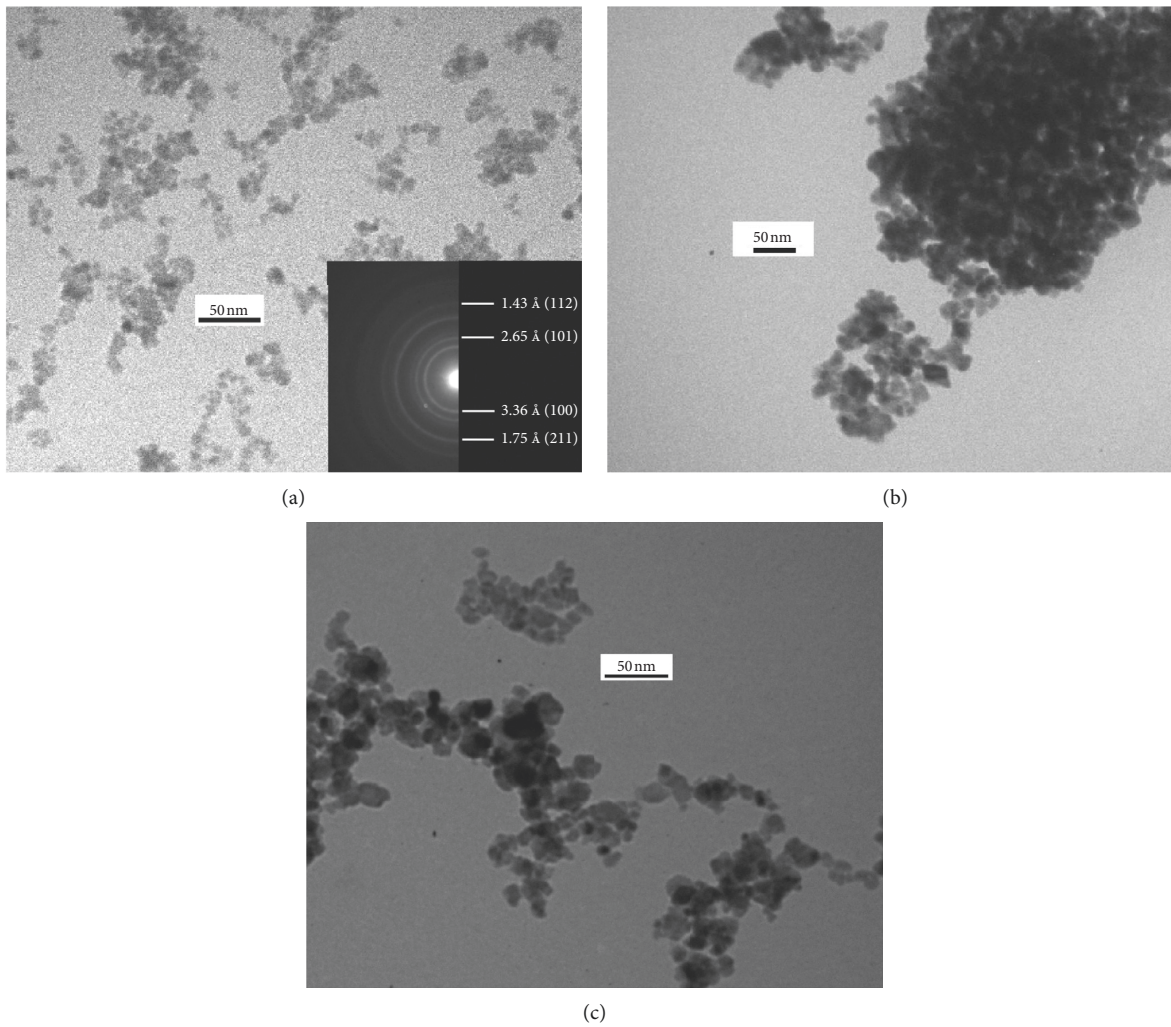

Figure 3: TEM image of the (a) material obtained through calcination of the xerogel at 400°C during 2 hour 20 minutes (electron diffraction with d-spacing and corresponding *hkl* indices for SnO_2 (in round brackets) is presented in the inset), (b) undoped, and (c) doped with 0.24 wt.% Pd gas-sensitive materials on the base of nanosized SnO_2.

high-temperature sensor treatment process due to the introduction of palladium [27]. It should be noted that both types of the sensors (based on unmodified SnO_2 and Pd/SnO_2) demonstrate extreme dependences of the gas-sensitive layer conductivities on the operational temperature of the sensor. Such character of the conductivity changes can be caused by the influence of oxygen adsorption-desorption processes occurring on the sensor surface. An increase in the operational temperature of the sensors from 225 to 290°C (for the sensors based on Pd/SnO_2) and up to 325–345°C (for the sensors based on unmodified SnO_2) can lead to an increase in the amount of the chemisorbed oxygen that, in turn, leads to a decrease in the sensors conductivities [13, 14]. A following increase

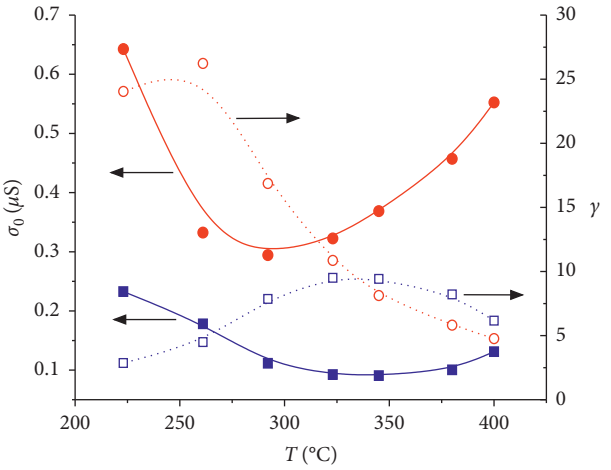

FIGURE 4: Dependencies of conductivity in air (σ_0) and response to hydrogen (γ) of the sensors based on undoped SnO_2 (squares connected by blue lines) and Pd/SnO_2 (circuits connected by red lines) on the sensor operational temperature.

in the operational temperature of the sensor can facilitate the desorption of the chemisorbed oxygen and, thus, leads to an increase in the sensor conductivity (Figure 4).

As can be seen from Figure 4, the sensors based on the unmodified SnO_2 have the highest response value to 44 ppm H_2 (ca. 9.4–9.5) at the same temperature range where the minimal conductivities of the sensors were observed (325–345°C, Figure 4). Such behavior of the sensor parameter changes allowed to conclude that the formation of the sensor responses is greatly influenced by the amount of the chemisorbed oxygen available for the hydrogen oxidation. For the sensors based on the Pd/SnO_2 material, the highest sensor responses to 44 ppm H_2 are observed at 260°C, and it is equal to ~26 which is much higher than the responses to H_2 of the sensors without any additives (Figure 4). The discrepancy between the maximum of the γ dependence on temperature (260°C) and the minimum of the σ_0 dependence on temperature (290°C) can be explained by the significant catalytic activity of palladium in the hydrogen oxidation reaction [17]. Above 260°C, the hydrogen oxidation rate on the palladium can be high enough to provide the formation of reaction products in a large amount. The products prevent or complicate the consumption of the oxygen chemisorbed on the tin dioxide surface by the hydrogen oxidation reaction that occurred on palladium, and thus, such "blocking" of the sensor surface could reduce the sensor responses to hydrogen [13, 14]. The assumption of SnO_2 surface blocking by the hydrogen oxidation products and the oxygen desorption correlates well with a further decrease in the sensitivities of the Pd/SnO_2-based sensors with an increase in their operational temperature. It can be seen (Figure 4) that the sensor responses in the operational temperature range of 345–400°C become even less than the responses of the sensors based on the unmodified SnO_2 probably due to almost complete isolation of the tin dioxide surface from hydrogen by increasing the amount of the reaction products formed on the palladium particles.

To assess the potential usage of the Pd/SnO_2-based sensors for hydrogen detection in air, the dependences of conductivity changes on time with the change of analyzed gas mixtures surrounding the sensors were studied at the different operational temperatures of the sensors (Figure 5). It was found that in the operational temperature range of 260–400°C, the sensors possess good dynamic properties: a steady-state conductivity level in the presence of 44 ppm H_2 and in clean air is attained quickly. In particular, values $\tau_{0,9}$ are in the range of 8–29 s and τ_{relax} falls in the range 12–28 s depending on the operational temperature of the sensor (Table 2).

As can be seen in Figure 5, the time required to achieve the steady-state conductivity level in the presence of 44 ppm H_2 at the sensor operational temperature 225°C is ca. 7 minutes that is significantly bigger in comparison with the higher operational temperatures. Further increase in the operational temperature will lead to an improvement of the sensor dynamic properties, since the rates of the chemical reactions (oxygen chemisorption and catalytic reaction of hydrogen oxidation), the diffusion of the reagents into the gas-sensitive layer, and the rates of the reaction products elimination from the sensor surface increase significantly at the higher sensor temperatures. This statement is in good correspondence with observed experimental data (Figure 5 and Table 2). It is clear from Table 2 that the values of $\tau_{0,9}$ and τ_{relax} decrease with the increase in the operational temperature of the sensor. Obtained values are better than those previously reported in the literature (where $\tau_{0,9} = 2$ min and $\tau_{relax} = 15$ min at 300°C) [28]. Thus, the comparison of the sensor responses data with their dynamic properties allowed to determine the optimal operational temperature for the 0.24 wt.% Pd/SnO_2-based sensors (about 260°C).

To determine a range of the hydrogen detection in air for the Pd/SnO_2-based sensor, the dependences of changes in the sensor conductivities on the hydrogen content in air ambient were studied in the concentration interval 3–935 ppm H_2 at the optimal sensor operational temperature (260°C) (Figure 6). It can be seen that the studied sensor can measure hydrogen in the wide range of its concentration: the response values of the sensors were found to be 5.7 and 193 for 3 and 935 ppm H_2 in air ambient, respectively. Besides, the conductivity level of the sensor in the presence of 3 ppm H_2 demonstrates good repeatability (inset in Figure 6). There are no evidences of a memory effect of the sensor and distortion of the conductivity value in 3 ppm H_2 by influence of 935 ppm H_2 applied to the sensor previously. Thus, the sensors based on Pd/SnO_2 can be used for the reliable detection of hydrogen in air ambient.

The dependence of the conductivity of the sensor based on Pd/SnO_2 on the hydrogen content in air is shown in Figure 7. As it can be seen, in linear scale, σ_g increases with increasing the H_2 content in air over all the measured hydrogen concentration ranges. In logarithmic scale, the dependence is linear and its slope is equal to 0.62:

$$\ln(\sigma_g) = -13.83 + 0.62 \cdot \ln(C_{H_2}). \quad (2)$$

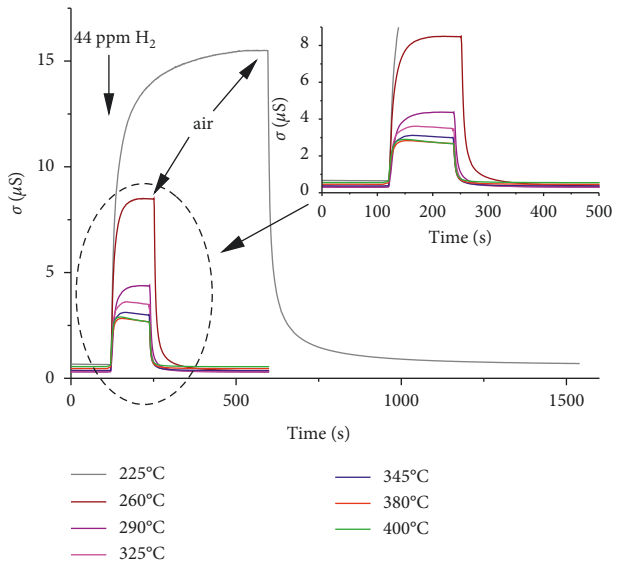

Figure 5: Change in conductivity in time for the 0.24 wt.% Pd/SnO_2-based sensor at different operational temperatures when gas mixture surrounding the sensor was subsequently changed from air to 44 ppm H_2 in air ambient and from 44 ppm H_2 to air.

Table 2: Response ($\tau_{0,9}$) and recovery (τ_{relax}) times to 44 ppm H_2 in air ambient for the 0.24 wt.% Pd/SnO_2-based sensor at its different operational temperatures.

T (°C)	225	260	290	325	345	380	400
$\tau_{0,9}$ (s)	128	29	23	15	12	10	8
τ_{relax} (s)	78	28	23	21	15	13	12

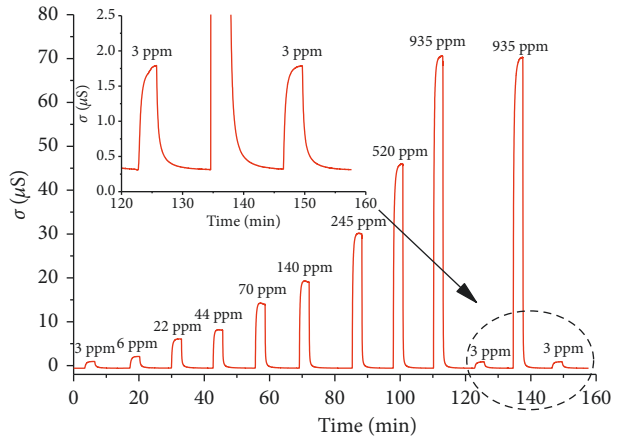

Figure 6: Change in conductivity for the 0.24 wt.% Pd/SnO_2-based sensor versus stepwise change of hydrogen concentration in gas mixture surrounding the sensors at sensor temperature 260°C.

The obtained value for the slope is in good correspondence with the reported data for the typical slope of the conductivity dependence on the concentration of the reducing gases for the adsorption semiconductor sensors in the logarithmic scale [29]. The ability to linearize well the dependence in the logarithmic scale makes a periodic calibration of the sensor during its operation easier because it can be performed using at least two points of H_2 concentrations only.

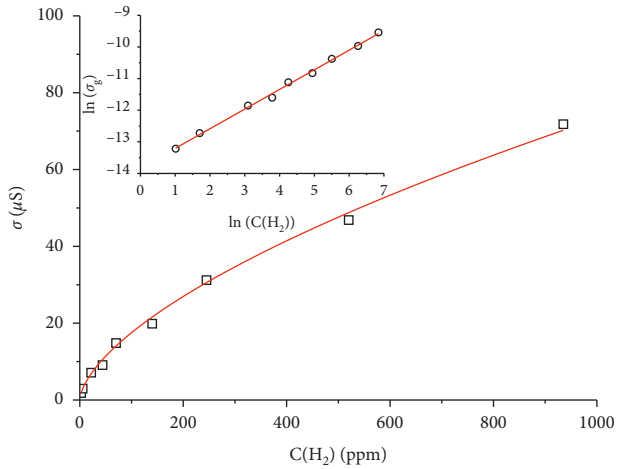

Figure 7: Dependence of conductivity for 0.24 wt.% Pd/SnO_2-based sensor versus H_2 concentration in air ambient in linear and logarithmic scales (inset).

4. Conclusions

Nanosized tin dioxide material with an average particle size of 5.3 nm allowed to create Pd-doped gas-sensitive material for highly sensitive hydrogen sensors. The optimal sensors based on Pd/SnO_2 nanomaterial possess a high response to microconcentration of H_2 (44 ppm in air ambient), a wide range of hydrogen detection in air (3–935 ppm H_2), good stability, lack of the sensor memory effect after exposure to a high hydrogen concentration, and good dynamic properties. These properties make the studied sensors promising for further application in creation of gas analytical devices intended to detect H_2 in air ambient.

Data Availability

The data used to support the findings of this study are included within the article.

Conflicts of Interest

The authors declare that they have no conflicts of interest.

References

[1] S. Basu and A. Dutta, "Room-temperature hydrogen sensors based on ZnO," *Materials Chemistry and Physics*, vol. 47, no. 1, pp. 93–96, 1997.

[2] I. S. Mulla, S. D. Pradhan, and K. Vijayamohanan, "Humidity-sensing behaviour of surface-modified zirconia," *Sensors and Actuators A: Physical*, vol. 57, no. 3, pp. 217–221, 1996.

[3] V. Guidi, M. C. Carotta, M. Ferroni, G. Martinelli, and M. Sacerdoti, "Effect of dopants on grain coalescence and oxygen mobility in nanostructured titania anatase and rutile," *The Journal of Physical Chemistry B*, vol. 107, no. 1, pp. 120–124, 2003.

[4] A. A. Tomchenko, V. V. Khatko, and I. L. Emelianov, "WO_3 thick-film gas sensors," *Sensors and Actuators B: Chemical*, vol. 46, no. 1, pp. 8–14, 1998.

[5] G. Kelp, T. Tätte, S. Pikker et al., "Self-assembled SnO_2 micro- and nanosphere-based gas sensor thick films from an alkoxide-derived high purity aqueous colloid precursor," *Nanoscale*, vol. 8, no. 13, pp. 7056–7067, 2016.

[6] M. Batzill and U. Diebold, "The surface and materials science of tin oxide," *Progress in Surface Science*, vol. 79, no. 2–4, pp. 47–154, 2005.

[7] G. De, A. Licciulli, C. Massaro et al., "Sol-gel derived pure and palladium activated tin oxide films for gas-sensing applications," *Sensors and Actuators B: Chemical*, vol. 55, no. 2-3, pp. 134–139, 1999.

[8] J. C. Kim, H. K. Jun, J.-S. Huh, and D. D. Lee, "Tin oxide-based methane gas sensor promoted by alumina-supported Pd catalyst," *Sensors and Actuators B: Chemical*, vol. 45, no. 3, pp. 271–277, 1997.

[9] A. Cabot, J. Arbiol, J. R. Morante, U. Weimar, N. Bârsan, and W. Göpel, "Analysis of the noble metal catalytic additives introduced by impregnation of as obtained SnO_2 sol-gel nanocrystals for gas sensors," *Sensors and Actuators B: Chemical*, vol. 70, no. 1–3, pp. 87–100, 2000.

[10] F. Pourfayaz, Y. Mortazavi, A. Khodadadi, and S. Ajami, "Ceria-doped SnO_2 sensor highly selective to ethanol in humid air," *Sensors and Actuators B: Chemical*, vol. 130, no. 2, pp. 625–629, 2008.

[11] A. V. Marikutsa, M. N. Rumyantseva, A. M. Gaskov, and A. M. Samoylov, "Nanocrystalline tin dioxide: basics in relation with gas sensing phenomena. Part I. physical and chemical properties and sensor signal formation," *Inorganic Materials*, vol. 51, no. 13, pp. 1329–1347, 2015.

[12] E. Roduner, "Size matters: why nanomaterials are different," *Chemical Society Reviews*, vol. 35, no. 7, pp. 583–592, 2006.

[13] T. A. Miller, S. D. Bakrania, C. Perez, and M. S. Wooldridge, "Nanostructured tin dioxide materials for gas sensor applications," in *Functional Nanomaterials*, K. E. Geckeler and E. Rosenberg, Eds., p. 515, American Scientific Publishers, Valencia, Spain, 2006.

[14] N. Yamazoe and K. Shimanoe, "New perspectives of gas sensor technology," *Sensors and Actuators B: Chemical*, vol. 138, no. 1, pp. 100–107, 2009.

[15] A. Gurlo, "Nanosensors: towards morphological control of gas sensing activity. SnO_2, In_2O_3, ZnO and WO_3 case studies," *Nanoscale*, vol. 3, no. 1, pp. 154–165, 2011.

[16] C. Xu, J. Tamaki, N. Miura, and N. Yamazoe, "Grain size effects on gas sensitivity of porous SnO_2-based elements," *Sensors and Actuators B: Chemical*, vol. 3, no. 2, pp. 147–155, 1991.

[17] N. Yamazoe, Y. Kurokawa, and T. Seiyama, "Effects of additives on semiconductor gas sensors," *Sensors and Actuators*, vol. 4, pp. 283–289, 1983.

[18] R. Alcántara, F. F. Madrigal, P. Lavela, C. Pérez-Vicente, and J. Tirado, "Tin oxalate as a precursor of tin dioxide and electrode materials for lithium-ion batteries," *Journal of Solid State Electrochemistry*, vol. 6, no. 1, pp. 55–62, 2001.

[19] L. P. Oleksenko, G. V. Fedorenko, and N. P. Maksymovych, "Platinum-containing adsorption-semiconductor sensors based on nanosized tin dioxide for methane detection," *Theoretical and Experimental Chemistry*, vol. 53, no. 4, pp. 259–264, 2017.

[20] C. Hammond, *The Basics of Crystallography and Diffraction*, Oxford University Press, Oxford, UK, 2009.

[21] V. Vorotyntsev, N. Maksimovich, L. Yeremina, O. Kaskevich, and N. Nikitina, "Adsorption semiconductor gas sensors and heterogeneous catalytic reaction mechanisms," *Sensors and Actuators B: Chemical*, vol. 36, no. 1–3, pp. 333–337, 1996.

[22] G. V. Fedorenko, L. P. Oleksenko, N. P. Maksymovych, and I. P. Matushko, "Semiconductor adsorption sensors based on nanosized Pt/SnO_2 materials and their sensitivity to methane," *Russian Journal of Physical Chemistry A*, vol. 89, no. 12, pp. 2259–2262, 2015.

[23] G. Zhang and M. Liu, "Preparation of nanostructured tin oxide using a sol-gel process based on tin tetrachloride and ethylene glycol," *Journal of Materials Science*, vol. 34, no. 13, pp. 3213–3219, 1999.

[24] J. C. Giuntini, W. Granier, J. V. Zanchetta, and A. Taha, "Sol-gel preparation and transport properties of a tin oxide," *Journal of Materials Science Letters*, vol. 9, no. 12, pp. 1383–1388, 1990.

[25] B. Orel, U. Lavrenčič-Štankgar, Z. Crnjak-Orel, P. Bukovec, and M. Kosec, "Structural and FTIR spectroscopic studies of gel-xerogel-oxide transitions of SnO_2 and SnO_2: Sb powders and dip-coated films prepared via inorganic sol-gel route," *Journal of Non-Crystalline Solids*, vol. 167, no. 3, pp. 272–288, 1994.

[26] G. Fedorenko, L. Oleksenko, N. Maksymovych, G. Skolyar, and O. Ripko, "Semiconductor gas sensors based on Pd/SnO_2 nanomaterials for methane detection in air," *Nanoscale Research Letters*, vol. 12, no. 1, p. 329, 2017.

[27] K. Chatterjee, S. Chatterjee, A. Banerjee et al., "The effect of palladium incorporation on methane sensitivity of antimony doped tin dioxide," *Materials Chemistry and Physics*, vol. 81, no. 1, pp. 33–38, 2003.

[28] Y. C. Lee, H. Huang, O. K. Tan, and M. S. Tse, "Semiconductor gas sensor based on Pd-doped SnO_2 nanorod thin films," *Sensors and Actuators B: Chemical*, vol. 132, no. 1, pp. 239–242, 2008.

[29] N. Yamazoe and K. Shimanoe, "Theory of power laws for semiconductor gas sensors," *Sensors and Actuators B: Chemical*, vol. 128, no. 2, pp. 566–573, 2008.

Hindawi
Advances in Materials Science and Engineering
Volume 2019, Article ID 2629464, 7 pages
https://doi.org/10.1155/2019/2629464

Research Article

Deposition of Gold Nanoparticles via Galvanic Replacement in DMSO and Their Influence on Formation of Silicon Nanostructures

Mariana Shepida,[1] **Orest Kuntyi**,[1] **Stepan Nichkalo**,[1] **Galyna Zozulya**,[1] **and Sergiy Korniy**[2]

[1]*Lviv Polytechnic National University, Lviv 79013, Ukraine*
[2]*Karpenko Physico-Mechanical Institute of the NAS of Ukraine, Lviv 79060, Ukraine*

Correspondence should be addressed to Mariana Shepida; maryana_shepida@ukr.net

Received 7 February 2019; Revised 11 April 2019; Accepted 21 April 2019; Published 16 May 2019

Guest Editor: Pradip Basnet

The process of gold nanoparticle (AuNP) precipitation on the silicon (Si) surface by galvanic replacement (GR) in dimethyl sulfoxide (DMSO) solution depending on the concentration of $H[AuCl_4]$, temperature, and duration was investigated. It is established that with an increase in the concentration of $[AuCl_4]^-$ ions (from 2 to 8 mM $H[AuCl_4]$), both the size of AuNPs and their surface coverage density are increased. It is demonstrated that an increase in temperature causes the size of AuNPs to increase from 40 to 80 nm at 40°C to 80–120 and 120–160 nm at 50 and 60°C, respectively. As the duration of the GR process increases, there is a tendency of the particle size growth. Under the studied deposition conditions, the organic aprotic solvent medium contributes to the formation of spherical AuNPs with 2D substrate filling. It is established that the AuNPs deposited on the silicon surface catalyze the process of metal-assisted chemical etching (MacEtch), which makes it possible to obtain Si nanostructures in the form of nanowire arrays.

1. Introduction

MacEtch is one of the anisotropic methods for obtaining Si nanostructures of different morphologies, in particular porous Si [1–4], nanowires, and complex nanostructures [5–10]. They are the basis for modern devices used in nanoelectronics [11], optoelectronics [12–15], and devices for energy conversion and storage [16–19]. This method involves the deposition of the discrete metal nanoparticles as well as the porous metal nanofilms on the Si surface. These metals serve as the catalysts of local etching of the substrate in solutions based on oxidant and acid [1]. MacEtch occurs through the electrochemical mechanism, when metal nanoparticles (MNPs) are the cathode regions and the silicon surface in direct contact with MNPs is the anode. Thus, electrochemical reduction of hydrogen in the cathode region and local dissolution of Si with the formation of pores in the anode region occur. The higher potential difference ($\Delta E = E^0_{M^{n+}/M} - E^0_{Si^{4+}/Si}$) between cathode and anode sections leads to the greater rate of these processes. This is primarily due to the value of the standard electrode potential for the metal ($E^0_{M^{n+}/M}$). Therefore, metals which are characterized by high values of this parameter, such as noble metals (Au, Pt, Ag, and Pd), are used for MacEtch [8, 14, 19–21]. Noble metals are also characterized by high chemical and electrochemical resistance at the nanoscale level. The predominant use of AuNPs as the catalysts in the MacEtch method is due to the highest value of its standard electrode potential ($E^0_{Au^{3+}/Au} = 1.49$ V) and, consequently, to its high catalytic activity. This contributes to directional local vertical etching of the Si surface and allows the Si nanowires to be extracted with a high aspect ratio [1, 5, 10].

The most common methods of metal nanoparticle (MNP) deposition on a Si surface are the physical ones [22, 23]. They require the use of expensive equipment and are energy consuming. Therefore, in the last decade, there is

a tendency to find alternative methods, among which is GR [24–26]. Mostly, GR is carried out in an aqueous solution, where the hydrogen release on cathode regions and the etching of a substrate occur besides the main process of metal recovery as byprocesses [25, 27–30]. This complicates the controlled formation of MNPs, as a necessary condition for the surface modification. As it was shown in our previous works [31–34], GR in the organic solvent medium overcomes these disadvantages of aqueous solutions. In addition, organic solvents often play a role of a surfactant due to their electron-donor properties, affecting the geometry of nanoparticles and their size distribution.

This study aims to establish the optimal conditions for the control over the deposition process of catalytically active AuNPs with good density and geometry on the Si substrate surface by GR method thanks to the use of DMSO solvent. These synthesized AuNPs are predicted to be used for fabrication of Si nanostructures of given morphology via the MacEtch method.

2. Experimental

For our studies, n-Si(100) substrates with resistivity of 4 Ω·cm were used. The substrate was cut into equal pieces of $1 \times 1\ \text{cm}^2$. The samples were preliminary washed in acetone and ethanol in ultrasonic bath and then etched in a solution containing 5% HF and DMSO solvent for 10 min. The deposition of gold on a Si surface was carried out by the GR method from solutions of 2–8 mM $HAuCl_4$ ($HAuCl_4 \cdot 3H_2O$, 99.99%, Alfa Aesar) in the presence of HF (1% mass) in DMSO solvent (99%, Alfa Aesar). Afterwards, the samples were immersed in a solution of metal salt and kept in a hydrostatic mode at the temperatures of 40–60°C for 0.5–4 min. After AuNPs were deposited onto Si surface, the samples were washed sequentially with ethanol and acetone and dried at the temperature of 60°C.

The etching of the modified Si surface was carried out in a solution based on HF (40%), H_2O_2 (35%), and deionized water H_2O. The volumetric ratio of the components used in etching solution was 4 : 1 : 4. The etching was performed for a duration of 15 min at room temperature, after which the samples were washed in deionized water and dried in a heat chamber (80°C).

The morphology of the Si surface after the AuNP deposition and MacEtch was studied using scanning electron microscopes ZEISS EVO 40XVP and SELMI REM-106I, respectively. The images of the modified surface were obtained by recording secondary electrons by scanning an electron beam of 20 kV energy. The chemical composition of the resulting precipitates was characterized using the energy-dispersive X-ray spectroscopy (EDX).

AuNP size and density were determined by using the public domain Java image processing program ImageJ2 [35]. The ImageJ2 package is a free cross-platform software with an open architecture that allows calculating areas and statistical indicators of pixel values of different areas on images, extracted manually or using threshold functions. The statistical histograms were obtained using ORIGIN software pack with its standard deviation values of nanoparticle size.

3. Results and Discussion

Galvanic replacement of gold by silicon in DMSO-based H$[AuCl_4]$ solutions containing HF occurs by reaction (1). The process is carried out according to the electrochemical mechanism, which includes the presence of anode and cathode regions on the substrate surface where the electrically generating half-reaction (2) and the half-reaction of the $[AuCl_4]^-$ ion reduction (3) are localized. The high value of the electromotive force of the process $\Delta E^0 (E^0_{Au^{3+}/Au} - E^0_{[SiF_6]^{2-}/Si} = 2.62\ \text{V})$ provides high cathode current densities and, accordingly, high rates of total reaction (1).

$$4\left[AuCl_4\right]^- + 3Si + 18F^- = 4Au + 16Cl^- + 3\left[SiF_6\right]^{2-} \quad (1)$$

$$\text{Anode region: } Si + 6F^- \longrightarrow \left[SiF_6\right]^{2-} + 4e, \quad E_0 = -1.20\ \text{V} \quad (2)$$

$$\text{Cathode region: } \left[AuCl_4\right]^- + 3e \longrightarrow Au + 4Cl^-, \quad E_0 = 1.42\ \text{V} \quad (3)$$

The high stability of complex ions $[AuCl_4]^-$ ($K_{\text{instab.}} = 1 \cdot 10^{-19}$) causes a significant cathode polarization of gold reduction. Cathodic polarization also intensifies the formation of surface complexes on nanoclusters and metal nanoparticles due to donor-acceptor coupling of adsorbed donor-based solvent molecules [31]. This contributes to the formation of small-sized spherical particles, as well as their uniform distribution over the whole substrate surface (Figures (1)–(3)). As it follows from EDX analysis, GR in DMSO solvent results in the formation of Au deposits on the surface of Si (Figure 1(d)).

The concentration of precipitating metal ions and the temperature significantly affect the cathodic polarization. Thus, with an increase in the concentration of H$[AuCl_4]$ from 2 to 8 mM, the particles' size and their density on the Si surface increase (Figure 1). A tendency of the agglomerates formation is also observed (Figure 1(c)). However, there is a 2D substrate filling with particles up to 100 nm in size (Figures 1(a) and 1(b)). Consequently, the concentration of ions $[AuCl_4]^-$ is an effective factor of influence on the morphology of AuNPs deposited by GR onto the Si surface.

The temperature in the electrochemical processes is a depolarizing factor. When it increases, the rate of the electrically generating reaction of the anode dissolution of Si rises (2) and, consequently, the current density at the cathode regions (i_{cathode}) increases, thus leading to an intensification of the cathode metal reduction (3). Therefore, an increase in the temperature from 40 to 60°C tends to cover the substrate surface by the increasing amount of deposited AuNPs (Figures 1(b), 2(a), and 2(b)). An increase in the temperature also causes desorption of DMSO molecules from nanoclusters and AuNPs. Consequently, the inhibitory effect of the surface complexes on the nanoparticle growth decreases, and the "smoothing" effect is neglected. Therefore, the size of AuNPs increases from 40 to 80 nm at 40°C to 80–120 nm and 120–160 nm at 50 and 60°C, respectively (Figures 2(c)and 2(d)).

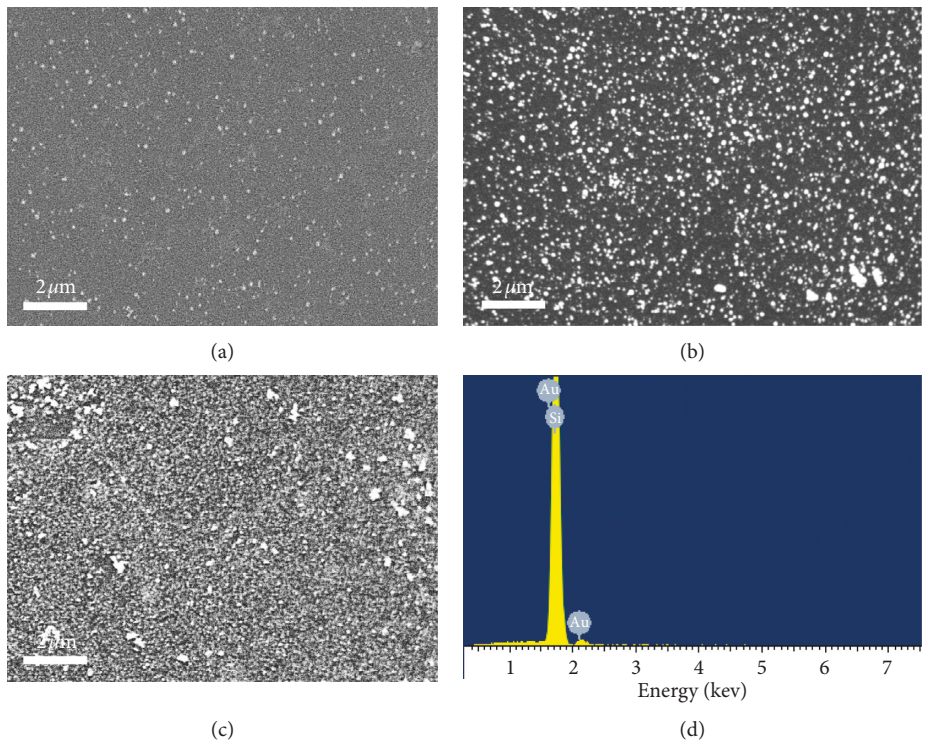

Figure 1: SEM image of the Si surface covered with gold deposited from a solution containing 2 mM (a), 4 mM (b), and 8 mM (c) $H[AuCl_4]$ by the GR method in the DMSO solvent for 1 min at 50°C and EDX spectrum (d).

During GR of gold on the Si surface by reaction (1), the size of AuNPs grows in time without an increase in their amount (Figure 3(d)). This indicates that the process of nucleation occurs in the initial period of GR, and in the future, the predominant growth of the formed particles takes place (Figures 3(a)–3(c)). It is known [36] that the activation energy of the nucleation process is much greater than that of the nanocluster and nanoparticle growth. Therefore, the last process has a priority. Thus, the duration of GR process is one of the factors influencing the sizes of AuNPs on the Si surface.

One of the main applications of galvanic replacement of AuNPs on the surface of Si is the creation of Si nanowires. At the same time, it is important to obtain an array of discrete Au nanoparticles. Wu et al. [2] synthesized dendritic Au layers on the Si wafer surface by the GR method. Furthermore, they have shown that the MacEtch of such samples produces a porous structure but not an array of nanowires. In contrast to the authors of the paper [2], we synthesized discrete AuNPs by the GR method, the compactness and density of which on the Si wafer surface being controlled by selecting a proper temperature and deposition time. No dendritic structures were found, however.

Next, we used these synthesized AuNPs for fabrication of Si nanowires of given morphology by means of the MacEtch method. As a result of etching of the Si wafer samples covered with AuNPs deposited from a solution of 4 mM $H[AuCl_4]$ at 50°C in the HF-H_2O_2-H_2O etchant for 15 min, the arrays of Si nanowires on a Si wafer surface were formed (Figure 4). The morphology of Si nanowires is similar to those obtained by other scientists [37]. Such a rough surface morphology is promising from the point of view of ultrahigh light absorption, where the nanoforest acts as an antireflective surface.

In Figure 4(a) we see that the nanowires are quite densely spaced, forming a thick nanoforest. So, in this case, it makes sense to conclude a high surface coverage of Si wafer with nanowires.

The cross section SEM image (Figure 4(b)) allows to estimate the main nanorod parameters and average size. The nanowires' diameter ranges from 100 to 300 nm, and the height is about 2.5 μm (estimated from inset in Figure 4(b)). The vertical etching rate was 167 nm/min, so the height is a function of etching time. We can predict that with longer etching times the height of the nanoforest will increase. As the nanowires' height was the same order, we can assume that the AuNPs synthesized in the DMSO solvent show a good adhesion to the surface of Si wafer. Further studies are needed however.

All technological conditions for the AuNP formation on the surface of silicon wafers are suitable for the nanowire fabrication, since, as it was shown in [9, 37], Si nanostructures are formed using the metal catalysts both, in the form of discrete close-packed particles, and porous films as well. On the other hand, AuNPs in the form of a porous film are not suitable for plasmonics as the plasmon effects depend on the size and distance between the metal nanoparticles. In our case, the technological conditions for the deposition of AuNPs allow to obtain discrete particles in which plasmon effects can be manifested. These issues require further studies.

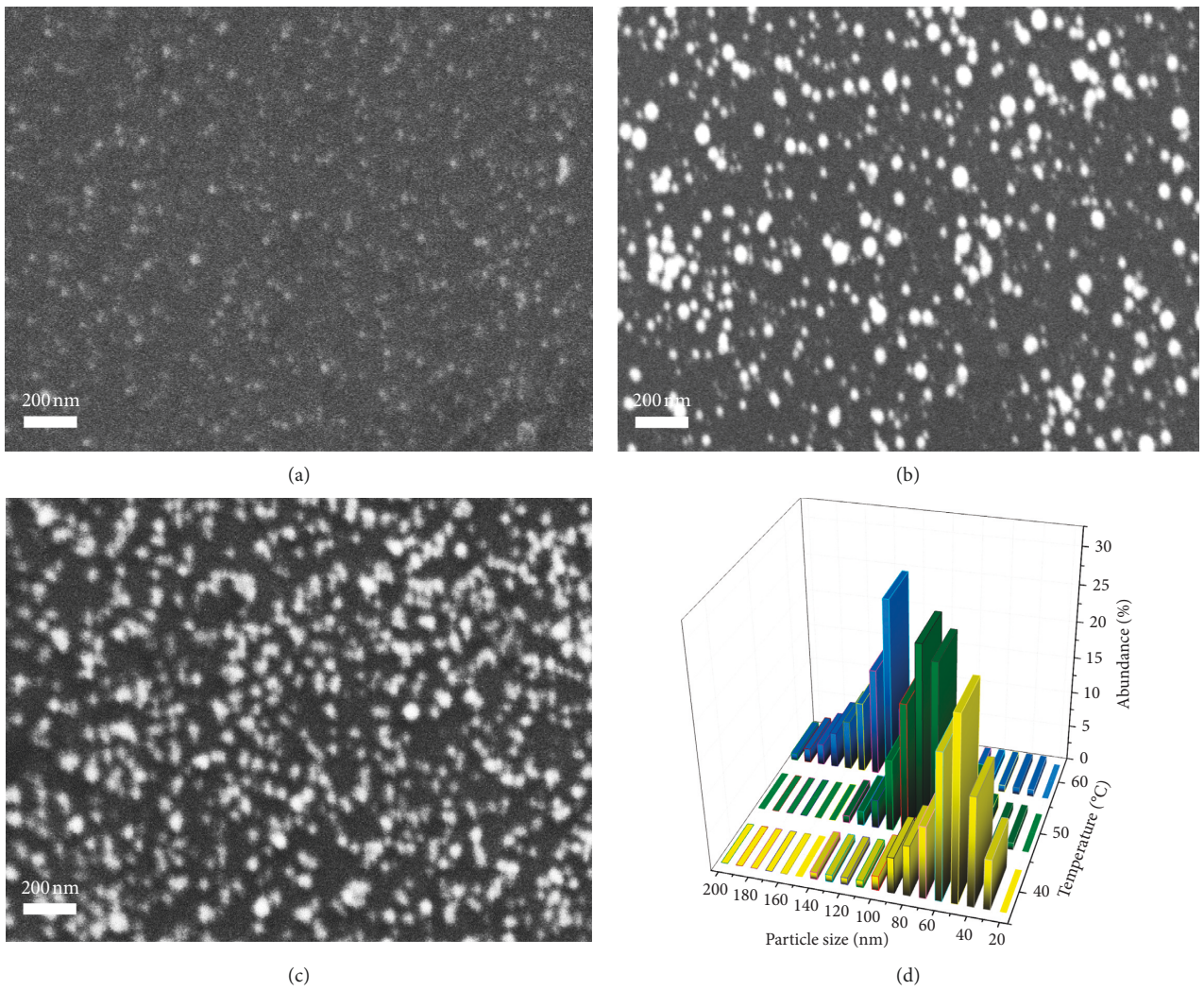

Figure 2: SEM image of the Si surface covered with gold deposited from a solution of 4 mM $H[AuCl_4]$ by the GR method in DMSO for 1 min at 40°C (a), 50°C (b), and 60°C (c), and the size distribution histograms of AuNPs (d).

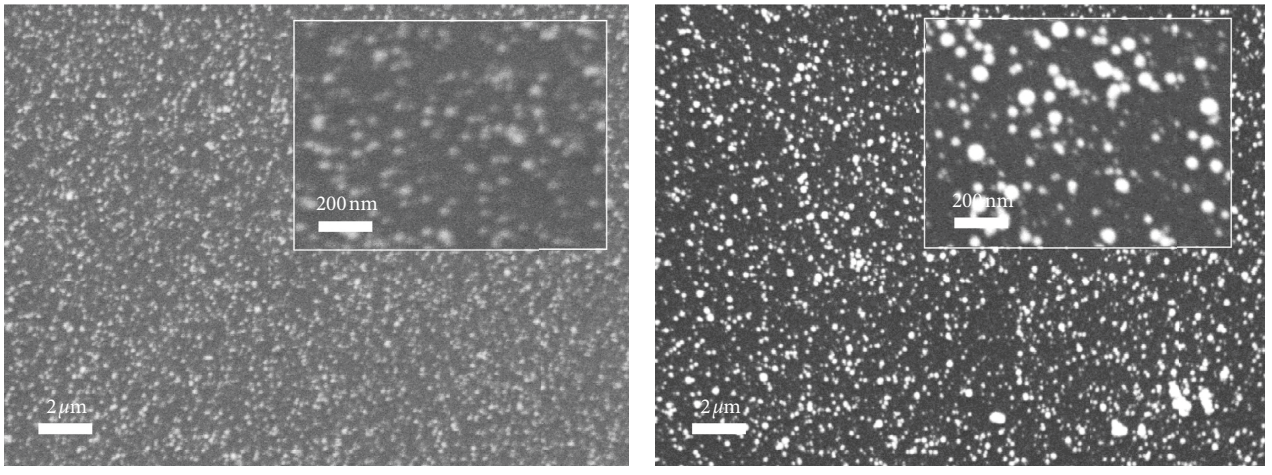

Figure 3: Continued.

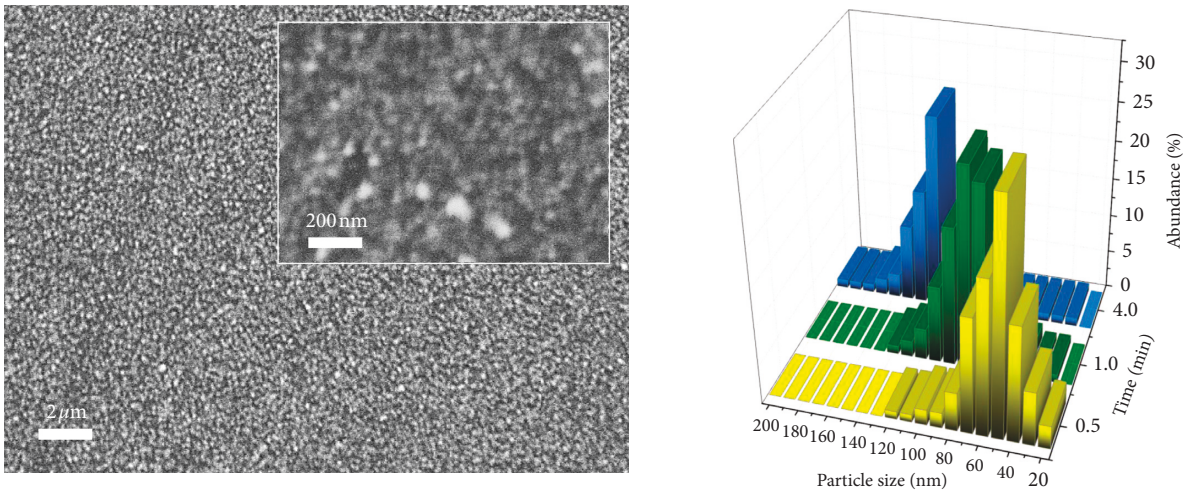

(c) (d)

Figure 3: SEM image of the Si surface covered with gold deposited from a solution of 4 mM $H[AuCl_4]$ by the GR method in DMSO at 50°C for 0.5 min (a), 1 min (b), and 4 min (c), and the size distribution histograms of AuNPs (d).

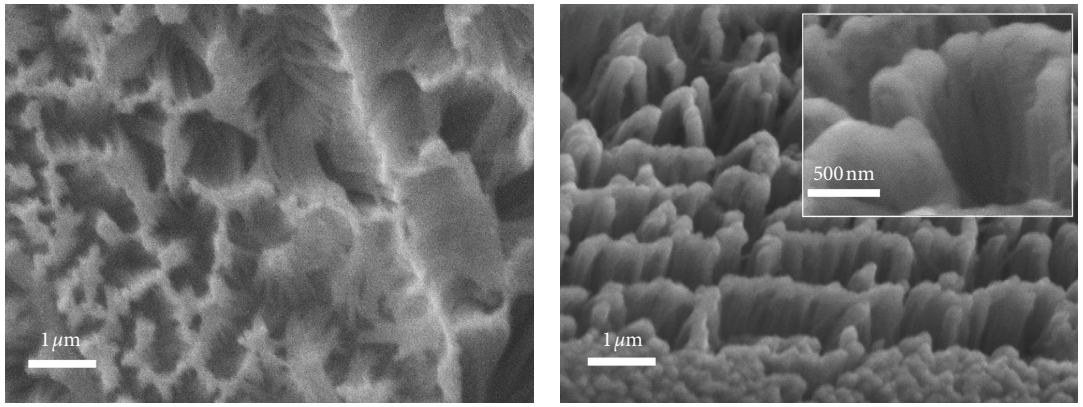

(a) (b)

Figure 4: Top-view (a) and cross section (b) SEM images of Si nanowires arrays formed after the 15 min HF-H_2O_2-H_2O etching of Si substrate covered with AuNPs deposited from a solution of 4 mM $H[AuCl_4]$ at 50°C.

4. Conclusions

Gold nanoparticles up to 100 nm are deposited on the Si surface at 2–8 mM $H[AuCl_4]$ in the DMSO solvent in the presence of fluoride ions by the GR method at 40–60°C. The organic aprotic solvent medium contributes to the formation of spherical metal particles and the 2D surface filling of the Si surface and also prevents the side processes to occur during GR. The main factors influencing the size of AuNPs are the concentration of $H[AuCl_4]$, temperature, and the process duration. As their values increase, the size of the nanoparticles increases as well. Gold nanoparticles synthesized by the GR method in the mixture of $H[AuCl_4]$ and organic DMSO solvent on the Si wafer surface gave the possibility to produce more complex structures by means of the MacEtch technique in the form of Si nanowire arrays, which are one of the most promising materials for modern nanoelectronic devices. Thus, the control over the process of GR of AuNPs of given morphology, shape, size, and distribution on the Si surface opens up the opportunity to create more complex device structures.

Data Availability

The data used to support the findings of this study are included within the article.

Conflicts of Interest

The authors declare that there are no conflicts of interest regarding the publication of this paper.

Acknowledgments

This work was financially supported by the Ministry of Education and Science of Ukraine under the project

"Controlled electrochemical synthesis of metal nanoparticles and nanostructured materials" (State Registration no. 0118U000268).

References

[1] Z. Huang, N. Geyer, P. Werner, J. de Boor, and U. Gösele, "Metal-assisted chemical etching of silicon: a review," *Advanced Materials*, vol. 23, no. 2, pp. 285–308, 2011.

[2] H.-L. Wu, C.-H. Chen, and M. H. Huang, "Seed-mediated synthesis of branched gold nanocrystals derived from the side growth of pentagonal bipyramids and the formation of gold nanostars," *Chemistry of Materials*, vol. 21, no. 1, pp. 110–114, 2009.

[3] A. Druzhinin, V. Yerokhov, S. Nichkalo, and Y. Berezhanskyi, "Micro- and nanotextured silicon for antireflective coatings of solar cells," *Journal of Nano Research*, vol. 39, pp. 89–95, 2016.

[4] R. F. Balderas-Valadez, V. Agarwal, and C. Pacholski, "Fabrication of porous silicon-based optical sensors using metal-assisted chemical etching," *RSC Advances*, vol. 6, no. 26, pp. 21430–21434, 2016.

[5] J. M. Duran and A. Sarangan, "Fabrication of ultrahigh aspect ratio silicon nanostructures using selfassembled gold metal-assisted chemical etching," *Journal of Micro/Nanolithography, MEMS, and MOEMS*, vol. 16, no. 1, article 014502, 2017.

[6] A. Stafiniak, J. Prażmowska, W. Macherzyński, and R. Paszkiewicz, "Nanostructuring of Si substrates by a metal-assisted chemical etching and dewetting process," *RSC Advances*, vol. 8, no. 54, pp. 31224–31230, 2018.

[7] S. Ashrafabadi and H. Eshghi, "Single-crystalline Si nanowires fabrication by one-step metal assisted chemical etching: the effect of etching time and resistivity of Si wafer," *Superlattices and Microstructures*, vol. 120, pp. 517–524, 2018.

[8] P. V. Trinh, P. N. Hong, B. H. Thang et al., "Effect of surface morphology and dispersion media on the properties of PEDOT:PSS/n-Si hybrid solar cell containing functionalized graphene," *Advances in Materials Science and Engineering*, vol. 2017, Article ID 2362056, 9 pages, 2017.

[9] S. Nichkalo, A. Druzhinin, A. Evtukh, O. Bratus', and O. Steblova, "Silicon nanostructures produced by modified MacEtch method for antireflective Si surface," *Nanoscale Research Letters*, vol. 12, no. 1, p. 106, 2017.

[10] B. Miao, J. Zhang, X. Ding et al., "Improved metal assisted chemical etching method for uniform, vertical and deep silicon structure," *Journal of Micromechanics and Microengineering*, vol. 27, no. 5, article 055019, 2017.

[11] H. Han, Z. Huang, and W. Lee, "Metal-assisted chemical etching of silicon and nanotechnology applications," *Nano Today*, vol. 9, no. 3, pp. 271–304, 2014.

[12] R. F. Balderas-Valadez, J. O. Estévez-Espinoza, U. Salazar-Kuri, C. Pacholski, W. L. Mochan, and V. Agarwal, "Fabrication of ordered tubular porous silicon structures by colloidal lithography and metal assisted chemical etching: SERS performance of 2D porous silicon structures," *Applied Surface Science*, vol. 462, pp. 783–790, 2018.

[13] A. A. Druzhinin, Lviv Polytechnic National University, S. I. Nichkalo, and O. Y. Ostapiv, "Development of anti-reflecting surfaces based on Si micropyramids and wet-chemically etched Si nanowire arrays," *Functional Materials*, vol. 25, no. 4, pp. 675–680, 2018.

[14] M. Lajvardi, H. Eshghi, M. Izadifard, M. E. Ghazi, and A. Goodarzi, "Effects of silver and gold catalytic activities on the structural and optical properties of silicon nanowires," *Physica E: Low-Dimensional Systems and Nanostructures*, vol. 75, pp. 136–143, 2016.

[15] M. Pavlenko, E. L. Coy, M. Jancelewicz et al., "Enhancement of optical and mechanical properties of Si nanopillars by ALD TiO2 coating," *RSC Advances*, vol. 6, no. 99, pp. 97070–97076, 2016.

[16] S. Nichkalo, A. Druzhinin, V. Yerokhov, and O. Ostapiv, "Fabrication and characterization of high-performance anti-reflecting nanotextured Si surfaces for solar cells," *Nanooptics, Nanophotonics, Nanostructures, and Their Applications*, vol. 210, pp. 275–283, 2018.

[17] W. McSweeney, H. Geaney, and C. O'Dwyer, "Metal-assisted chemical etching of silicon and the behavior of nanoscale silicon materials as Li-ion battery anodes," *Nano Research*, vol. 8, no. 5, pp. 1395–1442, 2015.

[18] K.-Q. Peng and S.-T. Lee, "Silicon nanowires for photovoltaic solar energy conversion," *Advanced Materials*, vol. 23, no. 2, pp. 198–215, 2011.

[19] M.-H. Shiao, C.-P. Lai, B.-H. Liao, and Y.-S. Lin, "Effect of photoillumination on gold-nanoparticle-assisted chemical etching of silicon," *Journal of Nanomaterials*, vol. 2018, Article ID 5479605, 5 pages, 2018.

[20] N. Geyer, B. Fuhrmann, Z. Huang, J. de Boor, H. S. Leipner, and P. Werner, "Model for the mass transport during metal-assisted chemical etching with contiguous metal films as catalysts," *The Journal of Physical Chemistry C*, vol. 116, no. 24, pp. 13446–13451, 2012.

[21] J.-M. Chen, C.-Y. Chen, C. P. Wong, and C.-Y. Chen, "Inherent formation of porous p-type Si nanowires using palladium-assisted chemical etching," *Applied Surface Science*, vol. 392, pp. 498–502, 2017.

[22] C. Zhang, K. Lin, Y. Huang, and J. Zhang, "Graphene-Ag hybrids on laser-textured Si surface for SERS detection," *Sensors*, vol. 17, no. 7, pp. 1462–1470, 2017.

[23] Z. Huang, X. Zhang, M. Reiche et al., "Extended arrays of vertically aligned sub-10 nm diameter [100] Si nanowires by metal-assisted chemical etching," *Nano Letters*, vol. 8, no. 9, pp. 3046–3051, 2008.

[24] Q. Wei, Y.-S. Shi, K.-Q. Sun, and B.-Q. Xu, "Pd-on-Si catalysts prepared via galvanic displacement for the selective hydrogenation of para-chloronitrobenzene," *Chemical Communications*, vol. 52, no. 14, pp. 3026–3029, 2016.

[25] S. S. Djokić and K. Cadien, "Galvanic deposition of silver on silicon surfaces from fluoride free aqueous solutions," *ECS Electrochemistry Letters*, vol. 4, no. 6, pp. 11–13, 2015.

[26] A. Raygani and L. Magagnin, "Gold metallization of silicon by galvanic displacement," *Electrochemical Society (ECS) Transactions*, vol. 41, pp. 3–8, 2012.

[27] A. Gutes, I. Laboriante, C. Carraro, and R. Maboudian, "Palladium nanostructures from galvanic displacement as hydrogen peroxide sensor," *Sensors and Actuators B: Chemical*, vol. 147, no. 2, pp. 681–686, 2010.

[28] C. Carraro, R. Maboudian, and L. Magagnin, "Metallization and nanostructuring of semiconductor surfaces by galvanic displacement processes," *Surface Science Reports*, vol. 62, no. 12, pp. 499–525, 2007.

[29] A. Gutés, C. Carraro, and R. Maboudian, "Ultrasmooth gold thin films by self-limiting galvanic displacement on silicon," *ACS Applied Materials & Interfaces*, vol. 3, no. 5, pp. 1581–1584, 2011.

[30] S. Y. Sayed, F. Wang, M. Malac, A. Meldrum, R. F. Egerton, and J. M. Buriak, "Heteroepitaxial growth of gold nanostructures on silicon by galvanic displacement," *ACS Nano*, vol. 3, no. 9, pp. 2809–2817, 2009.

[31] O. Kuntyi, Lviv Polytechnic National University, M. Shepida et al., "Modification of silicon surface with silver, gold and palladium nanostructures via galvanic substitution in DMSO and DMF solutions," *Chemistry & Chemical Technology*, vol. 12, no. 3, pp. 305–309, 2018.

[32] H. Itasaka, M. Nishi, M. Shimizu, and K. Hirao, "Growth of nanogold at interfaces between locally induced naked silicon surfaces and pure $HAuCl_4$ solutions," *Journal of The Electrochemical Society*, vol. 163, no. 14, pp. D743–D746, 2016.

[33] O. Y. Dobrovets'ka, O. I. Kuntyi, G. I. Zozulya, I. V. Saldan, and O. V. Reshetnyak, "Galvanic deposition of gold and palladium on magnesium by the method of substitution," *Materials Science*, vol. 51, no. 3, pp. 418–423, 2015.

[34] Y.-C. Wang, J.-Y. Lin, C.-H. Wang, P.-L. Huang, S.-L. Lee, and J.-K. Chang, "Formation of metal coatings on magnesium using a galvanic replacement reaction in ionic liquid," *RSC Advances*, vol. 4, no. 67, p. 35298, 2014.

[35] C. T. Rueden, J. Schindelin, M. C. Hiner et al., "ImageJ2: imageJ for the next generation of scientific image data," *BMC Bioinformatics*, vol. 18, no. 1, p. 529, 2017.

[36] S. Simeonova, P. Georgiev, K. S. Exner et al., "Kinetic study of gold nanoparticles synthesized in the presence of chitosan and citric acid," *Colloids and Surfaces A: Physicochemical and Engineering Aspects*, vol. 557, pp. 106–115, 2018.

[37] M.-L. Seol, J.-H. Ahn, J.-M. Choi, S.-J. Choi, and Y.-K. Choi, "Self-aligned nanoforest in silicon nanowire for sensitive conductance modulation," *Nano Letters*, vol. 12, no. 11, pp. 5603–5608, 2012.